

SIMULATING REALISTIC LYMAN- α EMITTERS INCLUDING THE EFFECT OF RADIATIVE TRANSFER

HASTI KHORAMINEZHAD¹, SHUN SAITO^{1,2}, MAX GRONKE^{3,4}, CHRIS BYROHL^{2,5}

¹ Institute for Multi-messenger Astrophysics and Cosmology, Department of Physics, Missouri University of Science and Technology,
1315 N Pine Street, Rolla, MO 65409, USA

² Kavli Institute for the Physics and Mathematics of the Universe (Kavli IPMU, WPI), University of Tokyo, Chiba 277-8582, Japan

³ Astronomisches Rechen-Institut, Zentrum für Astronomie, Universität Heidelberg, Mönchhofstraße 12-14, 69120 Heidelberg, Germany

⁴ Max-Planck-Institut für Astrophysik, Karl-Schwarzschild-Str. 1, 85741 Garching, Germany

⁵ Institut für Theoretische Astrophysik, Universität Heidelberg, ZAH, Albert-Ueberle-Str. 2, 69120 Heidelberg, Germany

Version July 23, 2025

ABSTRACT

We present an empirical yet physically motivated simulation of realistic Lyman- α emitters (LAEs) at $z \sim 2-3$, crucial for ongoing and forthcoming cosmological LAE surveys. We combine an empirical UniverseMachine galaxy-halo model with a simple spherical expanding shell model for the Lyman- α radiative transfer, calibrating only three free parameters to simultaneously reproduce the observed Lyman- α luminosity function and the angular clustering. Our LAE model is further supported by its consistency with other observables such as the Lyman- α equivalent width distribution, the Lyman- α escape fraction as a function of stellar mass and dust reddening, and the systemic velocity offsets. Our LAE model provides predictions for the halo occupation distributions for LAEs and relationship between Ly α luminosity and halo mass, including the distribution of satellite LAEs. Our work provides a crucial first step towards creating a high-fidelity LAE synthetic catalog for the LAE cosmology surveys. We make our LAE catalog and spectra publicly available upon publication.

Subject headings: Large-scale structure — Lyman-Alpha Emitters — Lyman-Alpha Radiative Transfer

1. INTRODUCTION

Realistic high-fidelity mock galaxy catalogs play a crucial role in precision cosmology from large-scale structure surveys (e.g., Kitaura et al. 2016; Saito et al. 2016; Rossi et al. 2021; Prada et al. 2023; Euclid Collaboration et al. 2025). In particular, there is currently a strong demand for a high-fidelity catalog for Lyman- α (Ly α) emitting galaxies (LAEs). LAEs offer powerful probes of the high-redshift Universe (e.g., Partridge & Peebles 1967; Chiang et al. 2013; Ebina & White 2024) and thus LAEs at $z \sim 2-3$ are targeted by various optical and near-infrared galaxy surveys; ongoing ones such as the Hobby-Eberly Telescope Dark Energy Experiment (HETDEX, Gebhardt et al. 2021; Hill et al. 2021) and the Javalambre Physics of the Accelerating Universe Astrophysical Survey (J-PAS, Benitez et al. 2014) as well as forthcoming ones such as the second stage of the Dark Energy Spectroscopic Instrument (DESI-II, Schlegel et al. 2022), the Multiplexed Survey Telescope (MUST, Zhao et al. 2024), the Wide-field Spectroscopic Telescope (WST, Mainieri et al. 2024), and the proposed Spectroscopic Stage-5 experiment (Spec-S5, Besuner et al. 2025). A realistic LAE mock catalog is crucial to optimize their survey strategies, calibrate LAE selection functions, and to interpret cosmological analyses, since any systematic uncertainties could bias the inferred cosmological parameters.

A realistic mock LAE catalog shall reproduce two essential observables: (i) the observed LAE luminosity function and (ii) the LAE clustering on large scales. The clustering strength of galaxies on large scales, $\geq \mathcal{O}(10 \text{ Mpc})$, is the main target of the aforementioned surveys as a source of cosmological information such as the Baryon Acoustic Oscillations (BAO) and the Redshift Space Distortion (RSD). In addition, the clustering at intermediate scales, $\mathcal{O}(0.1-10 \text{ Mpc})$, carries the important information on how the galaxies are connected with underlying dark matter halos and thus how galaxies have evolved in the context of the large-scale structure (see e.g., Wechsler & Tinker 2018, for a review). The LAE luminosity function controls the Poisson shot noise of the clustering measurements at a given survey flux threshold. Beyond these two primary requirements, it is beneficial for the catalog to also reproduce additional observed properties such as the distribution of Ly α equivalent width (EW) that characterizes the strength of the Ly α emission line with respect to the continuum level. The EW distribution and additional observational constraints (see e.g., Ouchi et al. 2020, for a review) further improve the fidelity of the observed sample selection.

Cosmological galaxy formation simulations are an important tool in the creation of mock catalogs. Yet, their limited dynamical spatial range and modeling uncertainties down to individual HII regions, sourcing most of an LAEs' photons, impede a straightforward use to create LAE mocks. In addition, Ly α photons are resonantly scattered by neutral hydrogen atoms on any scale that spans the interstellar medium (ISM), the circumgalactic medium (CGM), and the intergalactic medium (IGM). In dense HI regions, each Ly α photon could undergo an extremely large number of scatterings, often up to millions, on the ISM and CGM scales (Laursen et al. 2009; Dijkstra 2017) and be absorbed by dust grains (Atek et al. 2008; Duval et al. 2014). Resonant

scattering also changes the spectral line profile of Ly α : photons diffusing in frequency to the line wings can escape more easily. The Ly α line is typically redshifted and broadened compared to the intrinsic emission (Verhamme, A. et al. 2006; Yang et al. 2016). Each scattering imparts a frequency shift, and photons that eventually escape have often shifted to the red side of the line or even emerged as double-peaked profiles bracketing the systemic wavelength (see e.g., Steidel et al. 2010; Leclercq et al. 2017; Runnholm et al. 2021). The impact on Ly α radiative transfer on the spectral profile was theoretically investigated by analytic methods (e.g., Harrington 1973; Neufeld 1990; Nebrin et al. 2025; Smith et al. 2025) and simulation methods (e.g., Zheng & Miralda-Escudé 2002; Dijkstra et al. 2006; Tasitsiomi 2006; Verhamme, A. et al. 2006; Semelin et al. 2007; Zheng et al. 2010; Yajima et al. 2012; Gronke et al. 2015; Gronke & Dijkstra 2016; Song et al. 2020; Smith et al. 2022; Xu et al. 2023; Almada Monter & Gronke 2024; Chang & Gronke 2024). In addition, even in an optically thin regime on IGM scales, the redshifted Ly α photon on the blue side of the spectrum could be attenuated by HI in the IGM (e.g., Laursen et al. 2011; Byrohl & Gronke 2020). All of these processes complicate the interpretation of LAE observations. This means that the presence or absence of Ly α emission is not a simple indicator of the intrinsic properties of the galaxy but rather a convoluted result of Ly α radiative transfer (RT) through density and kinematics of HI gas and dust at a wide range of scales, $O(10\text{ pc}-10\text{ Mpc})$ (see Dijkstra (2017) for a comprehensive review of Ly α RT). Despite extensive surveys and large samples, connecting the observed Ly α luminosities and spectra to the underlying star formation activity and dark-matter halos remains non-trivial. For example, it is unclear whether the LAE-halo connection can be modeled by a simple framework that works for a mass-selected galaxy sample such as the Halo Occupation Distribution (HOD) approach (e.g., Hamana et al. 2004; Ouchi et al. 2018; Hong et al. 2019; Herrero Alonso et al. 2021).

One may wonder if these complications are relevant only for small-scale galaxy formation physics. However, some previous work pointed out that complications in Ly α RT could have an impact on the cosmological interpretation of large-scale LAE clustering. The IGM attenuation on the blue side of the Ly α spectrum could potentially correlate with the large-scale density field and introduces the anisotropic selection effect, leading to suppression of clustering along the line of sight (Zheng et al. 2011; Behrens et al. 2018; Gurung-López et al. 2019b). Furthermore, the peak shift and smearing of the Ly α emission could be regarded as a velocity offset that leads to an effect similar to the Finger-of-God suppression (Byrohl et al. 2019; Gurung-López et al. 2021; Lujan Niemeyer 2025). Thus, we argue that *one needs to model the Ly α spectra* for a realistic LAE mock catalog, since Ly α RT shapes the Ly α line profile and the escape fraction of photons, which ultimately impact the selection of LAEs and their inferred large-scale distribution (see e.g., Landriau et al. 2025, for a recent comparison of LAE spectra between HETDEX and DESI).

It is not computationally feasible to fully solve the physics of Ly α RT in a hydrodynamical simulation at all relevant scales in a self-consistent manner and to scale it up to the cosmological volume required for the LAE surveys. There are recent promising progress along this line, but they still require calibration of their subgrid physics such as dust attenuation, and it is unclear how well they can reproduce the radiative transfer processes on the sub-parsec scale (Smith et al. 2022; Xu et al. 2023; Byrohl & Nelson 2023). Alternatively, one could empirically model the Ly α escape fraction for LAEs without incorporating Ly α RT physics, but adopt a physical model for all galaxy populations from a hydrodynamical simulation (Nagamine et al. 2010; Shimizu & Umemura 2010; Shimizu et al. 2011; Im et al. 2024; Ravi et al. 2024; Sullivan et al. 2025) or from a semi-analytical model (Le Delliou et al. 2006; Kobayashi & Totani 2008). Notably, there are only a few exceptions in the literature that model LAEs at $z = 2-3$ by incorporating Ly α RT (Garel et al. 2015; Gurung-López et al. 2019a,b; Byrohl & Nelson 2023) (see also e.g., Hutter et al. 2015; Inoue et al. 2018; Gronke et al. 2021, for reionization studies at higher redshifts). We will discuss the differences in these previous works in more detail in Sec. 5.1.

In this work, we advance the modeling of LAEs by developing a framework to construct a high-fidelity mock LAE catalog that satisfies the following conditions:

1. it is applicable to a dark-matter only N -body simulation so that it can be readily scaled to a Gpc-scale simulation in the future,
2. it includes a model for global galaxy properties such as the stellar mass and star formation rate (SFR), which allows us to model the intrinsic Ly α luminosity and predict the relation between LAEs and other population of galaxies,
3. it incorporates a Ly α RT model that allows us to predict the Ly α spectra, and
4. the model is calibrated such that it simultaneously reproduces the observed luminosity function and clustering of LAEs as well as other LAE diagnostics, when possible, such as the EW distribution, systemic velocity offset, and the dust reddening strength.

Our approach is built on an empirical galaxy formation model, UniverseMachine (Behroozi et al. 2019), which is calibrated to a broad range of galaxy observables and thus provides a realistic (albeit imperfect) population of galaxies, satisfying conditions 1) and 2). To meet condition 3), we then link Ly α emission to these galaxies via the direct results of the Monte Carlo Ly α RT code with a spherical expanding shell model on the ISM/CGM scales (Gurung-López et al. 2021) and the mean IGM transmission modified from Laursen et al. (2011). As we shall show, our calibrated model successfully reproduces various LAE observables (condition 4)).

This paper is organized as follows. In Sec. 2 we describe N -body simulation data and observational data. Sec. 3 details our approach to modeling LAEs. In Sec. 4, we present our main fitting results as well as implications of our simulated LAE mock

catalogs. We clarify the difference between our work and others and the limitations of our approach in Sec. 5 before we conclude this work in Sec. 6. Supplementary information on model validation and further technical considerations is provided in the appendices. Throughout this paper, we denote the comoving and physical distance units as cMpc/h and pMpc/h etc., respectively. The rest frame wavelength is denoted without any superscripts, while the observed one is clarified as λ^{obs} . For example, the rest frame Ly α wavelength is denoted by $\lambda_{\text{Ly}\alpha} = 1215.67 \text{ \AA}$. We define galaxies with Ly α luminosity of $\log_{10}(L_{\text{Ly}\alpha}/\text{erg s}^{-1}) \geq 41.7$ and equivalent width of $\text{EW}_0 > 40 \text{ \AA}$ as our fiducial “LAEs” when we compare our model with observational data unless it has different specific criteria, and call galaxies that do not satisfy the criteria as “others”.

2. SIMULATION AND OBSERVATIONAL DATASET

In this section, we describe the external datasets including both cosmological simulations and observations. Note that we only include the observational measurements adopted in our fitting procedure here, while we will compare predictions from our LAE mock with other measurements in the literature in later sections.

2.1. *N*-body simulation

The goal of this work is to model LAEs on top of a dark-matter only *N*-body simulation such that it simultaneously reproduces both the LAE luminosity function and the spatial clustering at $\mathcal{O}(0.1\text{--}10 \text{ cMpc}/h)$. This requires a simulation with as large a box size and as high a mass resolution as possible. Taking into account that LAEs are typically hosted by dark-matter halos with a mass of $\geq 10^{11} M_{\odot}$ at $2 \lesssim z \lesssim 3$ (see e.g., Ouchi et al. 2020), we adopt the Small MultiDark Planck (SMDPL) simulation (Klypin et al. 2016) in this work. We justify our choice by comparing the mass resolution in Appendix A.1. SMDPL has 3840^3 dark matter particles with particle mass of $m_p = 9.63 \times 10^7 M_{\odot}/h$ in a periodic box with a comoving length of $400 \text{ cMpc}/h$. The simulation is run using the L-Gadget-2 code, a performance-optimized version of the publicly available cosmological code Gadget-2 (Springel 2005) with a force resolution of $1.5 \text{ ckpc}/h$. The cosmological parameters for these simulations are $h = 0.6777$, $\Omega_{\Lambda} = 0.692885$, $\Omega_m = 0.307115$, $\Omega_b = 0.048206$, $n = 0.96$ and $\sigma_8 = 0.8228$, closely aligned with Planck Collaboration et al. (2014). Dark matter halos and subhalos are identified using the Rockstar halo finder (Behroozi et al. 2012a) and halo merger trees are constructed using the Consistent Trees algorithm (Behroozi et al. 2012b).

2.2. The UniverseMachine galaxy-halo model

Since LAEs are observationally thought to be young star-forming galaxies (Dijkstra 2017; Kusakabe et al. 2018; Ouchi et al. 2020; McCarron et al. 2022; Firestone et al. 2025) and intrinsic Lyman- α luminosity is primarily correlated with the star formation rate (SFR) (Kennicutt 1998; Tilvi et al. 2009; Dijkstra & Westra 2010; Sobral & Matthee 2019; Runnholm et al. 2020), we need a prescription to predict a SFR for each individual galaxy or dark matter halo in the simulation. To this end, we adopt an empirical framework UniverseMachine (Behroozi et al. 2019) to connect the properties of galaxies and dark matter halos. In this framework, the assembly history of the stellar mass is parameterized as a function of the assembly history of the halo mass on a given dark-matter-only *N*-body simulation. Then, the free parameters are determined so that they reproduce observational data across $0 < z < 10$ including stellar mass functions, cosmic and specific SFRs, Ultraviolet (UV) luminosity functions, quenched fractions, correlation functions for all, quenched, and star-forming galaxies, measurements of the environmental dependence of central galaxy quenching, and UV-stellar mass relations.

In this work, we adopt a publicly available UniverseMachine model run on the SMDPL simulation (SMDPL-UM hereafter) and use two snapshots at $z = 2.42$ and 3.03 which hereafter we will denote $z \sim 2$ and $z \sim 3$, respectively. We do not use a light-cone realization of SMDPL-UM, which is left for future work. We use (sub)halo properties of the three-dimensional position, peculiar velocity, the maximum circular velocity of a halo, $V_{\text{max}} \equiv \max(\sqrt{GM_{\text{halo}}(< R)}/R)$, the virial mass M_{vir} , and the virial radius R_{vir} as well as galaxy properties of stellar mass M_* , and the SFR_{int} in this work. We do not adopt the observed SFR_{obs} and $M_{\text{UV,obs}}$ available in the SMDPL-UM catalog and instead recalibrate these quantities in order to ensure consistency with the observed UV luminosity function at $z \sim 2$ and 3 , incorporating an empirical dust model. This allows us to obtain a more realistic prediction for the observed equivalent width and the observed escape fraction (see Sec 4.3 for a comparison of our model with observations). Following Behroozi et al. (2019), the observed SFR_{obs} is modeled by

$$\log_{10} \left(\frac{\text{SFR}_{\text{obs}}}{M_{\odot} \text{ yr}^{-1}} \right) = \mu \log_{10} \left(\frac{\text{SFR}_{\text{int}}}{M_{\odot} \text{ yr}^{-1}} \right) + \kappa \exp \left\{ -\frac{(z-2)^2}{2} \right\}, \quad (1)$$

where the mean shift μ and the scatter κ are added to the UM-intrinsic SFR_{int} mainly to take into account the uncertainties in inferring SFR from observations. Note that our SFR_{obs} is not exactly equivalent to the one in Behroozi et al. (2019), since we do not use SFR derived from a spectral fitting. Rather, we account for the amount of ionized photon budget by SFR_{obs} to explain the UV luminosity function. We assume the Kennicutt relation that relates SFR_{obs} to the UV luminosity density at $\lambda = 1500 \text{ \AA}$, $L_{\lambda, \text{UV}}^{\text{int}} = 1.4 \times 10^{40} \text{ erg s}^{-1} \text{ \AA}^{-1} \times (\text{SFR}/M_{\odot} \text{ yr}^{-1})$ (Kennicutt 1998). Fig. 1 shows that SFR_{int} is not sufficient to explain the faint-end UV luminosity function in $M_{\text{UV}} \gtrsim -20 \text{ mag}$. We then recalibrate the mean shift value μ such that it reproduces the faint end of the UV luminosity function, producing $\mu = 0.5$, i.e., 0.5 dex higher SFR.

The 0.5 dex addition is still consistent with the observed SFR data points within 2σ errors at $z \sim 2$ and 3 (see Fig. 3 in Behroozi et al. (2019)). We do not recalibrate the scatter κ , since the shift at faint end appears constant. This SFR addition is not fully convincing and satisfying but is necessary to account for the insufficient amount of UV photons. This discrepancy may

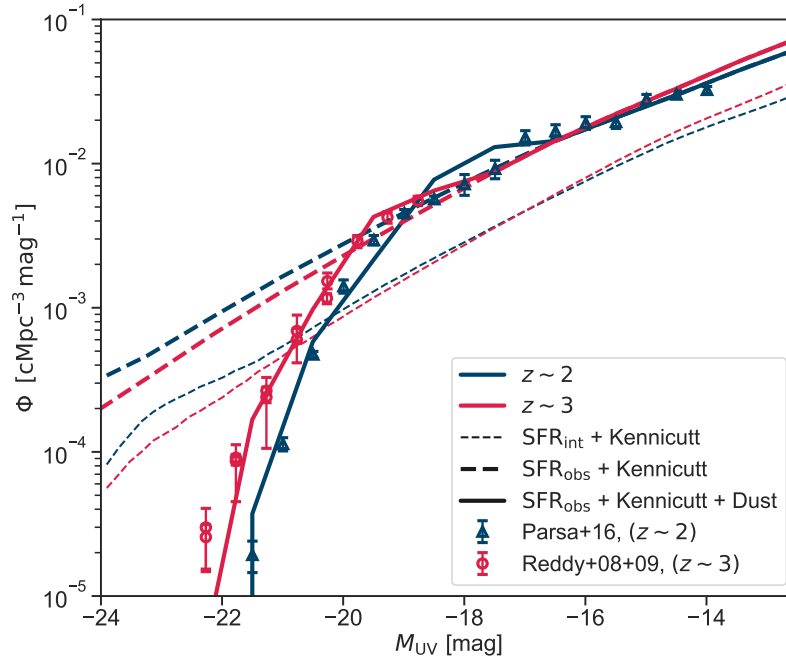


FIG. 1.— UV luminosity function at $z \sim 2$ (blue) and $z \sim 3$ (red) compared to observational data from Parsa et al. (2016) at $z \sim 2$ and Reddy et al. (2008); Reddy & Steidel (2009) at $z \sim 3$. The model (thick solid curves) calibrates the SFR to reproduce the UV luminosity function incorporating the empirical dust model from Vogelsberger et al. (2020). The dust model is not included in dashed lines. The thin dashed lines assume the SFR_{int} from the UniverseMachine model assuming Kennicutt relation, $L_{\text{cont},\lambda} = 1.4 \times 10^{40} \text{ erg s}^{-1} \text{ \AA}^{-1} \times (\text{SFR}/\text{M}_{\odot} \text{yr}^{-1})$ (Kennicutt 1998).

be attributed to starburst activities (e.g., Sun et al. 2023, 2024; Haskell et al. 2024) or tensions between infrared and UV SFR indicators (e.g., Fang et al. 2018). Note that the original $M_{\text{UV,obs}}$ available in the SMDPL-UM catalog is not reliable, as they are calibrated with UV luminosity functions only at $z > 4$ (Behroozi et al. 2019). We also checked the redshift evolution of UV luminosity function at $z = 2-3$. In Appendix A.2, we demonstrate that, once Eq. (1) is applied, the predicted rest-frame UV luminosity function of the SMDPL-UM catalog exhibits negligible evolution over $1.9 \leq z \leq 3.2$.

The mismatch at the bright end can be attributed to dust attenuation for UV photons. To model the dust attenuation, we adopt the ‘model A’ in Vogelsberger et al. (2020) which empirically calibrates the UV dust optical depth as a function of $M_{\text{UV,int}}$ and redshift (see Eq. (7) in Vogelsberger et al. 2020 but with different parameters; $C_0 = 4.43$, $C_1 = 1.99$, $M_0 = -19.5$, $\sigma_{\beta} = 0.34$ for constant values, for the redshift dependent part, we used $\beta_{M_0} = -0.97$ and $d\beta/dM_{\text{UV}}^{\text{obs}} = -0.71$ at $z = 2.42$ and $\beta_{M_0} = -1.78$ and $d\beta/dM_{\text{UV}}^{\text{obs}} = -0.73$ at $z = 3.03$). This operation gives us the dust optical depth for UV photons, $e^{-\tau_{\text{UV}}} = L_{\lambda,\text{UV}}^{\text{obs}}/L_{\lambda,\text{UV}}^{\text{int}}$. This simple approach to recovering a realistic UV luminosity function is sufficient for our purpose to model the equivalent width of LAEs.

A potential caveat in the UM framework could be “orphan” subhalos/galaxies which are no longer associated with any subhalo or halo in the halo catalog but originate from subhalos in earlier snapshots. We refer the reader to Jiang & van den Bosch (2016) and Behroozi et al. (2019) for a specific implementation of the orphans. In Appendix A.3, we quantify the impact of the orphans on our results. We also note that the measurement of the stellar mass function relevant to our LAE sample is not available particularly at $\log_{10}(M_{*}/M_{\odot}) < 11$ at $z \sim 3$, and thus it does not contribute to constraining the SMDPL-UM model.

2.3. Observational measurements of the LAE summary statistics

We use recent measurements of the luminosity function and the angular correlation function to calibrate our LAE model at both $z \sim 2$ and $z \sim 3$. In summary, we use the $z \sim 2.2$ luminosity function from Konno et al. (2016), the $z \sim 3.1$ luminosity function from Ouchi et al. (2008), and the angular correlation function from White et al. (2024) as our fiducial choice. In Appendices C.1 and C.2, we show our results with different measurements from Umeda et al. (2025) and Khostovan et al. (2019). All of these measurements are based on LAEs detected with narrow-band surveys. We will briefly describe these default datasets below.

The $z \sim 3.1$ luminosity function from Ouchi et al. (2008) is derived from a 1 deg^2 sky of the Subaru/XMM-Newton Deep Survey field. Their $z \sim 3.1$ sample consists of 356 LAEs detected through a narrow-band filter, NB503, with a central wavelength of $\lambda_c^{\text{obs}} = 5029 \text{ \AA}$ and a full width at half maximum (FWHM) of $\Delta\lambda^{\text{obs}} = 74 \text{ \AA}$. Their limiting magnitude roughly corresponds to

$\log_{10}(L_{\text{Ly}\alpha} [\text{erg s}^{-1}]) \simeq 42$. A spectroscopic follow-up campaign shows that the contamination fraction of the photometric LAE sample at $z = 3.1$ is estimated to be $< 13\%$. The $z \sim 2.2$ luminosity function from [Konno et al. \(2016\)](#) is measured in the luminosity range of $\log_{10}(L_{\text{Ly}\alpha} / \text{erg s}^{-1}) = 41.7 - 44.4$ with a total of 3137 LAEs detected by a narrow-band filter, NB387, with a central wavelength of $\lambda_c^{\text{obs}} = 3870\text{\AA}$ and a FWHM of $\Delta\lambda^{\text{obs}} = 94\text{\AA}$ in five independent fields that span a total of 1.43 deg^2 . They estimated that the contamination fraction from, e.g., low-redshift [OII] emitters is less than a few percent. This is in part because they applied an EW cut of $\geq 70 \text{\AA}$ to mitigate contamination from low- z [OII] emitters. In [Konno et al. \(2016\)](#), they also reported that the bright-end LAE luminosity function is dominated by active galactic nuclei (AGNs) (see also e.g., [Zheng et al. 2016](#); [Spinoso et al. 2020](#); [Zhang et al. 2021](#); [Liu et al. 2022a,b](#); [Torralba-Torregrosa et al. 2023a](#)). Therefore, we limit ourselves to the maximum luminosity of $\log_{10}(L_{\text{Ly}\alpha} / \text{erg s}^{-1}) = 43.0$ in this work, since we do not include AGNs in our model. In addition, we ignore interloper contamination and the impact of an incomplete sample selection (an EW cut, for instance) in these luminosity function measurements ([Konno et al. 2016](#)). A comparison of various LAE luminosity function measurements at $z = 2-3$ in the literature is presented in [Blanc et al. \(2011\)](#); [Konno et al. \(2016\)](#); [Herenz et al. \(2019\)](#); [Torralba-Torregrosa et al. \(2023b\)](#); [Umeda et al. \(2025\)](#).

We also use both $z \sim 2.4$ and $z \sim 3.1$ angular correlation functions in [White et al. \(2024\)](#), based on LAEs selected from the One-hundred-deg² DECam Imaging in Narrowbands (ODIN; [Ramakrishnan et al. \(2023\)](#); [Firestone et al. \(2023\)](#); [Lee et al. \(2024\)](#)). The ODIN survey is a wide-field, deep imaging survey targeting seven fields with three narrow-band filters, designed to select LAEs at redshifts $z \sim 2.4, 3.1$, and 4.5 . The 822 (1099) LAEs at $z \sim 2.4$ (3.1) are detected with N419 and N501 filters over the COSMOS field with limiting magnitude of 25.5 and 25.7, corresponding to Ly α line flux limits of 1.547×10^{42} and $1.584 \times 10^{42} \text{ erg s}^{-1}$. A subset of these objects was subjected to spectroscopic follow-up with the Dark Energy Spectroscopic Instrument (DESI; [Levi et al. \(2013\)](#); [DESI Collaboration et al. \(2016\)](#)), and these data were used to refine the narrow-band selection criteria, as well as to constrain the interloper fraction and the redshift distribution. With these follow-up observations, the contamination fractions are estimated between 0.02 and 0.08 at $z \sim 2.4$ and between 0.04 and 0.11 at $z \sim 3.1$, respectively. The clustering amplitude is directly affected by the contamination fraction f_{cont} by a factor of $(1 - f_{\text{cont}})^2$ (assuming that the contaminating objects do not cluster). We will adopt the most conservative values, i.e., $f_{\text{cont}} = 0.08$ at $z \sim 2.4$ and $f_{\text{cont}} = 0.11$ at $z \sim 3.1$ in our fitting processes.

3. MODELING THE LYMAN- α EMITTERS

3.1. Overview

We model the Ly α spectrum for each individual galaxy in the SMDPL-UM model, which can affect the LAE observability due to RT effects. We incorporate the Ly α RT effect on the Ly α spectrum across the ISM/CGM and IGM scales rather than assuming a simple scaling relation between the observed Ly α luminosity and other galaxy properties. We give an overview of our model here and then will discuss each ingredient in more detail in the subsequent subsections.

The starting point of our model is the linear relation between the intrinsic Ly α luminosity and SFR, given by (see e.g., [Dijkstra 2017](#))

$$L_{\text{Ly}\alpha}^{\text{int}} = 1.0 \times 10^{42} \text{ erg s}^{-1} \times \left(\frac{\text{SFR}_{\text{obs}}}{M_{\odot} \text{ yr}^{-1}} \right), \quad (2)$$

where the case-B recombination at the ISM gas temperature of 10^4 K is assumed, and the relation between SFR and the ionizing photon emission rate is calibrated assuming the Salpeter Initial Mass Function (IMF) ([Kennicutt 1998](#)). Although it is well known that different assumptions on the IMF shape and metallicity can lead to different normalizations of the relationship between the SFR_{obs} and $L_{\text{Ly}\alpha}^{\text{int}}$ ([Schaerer 2003](#)), this normalization still represents a conservative Ly α luminosity when compared to other literature values ([Kennicutt 1998](#); [Kroupa 2001](#); [Chabrier 2003](#); [Finkelstein et al. 2011a](#); [Dijkstra 2017](#); [Sobral & Matthee 2019](#)). We assume a Gaussian line profile with intrinsic line width W_{in} and a flat continuum with intrinsic equivalent width (in rest frame) EW_{in} , both of which will be specified in Sec. 3.2.

We model the rest-frame spectrum $\phi(\lambda) = \phi_{\text{Ly}\alpha}(\lambda) + \phi_{\text{cont}}(\lambda)$ that consists of the Ly α emission, $\phi_{\text{Ly}\alpha}(\lambda)$, and the continuum $\phi_{\text{cont}}(\lambda)$, as follows. The Ly α RT on the ISM and CGM scales is effectively modeled by the expanding gas shell model, closely following [Gurung-López et al. \(2019a\)](#) as we discuss in Sec. 3.2 in detail. This provides the line profile $\phi_{\text{Ly}\alpha}^{\text{ISM}}(\lambda; \vec{\theta}_g(\alpha, \beta, \gamma))$ for each individual galaxy. $\vec{\theta}_g(\alpha, \beta, \gamma)$ denotes a set of galaxy parameters necessary for the shell model with three dimensionless free parameters (α, β, γ) , and will be specified in Sec. 3.2. Then, the Ly α luminosity $L_{\text{Ly}\alpha}^{\text{ISM}}$ after escaping from the ISM/CGM scales is given by

$$L_{\text{Ly}\alpha}^{\text{ISM}} = \int \phi_{\text{Ly}\alpha}^{\text{ISM}}(\lambda; \vec{\theta}_g(\alpha, \beta, \gamma)) d\lambda = f_{\text{esc}}^{\text{ISM}} L_{\text{Ly}\alpha}^{\text{int}}, \quad (3)$$

where $f_{\text{esc}}^{\text{ISM}}$ is the ISM escape fraction of Ly α photons, and the integration is evaluated within $\pm 10 \text{\AA}$ from the Ly α line center. We also account for the impact of IGM transmission $T_{\text{IGM}}(\lambda)$. As we discuss in Sec. 3.4, we will simply assume that the IGM transmission $T_{\text{IGM}}(\lambda; z)$ depends only on redshift, neglecting line-of-sight variations. Thus, we model the observed Ly α

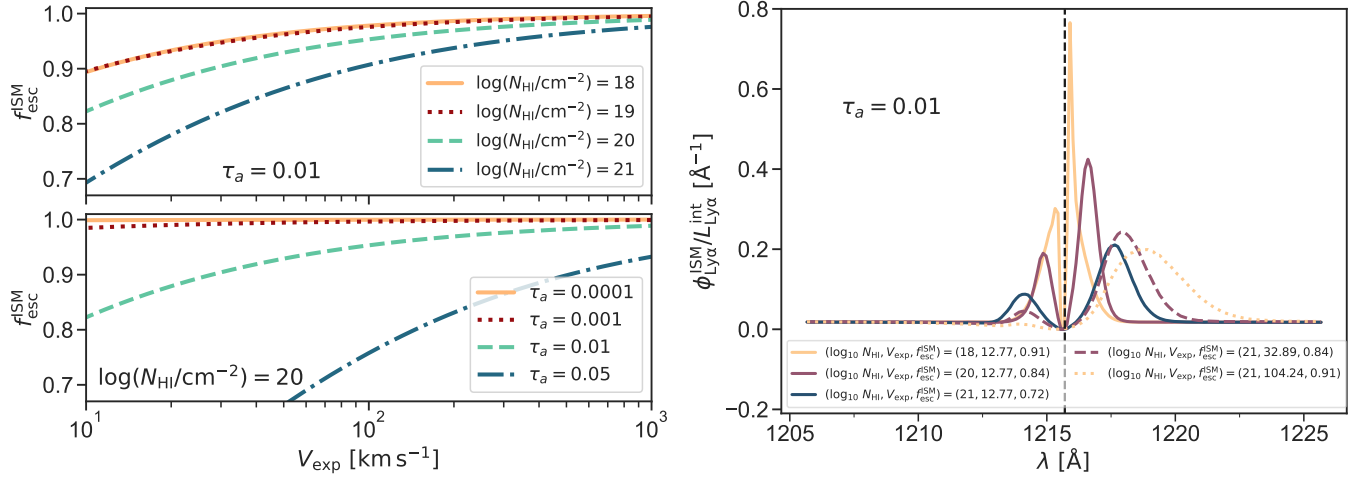


FIG. 2.— *Left*: ISM escape fraction, $f_{\text{esc}}^{\text{ISM}}$, as a function of expansion velocity, V_{exp} , neutral hydrogen column density, N_{HI} , and dust absorption optical depth, τ_a . Top panel shows how $f_{\text{esc}}^{\text{ISM}}$ changes for various N_{HI} values at a fixed $\tau_a = 0.01$. The bottom panel presents the dependence on τ_a for a fixed $\log_{10}(N_{\text{HI}}/\text{cm}^{-2}) = 20$. *Right*: Example line profile of the galaxies with various shell model parameters. The three parameters in each legend corresponds to $\log_{10}(N_{\text{HI}}/\text{cm}^{-2})$, $V_{\text{exp}}/(\text{km s}^{-1})$, and $f_{\text{esc}}^{\text{ISM}}$. The vertical dashed line shows the rest frame Ly α wavelength, $\lambda_{\text{Ly}\alpha} = 1215.67 \text{ \AA}$.

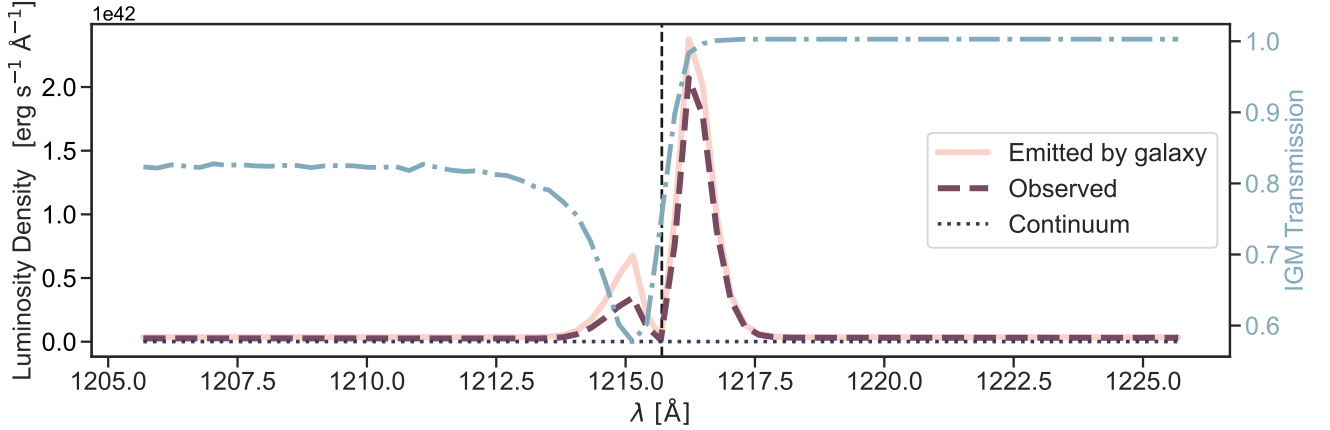


FIG. 3.— The impact of Ly α RT on an example Ly α profile. This galaxy resides at $z = 2.42$, with $M^* = 4.59 \times 10^8 M_{\odot}$, $\text{SFR} = 1.01 M_{\odot} \text{ yr}^{-1}$ and the shell model's key parameters of $V_{\text{exp}} = 21.41 \text{ km/s}$, $\log_{10} N_{\text{HI}} = 19.48 \text{ cm}^{-2}$ and $\tau_a = 0.03$. The light red solid curve represents the emitted Ly α luminosity density from the ISM/CGM. The dark dashed curve corresponds to the observed Ly α spectrum after incorporating both ISM/CGM and IGM effects. The blue dot-dashed curve (right y-axis) represents the IGM transmission. The vertical black dashed line marks the rest-frame Ly α line center wavelength, ($\lambda = 1215.67 \text{ \AA}$).

luminosity by

$$L_{\text{Ly}\alpha}^{\text{obs}} = \int \phi_{\text{Ly}\alpha}^{\text{ISM}}(\lambda; \vec{\theta}_g(\alpha, \beta, \gamma)) T^{\text{IGM}}(\lambda; z) d\lambda = f_{\text{esc}}^{\text{IGM}} L_{\text{Ly}\alpha}^{\text{ISM}} = f_{\text{esc}}^{\text{IGM}} f_{\text{esc}}^{\text{ISM}} L_{\text{Ly}\alpha}^{\text{int}}, \quad (4)$$

where the fraction of Ly α luminosity, $f_{\text{esc}}^{\text{IGM}} \equiv L_{\text{Ly}\alpha}^{\text{obs}}/L_{\text{Ly}\alpha}^{\text{ISM}}$, depends on each galaxy property through the observed line profile $\phi^{\text{obs}}(\lambda) = \phi^{\text{ISM}}(\lambda; \vec{\theta}_g) \times T^{\text{IGM}}(\lambda; z)$, and the observed Ly α escape fraction corresponds to $f_{\text{esc}, \text{Ly}\alpha}^{\text{obs}} = f_{\text{esc}}^{\text{ISM}} f_{\text{esc}}^{\text{IGM}}$ in this notation. We will discuss later in more detail how to estimate the rest-frame equivalent width of each LAE. In summary, we attempt to model the LAEs with the three dimensionless free parameters (α, β, γ) so that they reproduce both the Ly α luminosity function and the angular correlation function at the same time. The advantage of our work is that it predicts the observed Ly α luminosity and line profile for each individual galaxy, which allows us to study statistical correlation between Ly α emission diagnostics and other galaxy properties.

3.2. Modeling the Ly α Radiative Transfer on ISM/CGM scales

To effectively capture the impact of Ly α RT on ISM/CGM scales, we adopt the model with an expanding spherical gas shell, following Gurung-López et al. (2019a). The expanding spherical shell model has been widely used in the literature to study Ly α RT and understand how key parameters, such as outflow velocity and gas column density, shape the observed line profiles (e.g., Zheng & Miralda-Escudé (2002); Dijkstra et al. (2006); Verhamme, A. et al. (2006); Tasitsiomi (2006); Semelin et al. (2007); Laursen et al. (2009); Yajima et al. (2012); Gronke et al. (2015); Smith et al. (2015)). In this model, an LAE galaxy is surrounded

by an expanding homogeneous isothermal spherical shell of neutral hydrogen gas with a fixed temperature of ($T = 10^4$ K) and the inner-to-outer radius fraction of 0.9. Even in this simplified geometry, it is computationally infeasible to perform a full Monte Carlo RT simulation for millions of individual simulated galaxies. For this reason, we adopt the publicly available Python package zELDA (Gurung-López et al. 2019; Gurung-López et al. 2021) that provides a fast prediction of the Ly α line profile trained by precomputed grids of full Monte Carlo simulations with a simple neural network¹. In zELDA, the Ly α line profile including both emission and continuum is calculated using five input parameters; expansion velocity V_{exp} , neutral hydrogen column density N_{HI} , optical depth of dust attenuation τ_a , intrinsic line width W_{in} , and intrinsic equivalent width EW_{in} .

$$\vec{\theta}_g = (V_{\text{exp}}, N_{\text{HI}}, \tau_a, W_{\text{in}}, EW_{\text{in}}). \quad (5)$$

In the left panel of Fig. 2, we show the ISM escape fraction $f_{\text{esc}}^{\text{ISM}}$ as a function of three key parameters, V_{exp} , N_{HI} , and τ_a . A technical note is that zELDA is trained only in a limited range of parameters ($V_{\text{exp}} \text{ km s}^{-1} \in (0, 1000)$, $\log_{10}(N_{\text{HI}}/\text{cm}^{-2}) \in (17, 21.5)$, $\log_{10}(\tau_a) \in (-4, 0)$) and, in principle, there could be some galaxies that have values for these parameters outside of the trained range. In this case, we simply adopt the ISM escape fraction and the spectral profile from the closest boundary, as it physically makes sense to expect $f_{\text{esc}}^{\text{ISM}} = 1$ for sufficiently large V_{exp} , for example. In the right panel of Fig. 2, we further illustrate the impact of these parameters on the emergent Ly α line profiles by showing the corresponding spectra for galaxies with different N_{HI} and V_{exp} values. Three solid lines ($\log_{10}(N_{\text{HI}}/\text{cm}^{-2}) = 18, 20, 21$ for orange, purple, and blue, respectively) have different N_{HI} at a fixed V_{exp} , showing that a larger neutral hydrogen density diffuses more Ly α photons and results in a smaller $f_{\text{esc}}^{\text{ISM}}$. As a consequence, the peak positions at both the red and blue sides of the spectra are more apart from the line center. In addition, the expansion velocity increases from the blue solid line ($V_{\text{exp}} = 12.77 \text{ km s}^{-1}$), the purple dashed line ($V_{\text{exp}} = 32.89 \text{ km s}^{-1}$), to the orange dotted line ($V_{\text{exp}} = 104.24 \text{ km s}^{-1}$), at fixed N_{HI} . This comparison shows that an outflow gas with higher velocity suppresses the blue side of photon's spectra more, while shifting the red peak position to a larger wavelength. Notice that the same values of $f_{\text{esc}}^{\text{ISM}}$ are shared by the orange solid and dotted lines, as well as the purple solid and dashed lines, highlighting that we cannot determine gas physics only from the escape fraction.

The next question is then how to assign $\vec{\theta}_g$ for each simulated galaxy. Motivated by Gurung-López et al. (2019a), we characterize them as follows:

$$V_{\text{exp}} = \alpha \text{ sSFR } r_{1/2} = 0.0978\alpha \left(\frac{\text{sSFR}}{10^{-10} \text{ yr}^{-1}} \right) \left(\frac{r_{1/2}}{\text{pkpc}} \right) \text{ km s}^{-1}, \quad (6)$$

$$N_{\text{HI}} = \beta \frac{M_{\text{HI}}}{(4\pi m_{\text{H}}) r_{1/2}^2} = 9.94 \times 10^{21} \beta \left(\frac{M_{\text{HI}}}{10^9 M_{\odot}} \right) \left(\frac{r_{1/2}}{\text{pkpc}} \right)^{-2} \text{ cm}^{-2}, \quad (7)$$

$$\tau_a = \left(\frac{\gamma}{\beta} \right) (1 - A_{\text{Ly}\alpha}) \frac{E_{\odot}}{Z_{\odot}} N_{\text{HI}} Z_{\text{cold}} = 0.11\gamma \left(\frac{M_{\text{HI}}}{10^9 M_{\odot}} \right) \left(\frac{r_{1/2}}{\text{pkpc}} \right)^{-2} \left(\frac{Z_{\text{cold}}}{0.0002} \right). \quad (8)$$

Here, the expansion velocity V_{exp} is scaled by the specific SFR ($\text{sSFR} \equiv \text{SFR}/M_*$) and the stellar-half mass radius $r_{1/2}$ (Hopkins et al. 2012; Arribas et al. 2014), while the neutral hydrogen column density, N_{HI} , is scaled by the neutral hydrogen mass, M_{HI} , and $r_{1/2}$. The optical depth of the dust attenuation τ_a is assumed to be proportional to the amount of gas-phase metallicity $N_{\text{HI}} Z_{\text{cold}}$. We assume a Ly α dust albedo of $A_{\text{Ly}\alpha} = 0.39$ at solar metallicity, $Z_{\odot} = 0.02$ (see Seaton (1979); Granato et al. (2000); Calzetti et al. (2000); Verhamme, A. et al. (2006); Scarlata et al. (2009)), and $E_{\odot}/Z_{\odot} = 8.85 \times 10^{-20} \text{ cm}^2$ refers to a reference dust opacity of the gas for solar metallicity. We introduced three constant free parameters (α, β, γ) which could absorb the inaccuracy of simple physical relations we assumed. The intrinsic line width W_{in} is determined by

$$W_{\text{in}} = \frac{V_{\text{max}}}{c} \lambda_{\text{Ly}\alpha}, \quad (9)$$

since the maximum circular velocity of a halo (V_{max} , see sec. 2.2 for the definition), traces the depth of halo gravitational potential and thus the kinetic energy of the halo. We assign the intrinsic EW by the intrinsic continuum level as

$$EW_{\text{in}} = \frac{L_{\text{Ly}\alpha}^{\text{int}}}{L_{\lambda, \text{UV}}^{\text{int}}}, \quad (10)$$

where $L_{\lambda, \text{UV}}$ is the rest-frame luminosity density of the continuum at $\lambda = 1500 \text{ \AA}$, extrapolated from the intrinsic UV magnitude $M_{\text{UV}}^{\text{int}}$ assuming the UV slope of -2 (Meurer et al. 1999; Bouwens et al. 2014).

In summary, for a given three dimensionless free parameter set of (α, β, γ), we need to specify θ_g in Eq. (5) which further depends on the parameters available in UniverseMachine, ($M_*, \text{sSFR}, V_{\text{max}}$) as well as the unavailable parameters, ($r_{1/2}, M_{\text{HI}}, Z_{\text{cold}}$).

¹ We do not implement the most updated version, zELDA II in Gurung-Lopez et al. (2025), since it relies on the specific IGM model in the IllustrisTNG simulation.

3.3. Scaling Relations

We outline below how we determine the parameters unavailable in `UniverseMachine`, $(r_{1/2}, M_{\text{HI}}, Z_{\text{cold}})$, for each galaxy. For simplicity, we rely on empirical relations motivated by previous observational results. This is distinct from [Gurung-López et al. \(2019a\)](#) who determined $r_{1/2}$, M_{HI} , and Z_{cold} within their semi-analytic model.

To model the galaxy size, we adopt the stellar half-mass radius, $r_{1/2}$, scaled with the halo virial radius, R_{vir} , with an associated scatter of 0.12 dex at fixed virial radius. [Kravtsov \(2013\)](#) found that $r_{1/2} \approx 0.015 R_{\text{vir}}$ at $z \sim 0$, a relation widely adopted in theoretical and observational studies (see, e.g., [Huang et al. 2017](#); [Somerville et al. 2018](#); [Hearin et al. 2019](#); [Zanisi et al. 2020](#)). Observations particularly on high redshifts show that LAEs are systematically more compact than other star-forming galaxies and that low-mass galaxies have an approximately constant half-mass radius ([Shibuya et al. 2015](#)), suggesting a mass-dependent size relation (see also [Ravindranath et al. 2004](#); [Ferguson et al. 2004](#); [van der Wel et al. 2014](#); [Shibuya et al. 2019](#), for other high-redshift studies.). Recent simulations also confirm this trend ([Pillepich et al. 2018](#); [Genel et al. 2014](#); [Vogelsberger et al. 2014a,b](#); [Somerville et al. 2025](#)). To incorporate this effect, we adopt a modified relation from [Kravtsov \(2013\)](#) that flattens the galaxy size-halo relation for smaller halos to account for the deviations seen in both simulations and observations. In practice, our prescription for $r_{1/2}$ is given by

$$\log_{10}(r_{1/2}/\text{pkpc}) = \begin{cases} \log_{10}(0.015 R_{\text{piv}}/\text{pkpc}) + \epsilon, & \text{if } R_{\text{vir}} \leq R_{\text{piv}} \\ \log_{10}(0.015 R_{\text{vir}}/\text{pkpc}) + \epsilon, & \text{if } R_{\text{vir}} > R_{\text{piv}} \end{cases} \quad (11)$$

where $R_{\text{piv}} = 113 \text{ pkpc}$ is the pivot radius, and the scatter term, ϵ , is drawn from a normal (Gaussian) distribution with mean zero and standard deviation $\sigma = 0.12$, corresponding to a 0.12 dex scatter in $\log_{10}(r_{1/2}/\text{pkpc})$. [Kravtsov \(2013\)](#) reported a scatter from 0.1 to 0.2 dex, while [Rohr et al. \(2022\)](#), using the FIRE simulations, reported a slightly smaller scatter of 0.084 dex. [Rohr et al. \(2022\)](#) further demonstrated that the galaxy-halo size relation exhibits very weak evolution from $z = 0$ to $z = 5$, with a scatter remaining nearly constant throughout this redshift range. This justifies our choice not to incorporate explicit redshift evolution in our size relation. Another technical reason to flatten the relation at a small radius is that N_{HI} would become unphysically larger as $r_{1/2}$ decreases (see Eq. (7)). In the top left panel of Fig. 4, we show the assumed size relation of all galaxies (colored scatter) compared to the empirical relation from [Kravtsov \(2013\)](#) (solid gray line). The shaded region around Kravtsov’s relation illustrates a broader scatter corresponding to the 2σ scatter expected from variations in dark matter halo spin. We also discuss the comparison with simulations in Appendix B.

To model the HI mass, M_{HI} , we adopt the scaling relation in terms of the stellar mass, M_* , motivated by results from the XGASS survey ([Catinella et al. 2018](#)). Specifically, we parametrize the cold gas mass as

$$\log_{10}\left(\frac{M_{\text{HI}}}{M_*}\right) = -0.5 \log_{10}(M_*/M_{\odot}) + 4 + \epsilon, \quad (12)$$

where the scatter term, ϵ , is drawn from a Gaussian distribution with mean zero and standard deviation $\sigma = 0.1$, corresponding to a 0.1 dex scatter in $\log_{10}(M_{\text{HI}}/M_*)$. This choice of scatter is taken from observational results, where a typical scatter in the gas fraction is around 0.1 dex ([Brown et al. 2015](#); [Saintonge et al. 2017](#); [Catinella et al. 2018](#)). In addition, recent hydrodynamic simulations, such as *IllustrisTNG* ([Marinacci et al. 2018](#); [Naiman et al. 2018](#); [Nelson et al. 2017](#); [Pillepich et al. 2017](#); [Springel et al. 2017](#)), *SIMBA* ([Davé et al. 2019](#)) and *EAGLE* ([Schaye et al. 2014](#); [Crain et al. 2015](#)) also show a comparable scatter of around 0.1 dex ([Davé et al. 2020](#)). Although observational data at relevant high redshifts is not available, several hydrodynamical simulations (*EAGLE*, *IllustrisTNG*, *SIMBA*, *FIRE*) consistently suggest only mild evolution in the $M_{\text{HI}}-M_*$ relation out to $z \sim 2-3$ ([Crain et al. 2017](#); [Davé et al. 2019](#)). This minimal evolution arises because galaxy gas reservoirs at different epochs self-regulate, with increased gas inflows at higher redshift balanced by enhanced star formation rates and stronger feedback-driven outflows. Thus, the atomic hydrogen content of galaxies at fixed stellar mass remains relatively stable across cosmic time, justifying our approach. This relation extends previous studies on gas fraction trends, derived from a robust sample to $M_* \sim 10^9 M_{\odot}$. Other observations consistently show that the fraction of atomic gases increases with decreasing stellar mass ([Huang et al. 2012](#); [Brown et al. 2015](#); [Saintonge et al. 2017](#); [Catinella et al. 2018](#)). The top right panel of Fig. 4 shows the assumed relation together with the XGASS results (gray points with errorbars).

The cold gas metallicity, Z_{cold} , refers to the abundance of elements heavier than helium in a galaxy’s cold gas phase, conventionally expressed as the ratio of the gas phase oxygen abundance to hydrogen. We adopt an empirical relation linking stellar mass, M_* , and cold gas metallicity, Z_{cold} , modified from the local observations by [Tremonti et al. \(2004\)](#):

$$12 + \log_{10}(Z_{\text{cold}}) = 0.38 \log_{10}(M_*/M_{\odot}) + 7.81 + \epsilon, \quad (13)$$

where we retain the slope of the [Tremonti et al. \(2004\)](#) relation but lower its normalization to achieve better consistency with observational measurement at $z = 2-3$ ([Erb et al. 2006](#); [Mannucci et al. 2009](#); [Finkelstein et al. 2011b](#); [Steidel et al. 2014](#); [Sanders et al. 2015](#)). The stochastic term, ϵ , is drawn from a Gaussian distribution with mean zero and standard deviation $\sigma = 0.05$, corresponding to 0.05 dex scatter in Z_{cold} . In the bottom panel of Fig. 4, we present our adapted scaling relation alongside observational measurements at various redshifts. Our choice of scatter (0.05 dex) is conservative and consistent with observational uncertainties. A comparison of our adopted relation with results from hydrodynamical simulations is presented in Appendix B, further validating our approach.

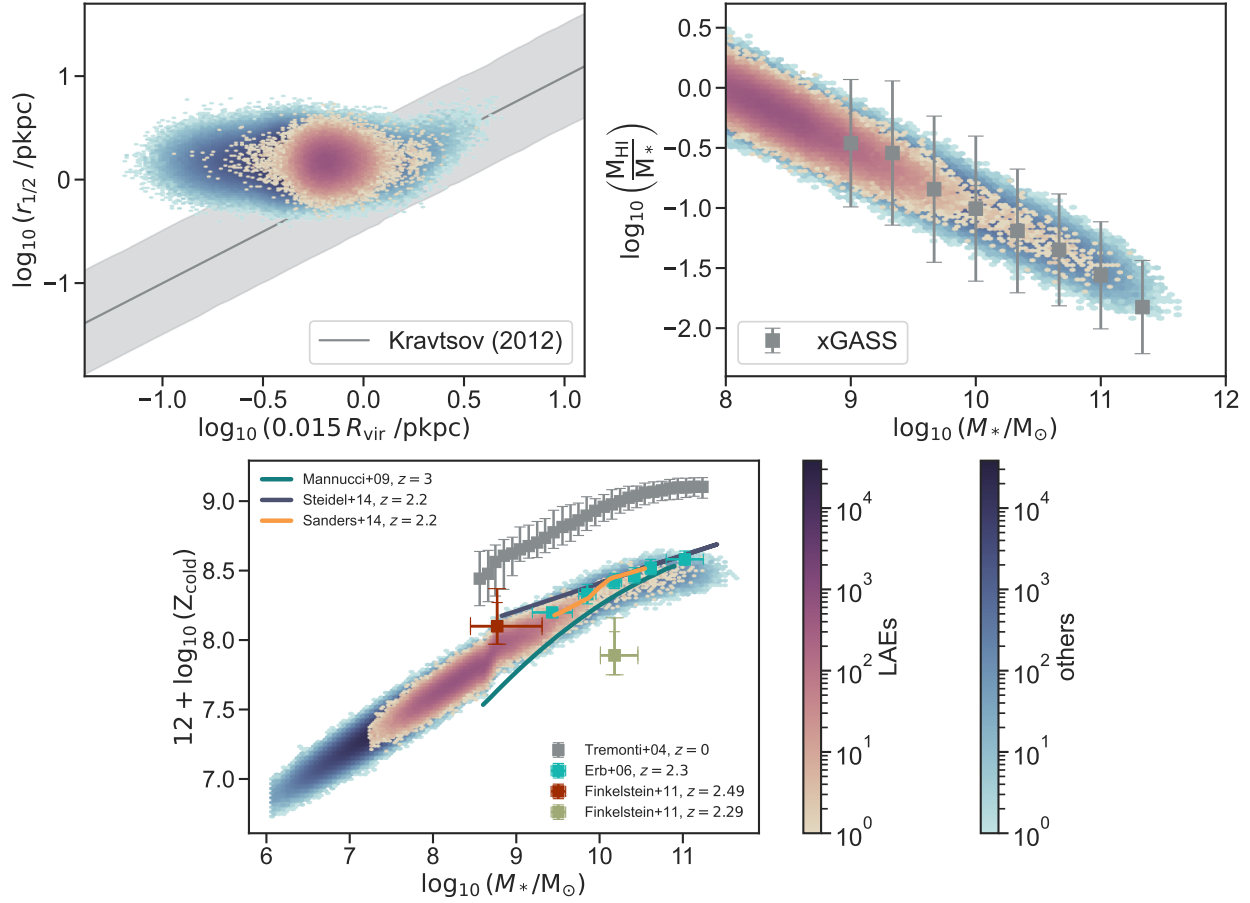


FIG. 4.— Scaling relations we adopt in this work. We show our galaxy sample at $z \sim 3$ where LAEs ($\log_{10}(L_{\text{Ly}\alpha} / \text{erg s}^{-1}) \geq 41.7$ and $\text{EW}_0 > 40 \text{ \AA}$) are shown in pink while others are represented in blue. *Top left*: Stellar half-mass radius, $r_{1/2}$, versus the halo virial radius, R_{vir} . The gray solid line represents the empirical relation $r = 0.015 R_{\text{vir}}$ from Kravtsov (2013) with the shaded region indicating the 2σ scatter. *Top right*: Neutral atomic hydrogen gas mass fraction, $\log_{10}(M_{\text{HI}}/M_*)$, as a function of stellar mass, serving as a scaling relation for inferring the neutral hydrogen column density. Measurements from the XGASS survey (Catinella et al. 2018) are shown in gray. *Bottom*: Cold gas metallicity (gas-phase oxygen abundance, $12 + \log_{10}(Z_{\text{cold}})$) as a function of stellar mass compared with several observational mass-metallicity relations including Tremonti et al. (2004); Erb et al. (2006); Mannucci et al. (2009); Finkelstein et al. (2011b); Steidel et al. (2014); Sanders et al. (2015) as depicted.

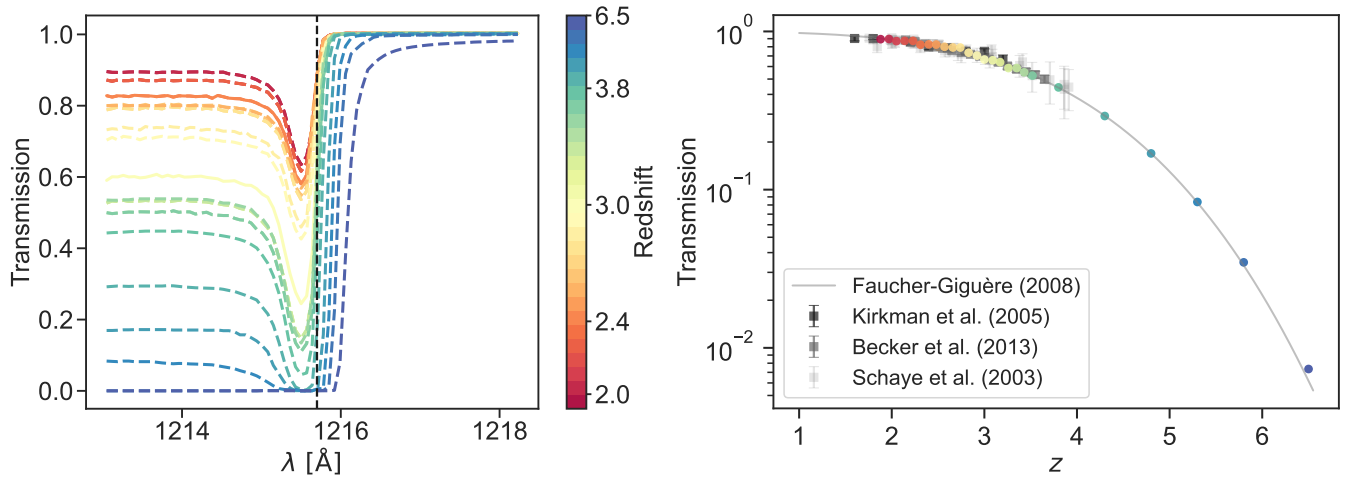


FIG. 5.— *Left*: The derived IGM transmission as a function of wavelength, color-coded for various redshifts. The vertical dashed line indicates the rest frame Ly α line center wavelength ($\lambda = 1215.7 \text{ \AA}$). Dashed curves represent the transmission function originally provided by Laursen et al. (2011), while solid curves are the ones adjusted by assuming that the mean transmission function blueward of the Ly α line follows the empirical relation represented in Eq. (15). *Right*: A comparison between observations and the model used in this study, illustrating transmitted flux blueward of the Ly α line with respect to redshift. The solid line corresponds to Eq. (15).

3.4. Modeling the Radiative Transfer of Lyman- α Photons within the Intergalactic Medium

To model the Ly α RT on IGM scales, we adopt a rather simple approach in this work. In short, we adopt a *fixed* transmission curve for all galaxies at a given redshift. Let us briefly review Ly α RT modeling on IGM scales before explaining our procedure. In an optically thin limit, the impact of Ly α RT on IGM scales is calculated by the transmission curve, $T^{\text{IGM}}(\lambda)$, and the optical depth, $\tau_{\text{IGM}}(\lambda)$, given by (Miralda-Escudé & Rees 1994; Madau 1995; Dijkstra et al. 2007; Laursen et al. 2011)

$$\tau_{\text{IGM}}(\lambda) = \int_{s_0}^{\infty} ds n_{\text{HI}}(s) \sigma \left[\lambda \left(1 + \frac{v(s) + H(z)s}{c} \right), T_{\text{HI}} \right], \quad (14)$$

$$T^{\text{IGM}}(\lambda) = \exp \{-\tau_{\text{IGM}}(\lambda)\},$$

where the integration is performed in terms of the distance from the galaxy, s . n_{HI} is the neutral hydrogen number density, $\sigma(\lambda)$ represents the cross section of neutral hydrogen in the gas rest frame that accounts for the wavelength shift due to the peculiar velocity of a galaxy in the gas rest frame, v , and the Hubble flow $H(z)$ at redshift z . This equation highlights a complexity in modeling transmission due to n_{HI} and v . Namely, we need to model both the neutral hydrogen gas density and velocity profiles at various scales. Previous studies used diverse approaches such as analytical models (Zheng & Miralda-Escudé 2002; Dijkstra et al. 2007) and hydrodynamic simulations (Laursen et al. 2011; Dayal & Ferrara 2012; Jensen et al. 2014; Gronke et al. 2018; Smith et al. 2019; Byrohl & Gronke 2020; Garel et al. 2021; Gronke et al. 2021; Park et al. 2021; Smith et al. 2022). Other approaches include absorption statistics directly from observed quasar spectra (Inoue et al. 2014; Hayes et al. 2021) or the Fluctuating Gunn-Peterson Approximation that is commonly adopted in Ly α forest studies (e.g., McDonald et al. 2000; Zaldarriaga et al. 2001; Viel et al. 2004; McDonald et al. 2005; Viel & Haehnelt 2006; McDonald et al. 2006; Bird et al. 2011; Iršič et al. 2016; Iršič et al. 2017; Baur et al. 2017; Murgia et al. 2018, 2019; du Mas des Bourboux et al. 2020; Qezlou et al. 2022; Bird et al. 2023; Hadzhiyska et al. 2023).

To model Ly α spectra, we need to model the wavelength dependence of the IGM transmission. In fact, the transmission has the largest impact around the line center, which is typically due to a large neutral hydrogen density around dark-matter halos (Laursen et al. 2011). HI gas distribution even around the CGM and IGM scales is not still converged among various hydrodynamical simulations (e.g., Faucher-Giguère et al. 2016; van de Voort et al. 2019; Villaescusa-Navarro et al. 2021). Due to these complications, we simply adopt a fixed transmission curve motivated by previous simulation work in Laursen et al. (2011) but adjust only the blue side of the transmission such that it becomes consistent with the observed mean transmission from Faucher-Giguère et al. (2008); Kirkman et al. (2005); Schaye et al. (2003).

The transmission curves in Laursen et al. (2011) were computed with $s_0 = 1.5R_{\text{vir}}$ and thus can be separated from our ISM/CGM RT calculation with the shell model. However, they were calculated at particular redshift output choices, and the blue side of their transmission curves were not fully consistent with the observed mean transmission whose redshift evolution is well described by the following form (Faucher-Giguère et al. 2008):

$$\langle T^{\text{IGM}}(\lambda = 1213\text{\AA}; z) \rangle = \exp \left\{ -1.330 \times 10^{-3} \times (1+z)^{4.094} \right\}. \quad (15)$$

In practice, we performed a Random Forest regression using a multi-output regressor to predict the IGM attenuation (Pedregosa et al. 2011). As training data, we compiled a grid of transmission curves, $T(\lambda)$, from Laursen et al. (2011), each corresponding to a fixed redshift in the range $z = 1$ to $z = 6.5$. Each input consists of the redshift value and the corresponding output as a vector of transmission sampled across the Ly α wavelength range. After formatting the data into a single matrix of shape $(N_{\text{redshift}}, N_{\lambda})$, we trained the model to learn the mapping $z \rightarrow T(\lambda)$. Once trained, the regressor was used to predict transmission curves at intermediate redshifts. This procedure allows for a smooth interpolation of IGM attenuation across redshifts. Fig. 5 shows the transmission function at different redshifts as a function of the rest-frame wavelength. We stress again that $f_{\text{esc}}^{\text{IGM}}$ depends on each galaxy property through the observed line profile $\phi^{\text{obs}}(\lambda) = \phi^{\text{ISM}}(\lambda; \vec{\theta}_g) \times T^{\text{IGM}}(\lambda; z)$, even though we fix the mean transmission curve at a given redshift. One may concern that we do not fully model the transmission in each line-of-sight dependent way (see e.g., Byrohl & Gronke 2020). We take this simple approach because we calibrate our model against the Ly α luminosity function and the angular correlation function where the impact of line-of-sight dependent transmission is expected to be minimal. In future work, we plan to model the transmission curve in each line of sight and quantify the impact of the RT on the redshift-space clustering (Zheng et al. 2011; Behrens et al. 2018).

3.5. Model calibration

In this section, we explain how we calibrate the three dimensionless free parameters in our LAE model, α , β and γ , as introduced in Eqs. (6), (7), and (8). These parameters describe the scaling of the neutral hydrogen expansion velocity, V_{exp} , neutral hydrogen column density, N_{HI} , and the dust attenuation optical depth, τ_d . The calibration process ensures that our model simultaneously reproduces both the observed Ly α luminosity function and the LAE angular correlation function at $z \sim 2$ and $z \sim 3$. These two summary statistics provide complementary information as the amplitude and shape of the luminosity function constrain the Ly α escape fraction as a function of intrinsic galaxy properties, while the LAE angular correlation function is sensitive to the properties of dark-matter halos. We show in Appendix D a detailed discussion on parameter dependence of the luminosity function as well as the angular correlation function. As described in Sec. 2.3, we calibrate our model using the luminosity function in Konno et al. (2016) and the angular correlation function in White et al. (2024) at $z \sim 2$, while we adopt the luminosity function in Ouchi et al. (2008) and the angular correlation function in White et al. (2024) at $z \sim 3$. We explore the full pa-

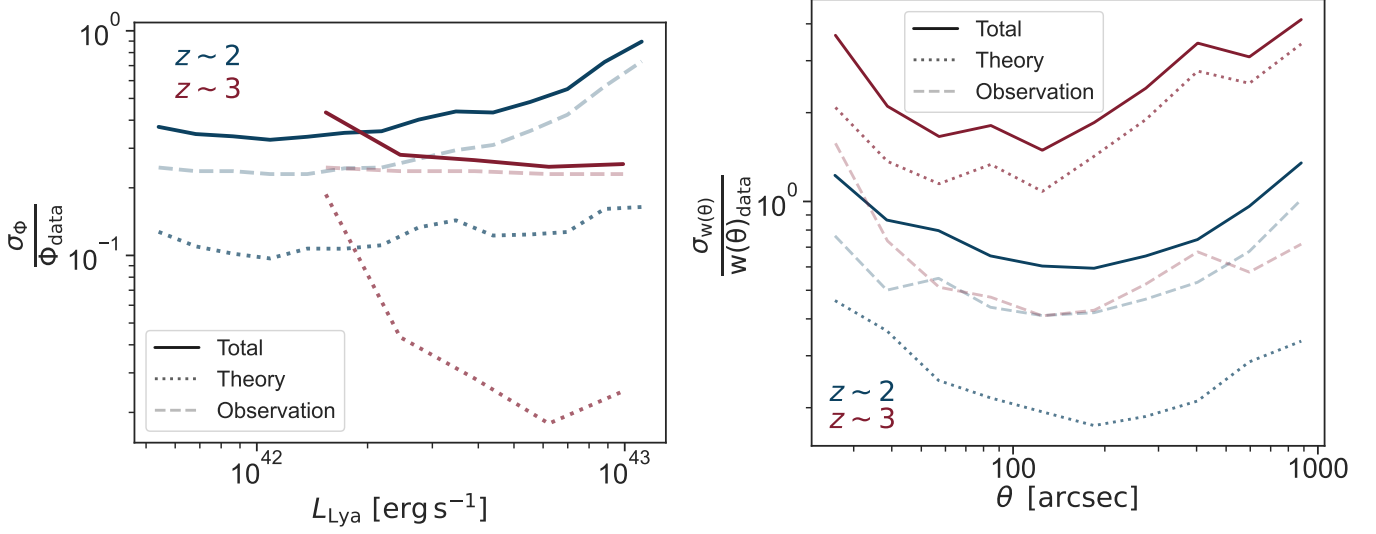


FIG. 6.— Relative error budgets for Ly α luminosity function and the angular correlation function at both redshifts. *Left:* Relative uncertainty in the luminosity function as a function of Ly α luminosity for $z \sim 2$ in blue and $z \sim 3$ in red. *Right:* Relative uncertainty in the angular correlation function as a function of angular scales with the same color scheme. In both panels, dotted curves show the theory errors from the jackknife covariance matrices, dashed curves show the observational errors from the fiducial luminosity function (left) and angular correlation function (right) measurements, and solid curves give the total error.

parameter space within the ranges $\alpha \in (0, 10]$, $\beta \in (0, 0.2]$ and $\gamma \in (0, 100]$ that we empirically find sufficiently wide for our analysis.

The luminosity function, denoted as $\Phi[\log_{10}(L_{\text{Ly}\alpha})]$, for LAEs is commonly defined as their comoving number density per logarithmic luminosity bin (Schmidt 1968):

$$\Phi[\log_{10}(L_{\text{Ly}\alpha})] = \frac{N(L_{\text{Ly}\alpha})}{V_{\text{sim}} \Delta \log_{10}(L_{\text{Ly}\alpha})}, \quad (16)$$

where $N(L_{\text{Ly}\alpha})$ is the number of LAEs in a given logarithmic luminosity bin, $V_{\text{sim}} = (400 \text{ cMpc } h^{-1})^3$ is the comoving volume of the simulation, and $\Delta \log(L_{\text{Ly}\alpha})$ is the logarithmic bin width. We measure the luminosity function using 100 logarithmic bins spanning from 10^{41} to $10^{46} \text{ erg s}^{-1}$, although we fit only up to $10^{43} \text{ erg s}^{-1}$ to avoid the AGN contribution as explained in Sec. 2.3.

The angular correlation function, $w(\theta)$, quantifies the clustering of galaxies by measuring the excess probability of finding a pair of sources at an angular separation θ compared to a random distribution Peebles (1980), defined by

$$dP_{12} = N(1 + w(\theta_{12}))d\Omega_1 d\Omega_2, \quad (17)$$

where dP_{12} represents the probability of finding two LAEs within two solid angle regions, $d\Omega_1$ and $d\Omega_2$ with an angular separation of θ_{12} given the sample's number density N . To estimate $w(\theta)$, we employ HALOTOOLS² (Hearin et al. 2017), using the Landy-Szalay estimator (Landy & Szalay 1993), expressed as:

$$w(\theta) = 1 + \left(\frac{N_R}{N_D} \right)^2 \frac{DD(\theta)}{RR(\theta)} - 2 \left(\frac{N_R}{N_D} \right) \frac{DR(\theta)}{RR(\theta)}, \quad (18)$$

where DD , DR , and RR represent the number of data–data, data–random, and random–random LAE pairs, respectively with data and random galaxies having the exact same geometry in the sky. Furthermore, N_R and N_D denote the number of random and data (LAE), respectively. Note that we prepare random particles because the angular correlation function is somewhat sensitive to the radial selection function (i.e., the width of the redshift slice). We first divided the cubic simulation box into five separate subboxes, and then transformed the 3D Cartesian coordinates into the sky coordinates. This transformation places all the galaxies in a common observer frame, ensuring a fair comparison with observational surveys. To further align our simulation with observational data, we apply different radial selection function. When comparing with White et al. (2024), at $z \sim 2$ (for the N419 filter) and $z \sim 3$ (for N501), we match their redshift distribution by adapting their redshift dependent selection function dn/dz (see Fig. 3 in White et al. (2024)) and randomly down-sample our LAEs and randoms accordingly. We also apply selection cuts to refine our sample, including a luminosity cut. To compute $w(\theta)$, we used 16 logarithmic bins spanning from 1.5 to 1505.6 arcseconds that roughly correspond to the comoving separation of 0.02 and 20 cMpc/ h in these redshifts. Note that we adopt the same angular binning size as the measurements in White et al. (2024). We repeat these processes for each subbox and average the measurements $w(\theta)$ in the five subboxes.

² <https://halotools.readthedocs.io/en/latest/>

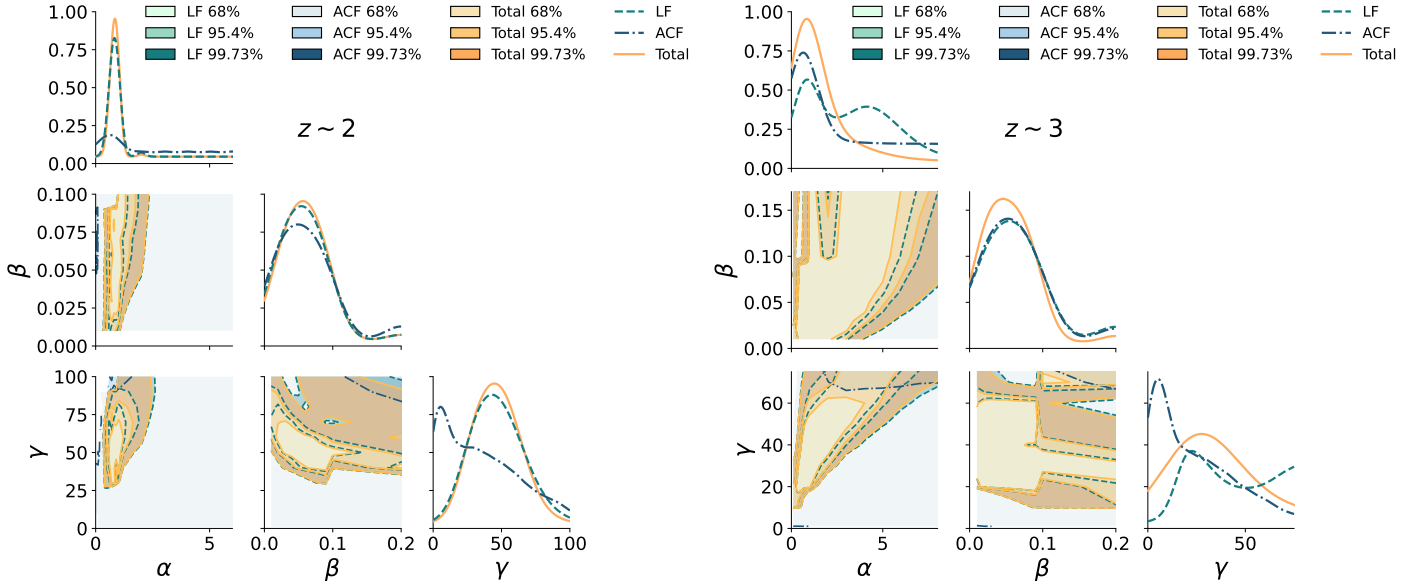


FIG. 7.— Corner plots showing the parameter constraints for α , β and γ at $z \sim 2$ (left) and $z \sim 3$ (right). The contours represent the 1σ (68%), 2σ (95.4%), and 3σ (99.73%) confidence intervals, with darker colors corresponding to the higher-confidence regions. The parameter constraints are derived from fitting the Lyman- α luminosity function (LF, green), the angular correlation function (ACF, blue), and the combined total fit (yellow). We also show the one-dimensional likelihood function, $\exp(-\chi^2/2)$, marginalized over other two parameters and normalized to one at those best-fitting values.

Due to the limited simulation box size ($L_{\text{box}} = 400 \text{ cMpc } h^{-1}$), we estimate the theoretical covariance matrix of the luminosity function and the angular correlation function from our simulation. We adopt the jackknife (JK) resampling method (Norberg et al. 2009) given by

$$C_{ij}^{\text{th}} = \frac{(N_{\text{JK}} - 1)}{N_{\text{JK}}} \sum_{k=1}^{N_{\text{JK}}} (x_i^k - \bar{x}_i)(x_j^k - \bar{x}_j). \quad (19)$$

The total sample is divided into $N_{\text{JK}} = 50$ jackknife subregions only in the RA-Dec positions with the κ -MEANS³ algorithm (Kwan et al. 2017). x_i^k represents the measurements of the summary statistics in the i -th bin, computed using all jackknife regions except the k -th one, while \bar{x}_i is the mean of all resamplings. We use the best-fitting model that we will show in the next section to evaluate the jackknife theoretical errors. In Fig. 6, we show the estimated theoretical errors (dotted lines) for the luminosity function (left) and the angular correlation function (right), and compare them with the observation measurement (dashed lines) and the total errors (solid lines) at $z \sim 2$ (blue) and $z \sim 3$ (red). For the luminosity function, the theoretical errors are subdominant, since our simulation volume is much larger than the observed ones. Meanwhile, for the angular correlation function, the theoretical error is not negligible, and larger than the measurement error at $z \sim 3$. Our simulation volume is larger than that of White et al. (2024) by a factor of ~ 2.6 at both $z \sim 2$ and $z \sim 3$. In addition, we downsample our LAEs to match the selection function in White et al. (2024) to ensure the same number density. Therefore, the larger theoretical error at $z \sim 3$ could be explained by the overestimated cosmic variance of the jackknife method. We leave the investigation of this issue with a larger box simulation for future work. We also find the off-diagonal elements of the covariance matrix too noisy to stably conduct the parameter estimation, and thus ignore them for simplicity.

We determine the best-fitting free parameters and their uncertainties by calculating χ^2 (or the likelihood function $\exp(-\chi^2/2)$) given by

$$\chi^2 = \sum_i^n \frac{(x_i^{\text{obs}} - x_i^{\text{th}})^2}{(\Delta x_i)^2}, \quad (20)$$

where x_i denotes either the luminosity function or the angular correlation function at i -th bin, and $(\Delta x)^2 = (\Delta x^{\text{obs}})^2 + C_{ii}^{\text{th}}$ combines uncertainties from the observations and theoretical predictions. As noted above, we ignore the correlation among different bins, and thus the total χ^2 is simply the sum of two contributions from the luminosity function and the angular correlation function, $\chi_{\text{tot}}^2 = \chi_{\text{LF}}^2 + \chi_{\text{ACF}}^2$.

4. RESULTS

In this section, we present the results of our LAE model calibration and compare our simulated LAEs with observational measurements at $z \sim 2$ and $z \sim 3$. This section is organized as follows. We first describe the best-fit parameters obtained from

³ <https://github.com/esheldon/kmeans-radec>

TABLE 1.— Summary of best-fit parameters at two redshifts. The first column lists each quantity, the second column shows its value at $z \sim 2$, and the third column shows the corresponding value at $z \sim 3$.

Redshift	$z \sim 2$	$z \sim 3$
Luminosity Function (N_{bin})	Konno et al. (2016) ($N_{\text{bin}} = 13$)	Ouchi et al. (2008) ($N_{\text{bin}} = 5$)
Angular Correlation Function [f_{cont}] (N_{bin})	White et al. (2024) [8%] ($N_{\text{bin}} = 10$)	White et al. (2024) [11%] ($N_{\text{bin}} = 10$)
$\chi^2_{\text{tot}} = \chi^2_{\text{LF}} + \chi^2_{\text{ACF}}$	$4.71 = 2.00 + 2.71$	$1.90 = 0.06 + 1.84$
(α, β, γ)	$(0.90^{+0.21}_{-0.16}, 0.07 \pm 0.03, 50.00^{+16.33}_{-17.94})$	$(0.80^{+0.61}_{-0.52}, 0.04 \pm 0.03, 30.00^{+23.21}_{-10.01})$
$\bar{M}_h \left(\log(L/\text{erg s}^{-1}) \geq 41.7, \text{EW}_0 > 40 \text{ \AA} \right) M_{\odot}/h$	1.12×10^{11}	1.41×10^{11}
$f_{\text{sat}} \left(\log(L/\text{erg s}^{-1}) \geq 41.7, \text{EW}_0 > 40 \text{ \AA} \right)$	12.37%	8.86%
$\bar{M}_h \left(\log(L/\text{erg s}^{-1}) \geq 42.22, \text{EW}_0 > 40 \text{ \AA} \right) M_{\odot}/h$	2.06×10^{11}	1.55×10^{11}
$f_{\text{sat}} \left(\log(L/\text{erg s}^{-1}) \geq 42.22, \text{EW}_0 > 40 \text{ \AA} \right)$	10.06%	8.67%

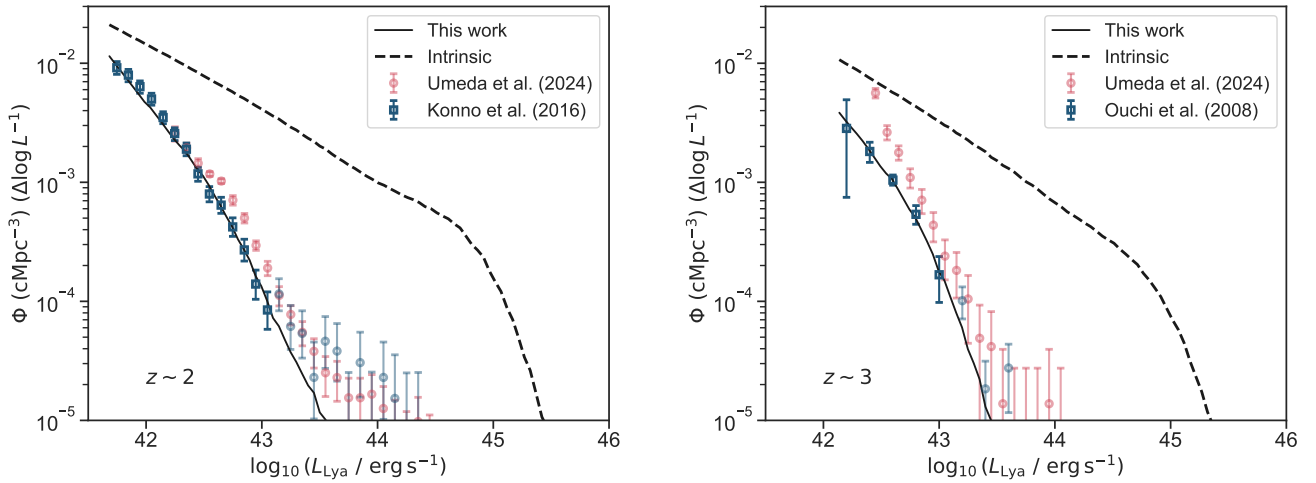


FIG. 8.— Lyman- α luminosity function for our best-fit model at $z \sim 2$ (left panel) and $z \sim 3$ (right panel). The solid black line shows our best-fit model, while the black dashed line indicates the intrinsic luminosity function as computed from Eq. (2). The blue data points represent the observational data at each redshift, while the fainter blue data points are not used to avoid contamination from AGNs (see Sec. 2.3). For comparison, we also show the measurements in Umeda et al. (2025) (faint red points).

our modeling approach and discuss their impact on the inferred Lyman- α properties. We then compare the observational LAE properties, such as Lyman- α escape fractions, equivalent width distributions, and observed Lyman- α velocity offsets, with our model predictions. Lastly, we present the implications and predictions of our LAE model, including the escape fraction and the LAE-halo connection. We will investigate the relationship between LAEs and their host dark-matter halos, specifically predicting the Halo Occupation Distribution (HOD) and potential assembly bias signatures.

4.1. Parameter constraints and model fitting

Fig. 7 displays the resulting parameter constraints and the likelihood (normalized to one at the best-fit values) for α, β and γ . The contours correspond to the 1σ (68%), 2σ (95.4%) and 3σ (99.73%) confidence intervals. Darker colors indicate higher confidence intervals. We notice that the angular correlation function weakly constrains the parameter space. This is expected since the angular correlation function has larger errors than the luminosity function in our setup (see Fig. 6). In addition, the angular correlation function is primarily sensitive to the halo bias, and thus our results show that the LAE clustering only does not constrain a detailed model of the Lyman- α escape fraction. Meanwhile, the Ly α escape fraction can be well constrained by the amplitude and shape of the luminosity function. We confirm expected degeneracies among the three free parameters constrained by the luminosity function. A larger escape fraction can be achieved by either a larger α , a smaller β , or a smaller γ , as discussed in Sec. 3. However, α and γ are relatively well constrained by the luminosity function, since α mainly changes the slope, while γ changes the overall amplitude as demonstrated in Fig. 28 in Appendix D.1. β is the parameter most weakly constrained by both the luminosity function and the angular correlation function, while it is essential to have β in this range to recover the observed velocity offset measurement, as we discuss in the next subsection.

We present the best-fitting values of the model parameters and the goodness of fit, χ^2 , in Table. 1. Although we find that our best-fitting model is consistent with the observed measurements, the χ^2 values tend to be small; we obtain $\chi^2_{\text{tot}} = 4.7$ for $20 = 13 + 10 - 3$ degrees of freedom at $z \sim 2$. This is most likely because our theory errors are overestimated and/or due to the fact that we ignored the correlation among different bins for both theoretical and observational measurements. Nevertheless, it

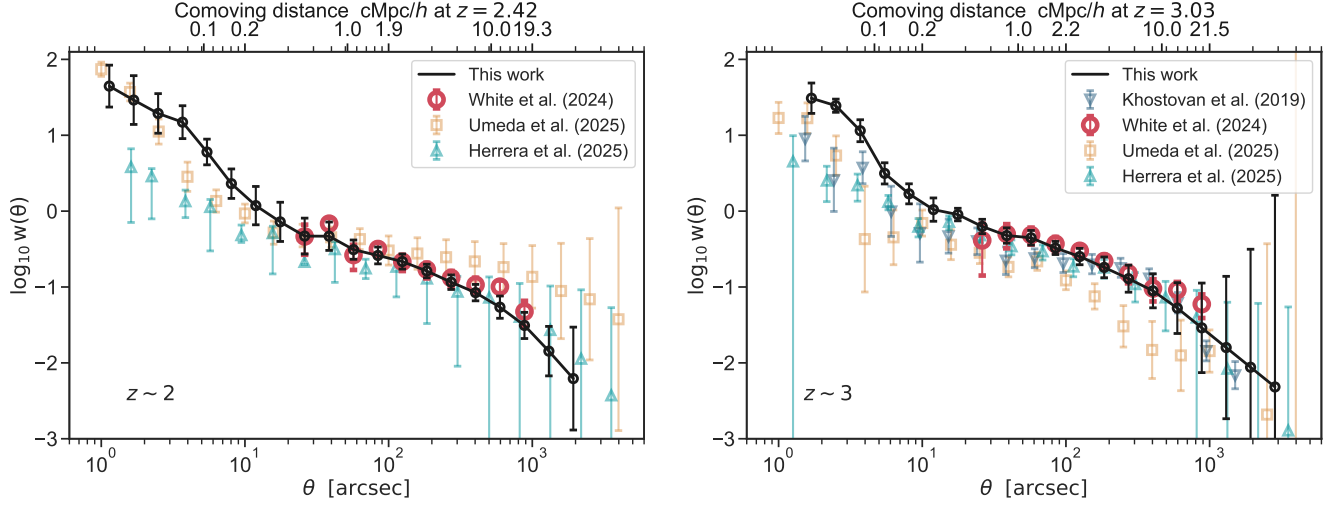


FIG. 9.— Angular correlation function, $w(\theta)$, predictions for our fiducial model compared with observational data at $z \sim 2$ (left) and at $z \sim 3$ (right). In both panels the black curve shows the best-fit model with the White et al. (2024) dataset, which incorporates the redshift distribution (dn/dz), luminosity threshold, and contamination fraction. For reference, we compare other observational measurements; Khostovan et al. (2019) (blue triangle) at $z \sim 3$, Umeda et al. (2025) (orange square) and Herrera et al. (2025) (green triangle) at both $z \sim 2$ and $z \sim 3$. Note that $w(\theta)$ is highly sensitive to the redshift interval since it measures the projected clustering in RA–Dec; a broader redshift range would result in a different projection and clustering amplitude. Error bars in each bin were estimated from the diagonal elements of the covariance matrix computed via jackknife resampling.

is highly encouraging that the best-fit results of (α, β, γ) of two redshifts are consistent within these uncertainties. This is one of the successes of our model, since a single set of (α, β, γ) can simultaneously explain the observational measurements at two independent redshifts. This fact also justifies our various assumptions in the scaling relations (see Sec. 3.3), since it does not require an additional redshift evolution.

We compare our best-fit predictions of the luminosity function in Fig. 8. In both left ($z \sim 2$) and right ($z \sim 3$) panels of Fig. 8, our best-fit model consistently traces the fitted observational data points (thick blue points). Our prediction is clearly underestimated at $\log_{10}(L_{\text{Ly}\alpha} / \text{erg s}^{-1}) > 43.0$ compared to the thick blue points, which could be explained by the contribution of AGNs. We also show the intrinsic $\text{Ly}\alpha$ luminosity function (dashed line), whose difference from the best-fit model is the consequence of our escape fraction modeling. For comparison, we overplot another observational measurement from Umeda et al. (2025). Interestingly, there are non-negligible discrepancies between the two measurements. In Appendix. C.1, we also show the results fitted to the luminosity function in Umeda et al. (2025).

The comparison of the angular correlation function is also presented in Fig. 9. At both $z \sim 2$ (left) and $z \sim 3$ (right), our best-fitting model is consistent with the observational data in White et al. (2024) (large red circle points). Notice that the observational data in White et al. (2024) only cover the two-halo regime, since a typical virial radius of LAEs is given by $\sim 200 \text{ pkpc}/h$ (see Fig. 4), which roughly corresponds to 30 and 40 arcseconds at $z \sim 2$ and $z \sim 3$, respectively. In this sense, the angular correlation function in the 1-halo regime is purely a prediction of our best-fitting model. For reference, we compare other observational measurements; Khostovan et al. (2019) (blue triangle) at $z \sim 3$, Umeda et al. (2025) (orange square) and Herrera et al. (2025) (green triangle) at both $z \sim 2$ and $z \sim 3$. It may seem that our model overestimates the 1-halo term in comparison to these measurements, but we stress that this is not a fair comparison, since the different measurements have different selection criteria in terms of luminosity threshold and radial selection function. As an example, we show in Appendix. C.2 that we can reproduce the Khostovan et al. (2019) measurements (including the 1-halo term regime) with a different set of free parameters.

4.2. Other observational supports

We have shown that our LAE model successfully reproduces the $\text{Ly}\alpha$ luminosity function and the angular correlation function at $z \sim 2$ and 3. However, a natural question is if our best-fit parameters of (α, β, γ) physically make sense. Since they are all parameters that are supposed to only effectively capture $\text{Ly}\alpha$ RT physics, it is not straightforward to interpret the direct physical meaning of the best-fit values obtained. Instead, we will check the ability of our LAE model to match additional observables, thereby providing further validation. Note that it is not straightforward to make a fair comparison for most of the following observables, since a different data set has different LAE selection criteria. We stress that we did not fit the observables in this subsection to derive our best-fit LAE model.

A relation between $\text{Ly}\alpha$ emissions and UV luminosity can be used as a diagnostic to check how LAEs are populated in the entire young star-forming galaxy population. Fig. 10 presents the rest-frame $\text{Ly}\alpha$ equivalent width (EW_0) distribution for our simulated LAEs at redshifts $z \sim 2$ and $z \sim 3$. In both panels, the histograms indicate a steep exponential decline, well described by a normalized probability density function of the form $P(\text{EW}_0) = (1/\text{EW}_{0,e}) \exp(-\text{EW}_0/\text{EW}_{0,e})$ (dark blue line). We find

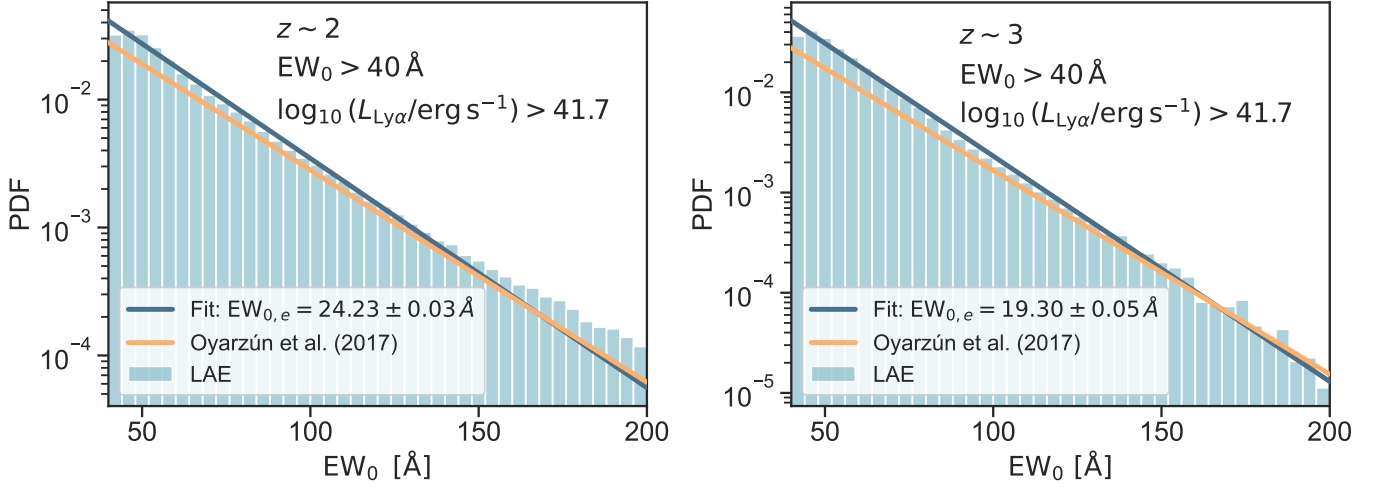


FIG. 10.— The probability density function (PDFs) of the rest-frame $\text{Ly}\alpha$ equivalent widths (EW_0) for our fiducial LAE samples at $z \sim 2$ (left) and $z \sim 3$ (right). Histograms show the EW_0 distributions for LAEs with $40 < \text{EW}_0 < 200$, and a luminosity cut of $\log_{10}(L_{\text{Ly}\alpha}/\text{erg s}^{-1}) > 41.7$, all normalized to unit area. The dark blue solid line represents the best-fit exponential function, $P(\text{EW}_0) = (A/\text{EW}_{0,e}) \exp(-\text{EW}/\text{EW}_{0,e})$, to our LAE model. The orange solid line is the Oyarzún et al. (2017) exponential fit, re-normalized over the same EW_0 range.

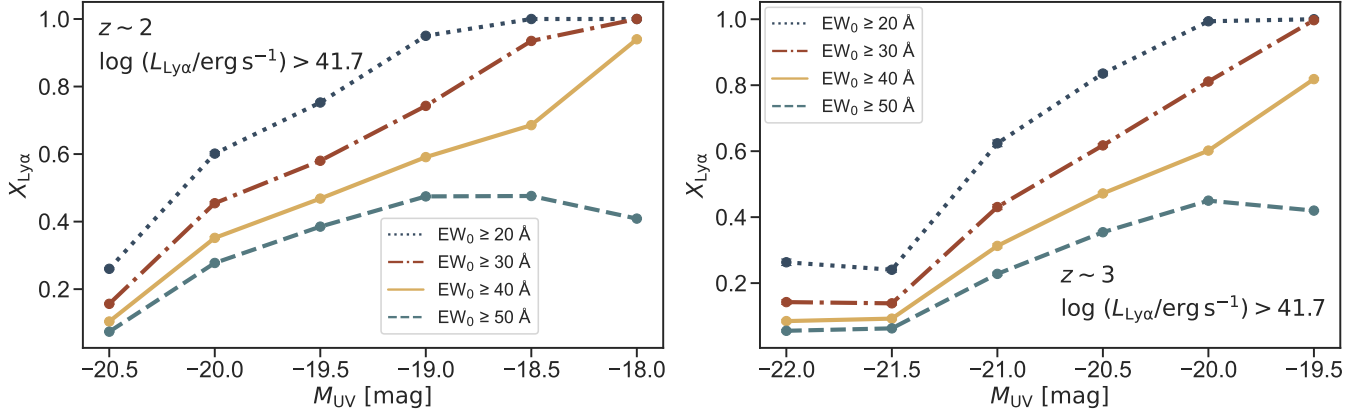


FIG. 11.— Fraction of galaxies displaying observable Lyman- α emission ($X_{\text{Ly}\alpha}$) as a function of rest-frame UV absolute magnitude (M_{UV}) for different $\text{Ly}\alpha$ equivalent width (EW) thresholds. The left and right panels present our model predictions at $z \sim 2$ and $z \sim 3$, respectively. Line colors and styles correspond to different minimum EW cuts. In both panels, a fixed $\text{Ly}\alpha$ luminosity threshold of $\log_{10}(L_{\text{Ly}\alpha}/\text{erg s}^{-1}) > 41.7$ is applied. The error bars are derived from Poisson error propagation: $\sigma_{X_{\text{Ly}\alpha}} = (N_{\text{LAE}}/N_{\text{UV}}^2 + N_{\text{LAE}}^2/N_{\text{UV}}^3)^{1/2}$, where N_{LAE} is the number of $\text{Ly}\alpha$ emitters and N_{UV} is the total number of continuum-detected galaxies in each M_{UV} bin.

a characteristic scale $\text{EW}_{0,e} = 24.23 \pm 0.03 \text{ \AA}$ at $z \sim 2$ and $\text{EW}_{0,e} = 19.30 \pm 0.05 \text{ \AA}$ at $z \sim 3$, indicating most LAEs have moderate equivalent widths. For comparison the orange solid line shows the exponential distribution from Oyarzún et al. (2017) ($\text{EW}_{0,e} \sim 38 \text{ \AA}$ for their M_* -selected sample at $z \sim 3 - 4.6$), re-normalized over $40 < \text{EW}_0 < 200 \text{ \AA}$ to match our histogram's range. The exponential form and scale of our prediction are in good agreement with observations, though minor discrepancies (slight over-estimation at low EW_0 and underestimation at high EW_0) are expected given sample differences ($\text{Ly}\alpha$ -luminosity selected sample in this work vs. mass-selected sample in Oyarzún et al. (2017) as well as the redshift range differences) and observational limitations (relatively small size of Oyarzún et al. (2017) sample) increasing fit uncertainties. Too many small EW objects could be explained by the fact that we include LAEs down to relatively small $\text{Ly}\alpha$ luminosity, $\log_{10}(L_{\text{Ly}\alpha}/\text{erg s}^{-1}) > 41.7$. Too few large EW at $z \sim 3$ could be explained by the lack of AGNs or bright $\text{Ly}\alpha$ sources at $\log_{10}(L_{\text{Ly}\alpha}/\text{erg s}^{-1}) > 43$ in our model.

Another way to check the relation with the UV SFR is the fraction of LAEs as a function of UV magnitude. Fig. 11 quantifies the fraction of LAEs, defined as $X_{\text{Ly}\alpha}$, as a function of rest-frame UV magnitude (M_{UV}) for different equivalent width (EW) thresholds. Specifically, we calculate:

$$X_{\text{Ly}\alpha}(M_{\text{UV}}, \text{EW}_{\min}) = \frac{N_{\text{LAE}}(M_{\text{UV}}, \text{EW} \geq \text{EW}_{\min}, L_{\text{Ly}\alpha} \geq L_{\min})}{N_{\text{UV}}(M_{\text{UV}}, L_{\text{Ly}\alpha} \geq L_{\min})}, \quad (21)$$

where N_{LAE} is the number of LAEs in a given M_{UV} bin that meet both the EW and $\text{Ly}\alpha$ luminosity thresholds, and N_{UV} is the total number of continuum-selected sources above the same luminosity threshold. For this analysis, we adopt $\log_{10}(L_{\text{Ly}\alpha}/\text{erg s}^{-1}) > 41.7$. Statistical uncertainties on $X_{\text{Ly}\alpha}$ are simply estimated by the Poisson error. As expected, at both

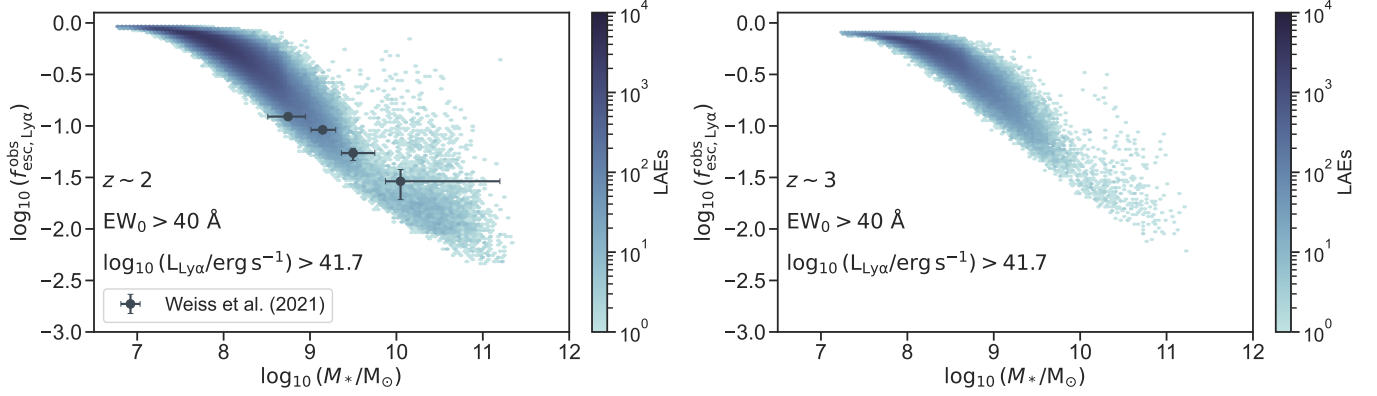


FIG. 12.— Observed Ly α escape fraction ($f_{\text{esc, Ly}\alpha}^{\text{obs}}$) as a function of stellar mass (M_*) for individual LAEs in our fiducial model at $z \sim 2$ (left) and $z \sim 3$ (right). The colored scatter points show simulated LAEs with observed Ly α luminosities above $\log_{10}(L_{\text{Ly}\alpha}/\text{erg s}^{-1}) > 41.7$ and rest-frame equivalent width $\text{EW}_0 > 40 \text{ \AA}$. Dark data points with error bars represent observational measurements from [Weiss et al. \(2021\)](#), who inferred $f_{\text{esc, Ly}\alpha}^{\text{obs}}$ using stacked Ly α and H β emission from a large sample of [OIII]-selected galaxies at $1.9 \leq z \leq 2.35$. Our model qualitatively reproduces the observed trend of decreasing escape fraction with increasing stellar mass.

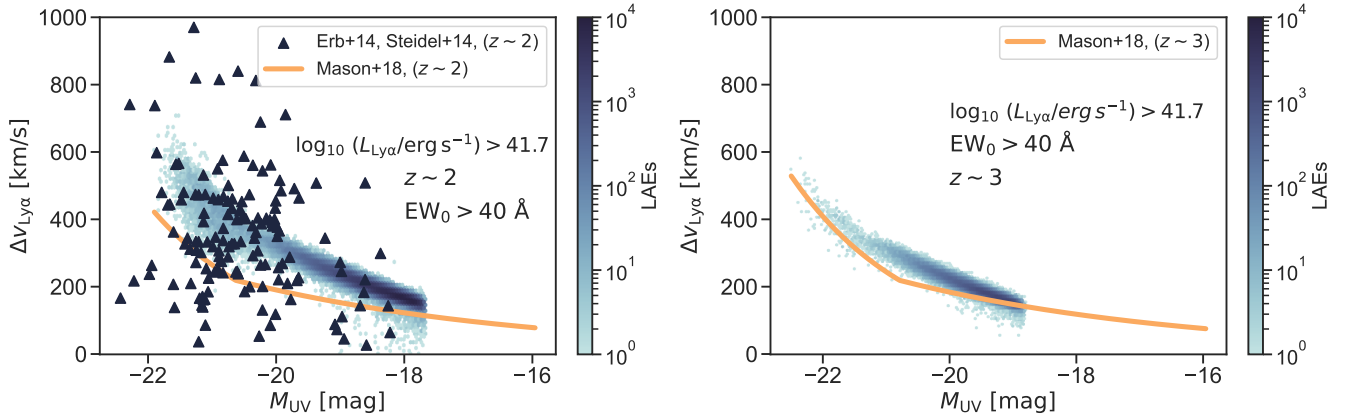


FIG. 13.— Lyman- α velocity offset ($\Delta v_{\text{Ly}\alpha}$) as a function of rest-frame UV absolute magnitude (M_{UV}) for simulated LAEs (shaded area with the color-bar) at $z \sim 2$ (left) and $z \sim 3$ (right). The simulated points correspond to galaxies with $\log_{10}(L_{\text{Ly}\alpha}/\text{erg s}^{-1}) > 41.7$ and $\text{EW}_0 > 40 \text{ \AA}$. Observational data from [Erb et al. \(2014\)](#) and [Steidel et al. \(2014\)](#) are represented by dark blue triangles at $z \sim 2$. The orange solid line depicts the prediction from [Mason et al. \(2018\)](#) who empirically modeled the median velocity offset as a function of UV magnitude and redshift via halo abundance matching as $\log_{10} \Delta v_{\text{Ly}\alpha} = 0.32 \gamma (M_{\text{UV}} + 20.0 + 0.26z) + 2.34$, where $\gamma = -0.3$ for $M_{\text{UV}} \geq -20 - 0.26z$ and $\gamma = -0.7$ otherwise.

redshifts, at a given UV magnitude, the fraction of galaxies displaying observable Ly α emission naturally decreases as the EW threshold increases, simply because higher EW threshold exclude galaxies with weaker Ly α emission. This trend indicates that galaxies with higher Ly α EW represent a smaller fraction of the overall galaxy population at these UV magnitudes. For instance at $M_{\text{UV}} \sim -20$, for $\text{EW}_0 \geq 20 \text{ \AA}$, more than $\sim 60\%$ of the galaxies are LAEs, while for $\text{EW}_0 \geq 50 \text{ \AA}$ this fraction lowers to $\sim 20\%$ at $z \sim 2$. At both $z \sim 2$ and $z \sim 3$, our results indicate a clear trend: the fraction of galaxies showing strong Ly α emission increases toward fainter UV magnitudes. This trend becomes especially prominent at higher EW thresholds ($\geq 40 \text{ \AA}$, $\geq 50 \text{ \AA}$), suggesting that galaxies with lower UV luminosities are more likely to host physical conditions that facilitate greater Ly α escape. These trends predicted by our model, are qualitatively consistent with observations (e.g., [Stark et al. 2011](#); [Caruana et al. 2017](#); [Kusakabe et al. 2020](#)).

We next investigate how the Ly α escape fraction varies with stellar mass in our simulated LAE population. Fig. 12 shows $f_{\text{esc, Ly}\alpha}^{\text{obs}}$ as a function of M_* for individual LAEs at $z \sim 2$ and $z \sim 3$, selected with $\text{EW}_0 > 40 \text{ \AA}$ and $\log(L_{\text{Ly}\alpha}/\text{erg s}^{-1}) > 41.7$. In both redshift bins, our model exhibits a clear declining trend in $f_{\text{esc, Ly}\alpha}^{\text{obs}}$ with increasing stellar mass. This behavior emerges naturally from our radiative transfer prescriptions, where more massive galaxies typically host denser HI and dustier interstellar media, resulting in more significant attenuation of Ly α photons. We compare our model predictions with the binned observational measurements from [Weiss et al. \(2021\)](#), who analyzed the Ly α escape fraction of [OIII]-emitting galaxies between $1.9 \leq z \leq 2.35$. Their escape fractions were estimated by stacking UV grism spectra from HST to measure H β and combined with Ly α fluxes from HETDEX. By comparing the stacked H β /Ly α ratios, they inferred how $f_{\text{esc, Ly}\alpha}^{\text{obs}}$ varies with stellar mass and other galaxy properties. Their analysis identified stellar mass and internal extinction as the dominant factors that regulate Ly α escape, as naturally predicted by our LAE model.

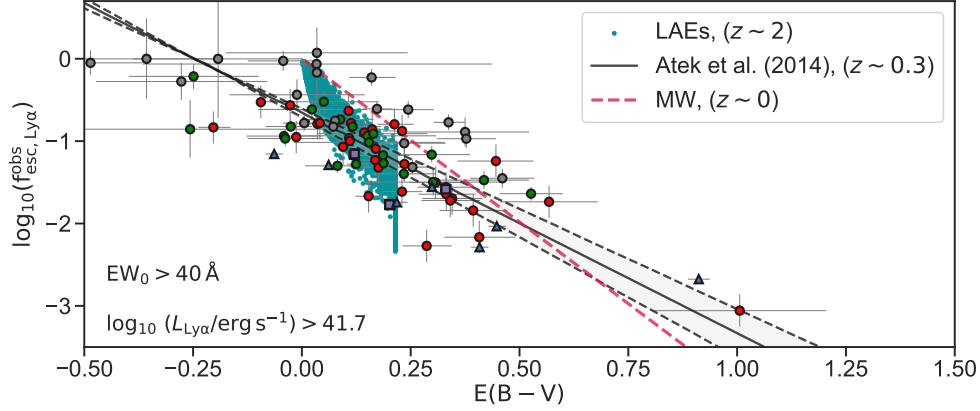


FIG. 14.— Observed $\text{Ly}\alpha$ escape fraction ($f_{\text{esc}, \text{Ly}\alpha}^{\text{obs}}$) as a function of dust reddening $E(B - V)$ for our LAEs at $z \sim 2$. Green points show individual LAEs with $\log(L_{\text{Ly}\alpha}/\text{erg s}^{-1}) > 41.7$ and $\text{EW}_0 > 40 \text{ \AA}$. The $E(B - V)$ values are derived from the model dust attenuation (see Eq. (8)) via the Calzetti et al. (2000) attenuation law using $E(B - V) = \tau_a \times 1.086/R_V$ with $R_V = 4.05$. For comparison, we include empirical fits from Atek et al. (2014) (black line), who studied local star-forming galaxies, and the Milky Way extinction law (red dashed line). Our results show a broad agreement with observed trends, particularly the anti-correlation between $f_{\text{esc}, \text{Ly}\alpha}^{\text{obs}}$ and $E(B - V)$, which is a hallmark of dust-regulated $\text{Ly}\alpha$ escape. The observational data points shows selected LAEs at $z \sim 0.3$ as well as local measurements ($z \sim 0$) from the following studies: Gray circles show GALEX-selected LAEs at $z \sim 0.3$ (Martin et al. 2005) from Atek et al. (2014); green circles are from Scarlata et al. (2009) and red circles from Cowie et al. (2011), both also at $z \sim 0.3$. Blue triangles compile local ($z \sim 0$), “net” $\text{Ly}\alpha$ emitters observed with IUE Boggess et al. (1978), i.e. galaxies whose IUE spectra retain net $\text{Ly}\alpha$ emission after accounting for absorptions. Purple squares show nearby starbursts imaged in HST/ACS (Atek et al. 2008).

A systemic velocity offset is an indicator of the $\text{Ly}\alpha$ radiative transfer. Fig. 13 illustrates the relationship between the $\text{Ly}\alpha$ velocity offset, defined as the offset between the rest-frame intrinsic $\text{Ly}\alpha$ wavelength ($\lambda_{\text{Ly}\alpha} = 1215.67 \text{ \AA}$) and the position of the red peak, given by $\Delta v_{\text{Ly}\alpha} = c(\lambda_{\text{peak}}/\lambda_{\text{Ly}\alpha} - 1)$. The simulated galaxies in both panels (shaded area color-coded by density) represent LAEs selected with rest-frame $\text{Ly}\alpha$ equivalent width $\text{EW}_0 > 40 \text{ \AA}$ and a luminosity threshold of $\log_{10}(L_{\text{Ly}\alpha}/\text{erg s}^{-1}) > 41.7$. We compare our results with observational measurements obtained by Erb et al. (2014) and Steidel et al. (2014) for galaxies at similar redshifts ($z \sim 2$). Furthermore, we include the analytic relation derived from Mason et al. (2018), which describes the median velocity offset as a function of UV luminosity and redshift. This relation was constructed by combining semi-analytic modeling and abundance matching techniques, adopting a redshift-dependent halo velocity offset relation and translating it into an observable M_{UV} dependence $\log_{10} \Delta v_{\text{Ly}\alpha} = 0.32 \gamma (M_{\text{UV}} + 20.0 + 0.26z) + 2.34$, where the slope parameter γ transitions between two regimes: $\gamma = -0.3$ at fainter luminosities ($M_{\text{UV}} \geq -20 - 0.26z$) and $\gamma = -0.7$ at brighter luminosities. Our LAEs show a clear decline in $\text{Ly}\alpha$ velocity offset toward fainter UV magnitudes, consistent with both observational data and the analytical predictions of Mason et al. (2018). We also find that the amplitude of the velocity offset is highly correlated with β or N_{HI} . For example, we could have a model with much larger β (say $\beta \sim 50$) but much smaller γ (say $\gamma \sim 1$) that fits only to the LAE luminosity function. However, we find that such a model gives too large a velocity offset, inconsistently with the range shown here.

Finally, let us check the strength of the dust reddening. Fig. 14 explores the relationship between the observed $\text{Ly}\alpha$ escape fraction ($f_{\text{esc}, \text{Ly}\alpha}^{\text{obs}}$) as a function of the dust reddening $E(B - V)$ for our LAEs at $z \sim 2$ and $z \sim 3$ (green points). To directly compare with observational studies, we convert the model-derived dust optical depth τ_a (computed via Eq. (8)) into $E(B - V)$ using the Calzetti et al. (2000) attenuation law, commonly adopted for actively star-forming galaxies. Specifically, we adopt $E(B - V) = 1.086\tau_a/R_V$ with $R_V = 4.05$. Interestingly, the range of $f_{\text{esc}, \text{Ly}\alpha}^{\text{obs}}$ and $E(B - V)$ for our LAEs is consistent with the observational results in Atek et al. (2014). In addition, we confirm a clear negative correlation between $f_{\text{esc}, \text{Ly}\alpha}^{\text{obs}}$ and $E(B - V)$: galaxies with higher dust content tend to have lower observed $\text{Ly}\alpha$ escape fractions. This trend is consistent with observational results from Atek et al. (2014), who derived similar relations for local star-forming galaxies based on GALEX and $\text{H}\alpha$ data. We overlay their best-fit relation (black line) and the theoretical Milky Way extinction curve (red dashed) for comparison. We note that $E(B - V)$ is observationally derived from the Balmer decrement that generally shows that the dust attenuation for emission lines tend to be greater than that for the stellar continuum (see e.g., Calzetti et al. 2000; Kashino et al. 2013; Saito et al. 2020). This fact would be consistent with the high value of $\gamma \sim O(10) \gg 1$. A potential caveat of this comparison is that all the observational data points are derived at $z \sim 0$. We do not see a strong evolution in our LAE model prediction from $z \sim 3$ to $z \sim 2$.

4.3. Implications of our LAE model

So far we have discussed observational results that support our LAE modeling. In this section, we focus instead on *predictions* and *implications* of our LAE model.

4.3.1. $\text{Ly}\alpha$ escape fraction

A simple question to ask is why massive galaxies are not considered LAEs at $z = 2-3$ in our model. Is it because star formation in massive galaxies is quenched and thus intrinsic $\text{Ly}\alpha$ luminosity is small, or because massive galaxies tend to have smaller $\text{Ly}\alpha$

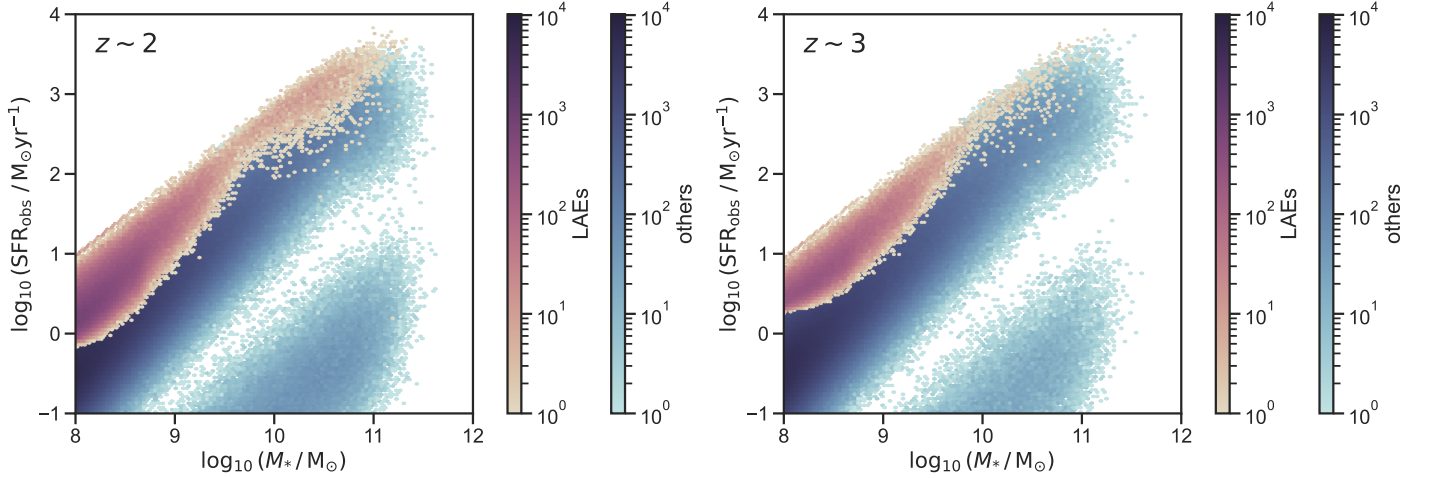


FIG. 15.— The relation between stellar mass M_* and SFR for LAEs ($(\log_{10}(L_{\text{Ly}\alpha}/\text{erg s}^{-1}) > 41.7$ and $\text{EW}_0 > 40 \text{ \AA}$) (in pink) and others (in blue) at $z \sim 2$ (left) and $z \sim 3$ (right).

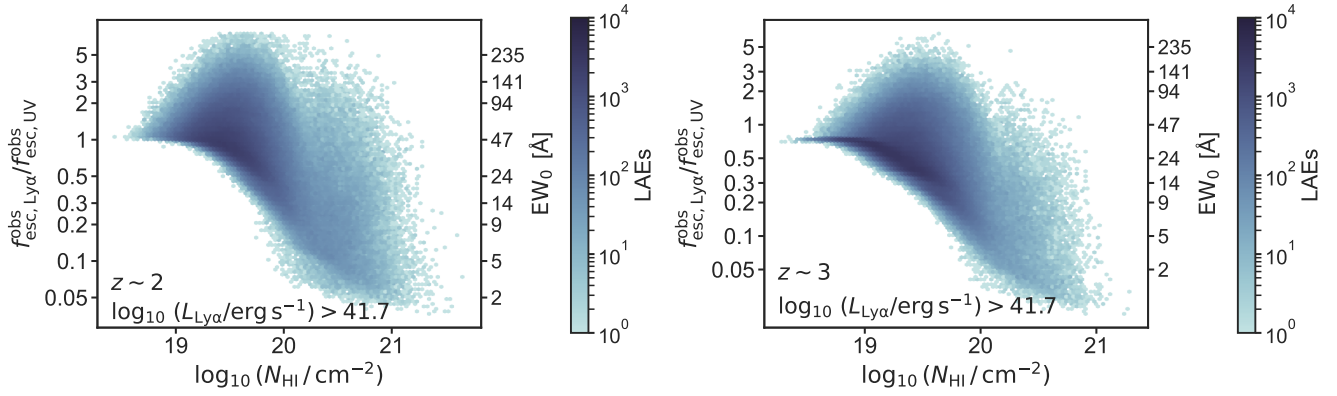


FIG. 16.— Ratio of Lyman- α to UV photon escape fractions ($f_{\text{esc,Ly}\alpha}^{\text{obs}}/f_{\text{esc,UV}}^{\text{obs}}$) as a function of neutral hydrogen column density (N_{HI}) (x-axis) and the rest-frame Ly α equivalent width (twin y-axis). Each point represents an individual LAE from our fiducial best-fit model, with color coding by their number counts. The left and right panels display results for redshifts $z \sim 2$ and $z \sim 3$, respectively. Only galaxies exceeding a luminosity threshold of $\log(L_{\text{Ly}\alpha}/\text{erg s}^{-1}) > 41.7$ are included.

escape fraction? Fig. 15 shows the relation between stellar mass and SFR. Our LAEs tend to be in an upper region of the star formation main sequence, and the number of LAEs generally decreases as a function of M_* (see also Fig. 12). This is expected because, at fixed M_* , galaxies with higher SFR have larger intrinsic Ly α luminosity and V_{exp} and thus larger $f_{\text{esc}}^{\text{ISM}}$. Interestingly, the UniverseMachine model predicts a clear bimodal population in (M_*, SFR) , and our model has no LAE in the quenched population of galaxies. This is not because the intrinsic SFR is too small, but because the escape fraction is too small at high M_* , since galaxies with similar SFR ($\text{SFR} < 10 M_{\odot}/\text{yr}$) are considered LAEs at $\log_{10}(M_*/M_{\odot}) < 9$.

In addition, Fig. 16 shows the ratio of Ly α to UV escape fractions, $f_{\text{esc,Ly}\alpha}^{\text{obs}}/f_{\text{esc,UV}}^{\text{obs}}$, as a function of the neutral hydrogen column density, N_{HI} , for individual LAEs in our model at $z \sim 2$ (left) and $z \sim 3$ (right). The ratio of the Ly α and the UV escape fraction is an indicator of the efficiency with which Ly α photons can escape compared to UV photons due to radiative transfer effects. In our model, this ratio can be expressed as follows:

$$\begin{aligned} \frac{f_{\text{esc,Ly}\alpha}^{\text{obs}}}{f_{\text{esc,UV}}^{\text{obs}}} &\equiv \left(\frac{L_{\text{Ly}\alpha}^{\text{obs}}}{L_{\text{Ly}\alpha}^{\text{int}}} \right) \left(\frac{L_{\lambda, \text{UV}}^{\text{int}}}{L_{\lambda, \text{UV}}^{\text{obs}}} \right) = \frac{f_{\text{esc,Ly}\alpha}^{\text{obs}}}{e^{-\tau_{\text{UV}}}} \\ &= \left(\frac{3 \times 1.4 \times 10^{40} \text{ erg s}^{-1} \text{ \AA}^{-1} \times \text{SFR}_{\text{obs}}}{1 \times 10^{42} \text{ erg s}^{-1} \times \text{SFR}_{\text{obs}}} \right) \left(\frac{\lambda_{\text{Ly}\alpha}}{\lambda_{\text{UV}}} \right)^{-2} \text{EW}_0 = \frac{\text{EW}_0}{47 \text{ \AA}}. \end{aligned} \quad (22)$$

where the observed Ly α escape fraction, $f_{\text{esc,Ly}\alpha}^{\text{obs}}$, was introduced in Sec. 3.1, and the observed UV escape fraction, $f_{\text{esc,UV}}^{\text{obs}} = e^{-\tau_{\text{UV}}}$, was computed in Sec. 2.2. The second line of Eq. (22) is derived with the Kennicutt relations we adopted for intrinsic Ly α luminosity and UV continuum luminosity density (Kennicutt 1998). In Fig. 16, we find a strong anti-correlation between $f_{\text{esc,Ly}\alpha}^{\text{obs}}/f_{\text{esc,UV}}^{\text{obs}}$ and N_{HI} , indicating that denser hydrogen environments significantly suppress Ly α escape compared to the UV continuum. This is expected, since higher N_{HI} gives smaller observed Ly α escape fraction, $f_{\text{esc,Ly}\alpha}^{\text{obs}}$ as seen in Fig. 2. At column

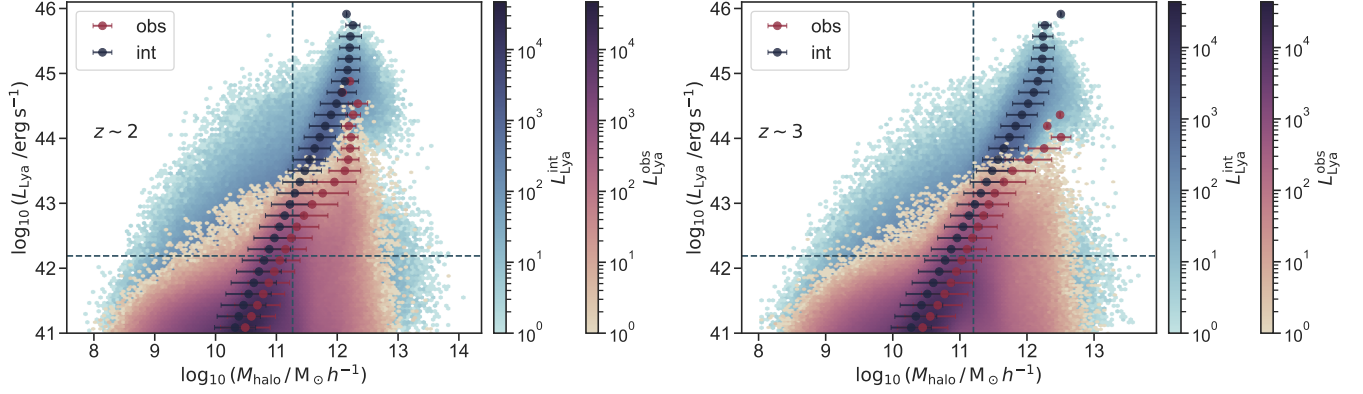


FIG. 17.— $\text{Ly}\alpha$ intrinsic (blue) and observed (pink) luminosities as a function of halo mass. The left panel presents our fiducial model results at $z \sim 2$, and the right panel shows the corresponding results at $z \sim 3$. The vertical dashed line marks the mean halo mass of the observed LAE sample, while the horizontal dashed line indicates the minimum luminosity threshold adopted for the angular correlation function analysis.

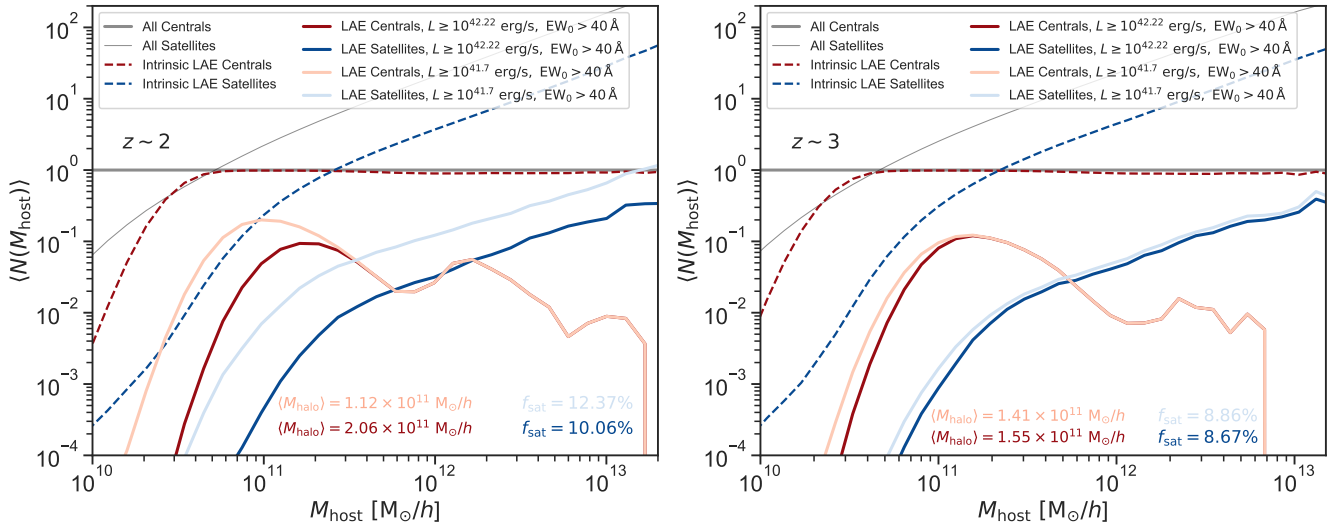


FIG. 18.— Halo Occupation Distribution (HOD) of LAEs at $z \sim 2$ (left) and $z \sim 3$ (right). Gray curves show the total central and satellite galaxy occupation functions in *UniverseMachine*. Dashed red and blue lines represent intrinsic LAE central and satellite populations selected based solely on SFR (see Eq. 2). Solid red and blue lines show the final observed LAE populations after accounting for ISM and IGM radiative transfer effects for two $\text{Ly}\alpha$ luminosity thresholds. Mean halo masses and satellite fractions are quoted for each sample.

densities $N_{\text{HI}} \lesssim 10^{19} \text{ cm}^{-2}$, $\text{Ly}\alpha$ photons escape almost as efficiently as UV continuum photons ($f_{\text{esc,Ly}\alpha}^{\text{obs}}/f_{\text{esc,UV}}^{\text{obs}} \approx 1$). Note also that the ratio can exceed unity, that is, $f_{\text{esc,Ly}\alpha}^{\text{obs}} > e^{-\tau_{\text{UV}}}$. As expected from Eq. (22), the ratio is defined in terms of the luminosity density for UV but the luminosity for $\text{Ly}\alpha$, leading to the dependence of $f_{\text{esc,Ly}\alpha}^{\text{obs}}/f_{\text{esc,UV}}^{\text{obs}} \propto \text{EW}_0$ and the ratio is greater than unity for LAEs with $\text{EW}_0 > 47 \text{ \AA}$. $f_{\text{esc,Ly}\alpha}^{\text{obs}}/f_{\text{esc,UV}}^{\text{obs}} \gg 1$ has been invoked in the past to theoretically explain objects with unusually large $\text{Ly}\alpha$ EWs (Neufeld 1990; Hansen & Oh 2006; Gronke & Dijkstra 2014). In reality, this would be possible in geometries in which the HI can ‘shield’ the dust from $\text{Ly}\alpha$ radiation. Such configurations require optically thick clumps embedded in a low-dust medium Duval et al. (2014). However, more recently it has been argued that these conditions are not realistic and such ‘equivalent width boosting’ are quiet rare and unlikely to be common in realistic galaxies (Laursen et al. 2013; Gronke et al. 2017). It is reassuring that our modeling approach, relying on physically motivated but less extreme assumptions, does not require ratios significantly greater than unity at $z \sim 2-3$. We also notice that some of our LAEs have a small ratio, $f_{\text{esc,Ly}\alpha}^{\text{obs}}/f_{\text{esc,UV}}^{\text{obs}} < 0.1$, particularly for LAEs with high HI column density. These systems could be regarded as Damped Lyman- α Absorbers (DLAs) with $\log_{10}(N_{\text{HI}}/\text{cm}^{-2}) \gtrsim 20.3$, which is consistent with a scenario where DLAs are hosted by massive halos (e.g., Bird et al. 2014).

4.3.2. LAE-halo Connection

Understanding how observed galaxies are connected with underlying dark-matter halos is important for both cosmology and galaxy evolution studies. This is because the clustering amplitude and its scale dependence on scales greater than the typical virial radius of halos depend on characteristic quantities of dark-matter halos, such as halo mass and age (see e.g., Wechsler & Tinker 2018, for a review). In addition, the clustering on the scales smaller than the halo virial radius tells us how the evolution of galaxies are affected by the dense environment. Some earlier observational work interpreted the large-scale amplitude of the LAE

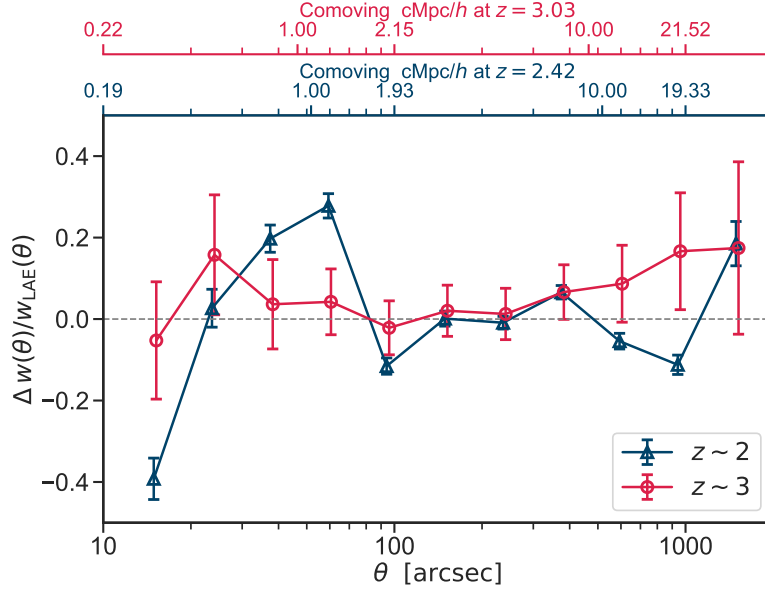


FIG. 19.— The measured strength of the assembly bias effect in our LAE model. Fractional difference between the angular correlation function of shuffled *UniverseMachine* galaxies and observed LAEs at $z \sim 3$ (red circles) and $z \sim 2$ (blue triangles). Shuffling preserves the mass-dependent halo occupation distribution but removes dependencies on secondary halo properties.

angular correlation function on the basis of a simple framework such as the correlation length or Halo Occupation Distribution (HOD), concluding that LAEs typically occupy halos with masses ranging from $\approx 10^{11}$ - $10^{12} M_{\odot}$ (e.g., [Hamana et al. 2004](#); [Ouchi et al. 2018](#); [Hong et al. 2019](#); [Herrero Alonso et al. 2021](#)). However, it is particularly unclear if such a simple framework works well for LAEs as HOD is supposed to work for a mass-limited galaxy sample, which is not clearly the case for LAEs. We remind here that our LAE model is designed to reproduce the luminosity function and the large-scale angular correlation function and thus *predicts* the LAE-halo connection as a consequence.

In Fig. 17, we show the LAE distribution of the Ly α luminosity versus the dark matter halo mass. We show intrinsic (blue) and observed (pink) Ly α luminosities as a function of the halo mass. Since the halo mass is the same for an intrinsic and observed luminosity for each LAE, blue points moved vertically downwards from the corresponding pink points. The blue and red error bars indicate the mean and standard deviation of the halo mass within each intrinsic and observed luminosity bin, respectively. At both $z \sim 2$ (left) and $z \sim 3$ (right), there is a clear trend of increasing luminosity with increasing halo mass, indicating that more massive halos typically host brighter LAEs. However, the halo mass scatter at fixed Ly α luminosity is as large as 0.5 dex, contributed by two effects; about 0.3 dex from the intrinsic scatter between SFR and halo mass as well as about 0.4 dex from the additional scatter from the Ly α RT model. This fact is qualitatively consistent with a little evolution of the LAE bias as a function of Ly α luminosity in [Kusakabe et al. \(2018\)](#).

We also compute the HOD of our simulated LAEs. Fig. 18 presents the resulting HODs at $z \sim 2$ (left) and $z \sim 3$ (right). The solid gray lines show the mean occupation of all central and satellite galaxies in the *UniverseMachine* sample, while dashed lines represent the intrinsic LAEs (galaxies that satisfy our SFR-based LAE selection before accounting for Ly α radiative transfer effects with $\text{SFR} \geq 0.1 M_{\odot} \text{ yr}^{-1}$). These curves serve as a reference to isolate the impact of radiative transfer and selection criteria. The solid red and blue curves show the observed LAE populations, split into central and satellite components for different Ly α luminosity thresholds. We find that the HOD of the observed LAE centrals generally follows the shape of the intrinsic LAE sample, but exhibits a suppression at high halo masses due to the lower Ly α escape fraction, as discussed earlier. The LAE occupation peaks around the halo masses of $10^{11} - 10^{12} M_{\odot}$ and declines toward higher halo masses, in qualitative agreement with other earlier work (e.g., [Ravi et al. 2024](#); [Sullivan et al. 2025](#)). We also quote the mean halo mass and satellite for each Ly α luminosity threshold in Fig. 18 and Table. 1. Since we do not force our model to match the angular correlation function in the one-halo regime, the 8.7-12.4% satellite fraction is merely a prediction. In addition, we find that, out of these LAE satellites, about 25% of them are hosted by LAE centrals, and the rest of about 75% are hosted by other centrals.

Finally, we quantify the impact of the halo assembly bias in our LAE model. The halo assembly bias refers to the fact that the clustering properties of galaxies/halos depend on secondary halo characteristics beyond halo mass alone (see e.g., [Wechsler et al. 2006](#); [Gao & White 2007](#); [Zehavi et al. 2018](#); [Artale et al. 2018](#)). To isolate the impact of occupancy variations in our LAE population, we performed a shuffling test, following [Hearin et al. \(2016\)](#). Within each halo mass bin, we randomly select *UniverseMachine* galaxies to match the exact number of LAEs, computing the angular correlation function, $w(\theta)$, for each randomized realization. Fig. 19 shows the fractional difference between the shuffled and observed LAE angular correlation functions ($\Delta w(\theta)/w_{\text{LAE}}(\theta)$) at both redshifts. The deviations from zero would indicate the presence of assembly bias, but in our test the residuals hover around zero at all scales and at both redshifts therefore there is no systematic deviation beyond the $1-\sigma$

TABLE 2.— A comparison with other example LAE simulation works at $z \sim 2-3$. “✓” symbol means the model is fitted to or compared at the level of χ^2 with the corresponding observable. “✓_{cc}” symbol means the model prediction is just compared with the corresponding observable as a consistency check. If a comparison with observational data is not available, it is indicated by “–”. LF/\bar{n}_g stands for the luminosity function or the integrated number density of LAEs, while $w(\theta)/b_g$ stands for the angular correlation function or just the clustering amplitude in terms of the LAE galaxy bias. The last column “Misc.” refers to miscellaneous observables related to LAEs.

Reference	L_{box} cMpc/h	Galaxy model	Ly α RT model	LF/\bar{n}_g	$w(\theta)/b_g$	Misc.
This work	400	empirical (UniverseMachine)	spherical shell RT & mean IGM transmission	✓/✓	✓/✓	✓ _{cc}
Byrohl & Nelson (2023)	35	hydro (TNG)	full RT	✓/✓	–	✓ _{cc}
Nagamine et al. (2010)	10–100	hydro (GADGET2)	constant/empirical f_{esc}	✓/✓	–	–
Shimizu et al. (2011)	100	hydro (GADGET2)	empirical f_{esc}	✓/✓	✓ _{cc} /✓ _{cc}	✓ _{cc}
Im et al. (2024)	$90 \times 90 \times 1000$	hydro (Horizon Run 5)	empirical f_{esc}	✓/✓	–	✓ _{cc}
Ravi et al. (2024) Sullivan et al. (2025)	500/250	hydro (MTNG/Astrid)	empirical f_{esc}	–/✓	✓ _{cc} /✓	–
Garel et al. (2015)	100	semi analytic (GALICS)	spherical shell RT & no IGM transmission	✓/✓	–	✓ _{cc}
Gurung-López et al. (2019b)	542	semi analytic (GALFORM)	spherical shell RT & IGM transmission	✓/✓	✓ _{cc} /✓ _{cc}	–

uncertainties. Thus, the level of assembly bias is statistically insignificant in our limited size of the simulation box (400 cMpc/h) and a more solid conclusion would require a bigger simulation.

5. DISCUSSION

5.1. Comparison with previous works

We now outline the differences and complementarities among various LAE simulation works in the literature. In Table 2, we try to provide a brief summary of the comparison among different cosmological simulations of LAEs, focusing on the relevant redshift range, $z = 2-3$.

The most physically well-motivated approach would be to run a cosmological hydrodynamical simulation and a Ly α RT code on the fly or as a post process. However, neither is it computationally feasible to resolve the dynamic range of relevant spatial scales, nor can such approach explore the large space of unconstrained physical parameters. As a result, most of the LAE models based on hydro simulations still relied on empirical modeling of the Ly α escape fraction (Nagamine et al. 2010; Shimizu & Umemura 2010; Shimizu et al. 2011; Im et al. 2024; Ravi et al. 2024; Sullivan et al. 2025). The only exception is the work of Byrohl & Nelson (2023) where they adopted the high-resolution TNG50 simulation and ran a full Monte Carlo Ly α RT calculation on the Voronoi mesh. Still, their simulation volume was limited only to 35 cMpc/h, and they needed to calibrate their dust attenuation by rescaling the Ly α emission from stellar regions to match the observed Ly α luminosity function $z \sim 2$. They have also checked that their LAE model is consistent with other observables such as the Ly α escape fraction versus stellar mass and the EW distribution, but do not consider spatial LAE clustering.

Semi-analytic or empirical models such as UniverseMachine would be less physical but more flexible than a hydro approach to model the entire galaxy population in a cosmological volume. Although earlier work in this category adopted an empirical model of the Ly α escape fraction (Le Delliou et al. 2006; Kobayashi & Totani 2008), more recent work included Ly α RT in a more physically well-motivated way using the spherically expanding shell model (Garel et al. 2015; Gurung-López et al. 2019a). Our work could be categorized here.

Since none of the work predicts the relevant LAE observables from the first principle, it would be important to know the observables against which each model is calibrated. Our work is unique in the sense that it is the only model that simultaneously reproduces the LAE luminosity function and the angular correlation function with the Ly α RT model being included beyond a simple empirical escape fraction model.

5.2. Limitations of our model and future directions

Our framework leaves room for a number of future improvements. First, the spherical shell Ly α RT model is currently a simplified and effective model, and it does not capture the real complexities of individual systems of gas density and velocity distribution. Although the spherical shell model can successfully explain a large number of observed LAE spectra (e.g., Gronke 2017; Gurung-López et al. 2021; Gurung-López et al. 2025; Nianias et al. 2025) and can be mapped onto different, more complex geometries (Gronke & Dijkstra 2016; Li & Gronke 2022), a single gas shell with fixed outflow velocity cannot explain both the spectral and surface brightness profile at the same time (Song et al. 2020). This means that our model is currently not suitable

for simultaneously studying the impact of Ly α RT on spatial diffusion, e.g., Ly α halos (e.g., Steidel et al. 2011; Momose et al. 2014, 2016; Leclercq et al. 2017; Lujan Niemeyer et al. 2022) or Lyman- α intensity mapping (e.g., Schaap & White 2021; Croft et al. 2018; Lin et al. 2022; Lujan Niemeyer et al. 2023; Lujan Niemeyer 2025). Second, the IGM transmission is treated as just an average at each redshift rather than computing the transmission for each galaxy along its particular line of sight. This means that we may need to be careful when we compare the clustering in three dimensions, since IGM transmission could be correlated with the underlying large-scale structure that leads to an anisotropic selection effect (Zheng et al. 2010; Behrens et al. 2018; Gurung-López et al. 2019b). Third, Lyman- α powering mechanisms other than nebular emission in star-forming regions could be substantial, depending on scales (e.g., Byrohl & Nelson 2023). Most importantly for cosmological applications, AGNs contribute significantly to the high end of the LAE luminosity function (Zheng et al. 2016; Spinoso et al. 2020; Zhang et al. 2021; Liu et al. 2022a,b; Torralba-Torregrosa et al. 2023a). Contamination from (obscured) AGN systems needs to be treated as an additional emission channel and radiative transfer treatment. Finally, the volume of our simulation (side length of 400 cMpc/h) is relatively small by cosmological standards. This imposes restrictions on the applicability of our current mock to cosmological studies with large-scale clustering such as BAO and RSD.

In the future, this work can be expanded in promising directions to further enhance its fidelity and predictive capabilities. We can explore the selection effects by modeling the wavelength-dependent line-of-sight IGM transmission for the given large-scale density and velocity field of the underlying dark matter simulation. IGM transmission features near the halo scale, not captured in the N -body simulations, can be informed by high-resolution cosmological hydrodynamical simulations (Byrohl & Gronke 2020; Byrohl & Nelson 2025) or explore approximate semi-analytical descriptions (e.g., Li & Zheng, in preparation). Hence, we can compute the observed flux by convolving our LAE spectra with such direction-dependent line-of-sight IGM transmission, incorporating any large-scale correlations affecting the LAE clustering. In addition, we plan to scale up our LAE catalog by adopting a larger simulation such as Uchuu-UM (Aung et al. 2023). Addressing these limitations will open up other exciting scientific investigations. For example, a simultaneous fit of our model to the LAE luminosity function and clustering in a much wider redshift range would allow us to constrain the HI properties on IGM scales during reionization in a manner consistent with low redshifts (e.g., Mason et al. 2015; Umeda et al. 2025). In addition, it is critical to explore in more detail what physical relations are key to reproduce the LAE luminosity function, clustering, and other LAE-related observables. We showed that the simple and empirical scaling relations with the expanding shell model do an excellent job of reproducing these observables with few parameter choices. In our future work, we will explore more systematically how the model is sensitive to the choice of our model assumptions and the implications of the posterior distributions of the model parameters on the observables such as spectral shapes. Such a systematic study would help us refine subgrid physics in a more physical approach, such as a hydrodynamical simulation with a full Ly α RT code.

6. SUMMARY AND CONCLUSION

We have introduced an empirical, yet physically motivated, approach to simulating realistic LAEs at redshifts $z \sim 2-3$ designed for ongoing and forthcoming large-scale cosmological surveys. Our method integrates the UniverseMachine galaxy-halo model, with spherical expanding shell model for the Ly α radiative transfer capturing essential processes in both the ISM and IGM. By calibrating three free parameters, a single set of their values successfully reproduced several observational diagnostics simultaneously, including the UV luminosity function (Fig. 1), observed Ly α luminosity function (Fig. 8), angular clustering (Fig. 9), Ly α equivalent width distribution (Fig. 10), observed Ly α escape fraction (Fig. 12), systemic velocity offsets (Fig. 13) and dust reddening (Fig. 14) at both redshifts. Beyond matching these key diagnostics, our approach also delivers predictions for LAE-halo connection, relation between Ly α luminosity and the halo mass and the relative escape efficiency of Ly α photons compared to the UV continuum.

Below, we summarize the main steps of our implementation and highlight the key findings.

- We started with SMDPL cosmological N -body simulation combined with the UniverseMachine empirical galaxy-halo model which provides a realistic population of galaxies including their positions, velocities, stellar masses and intrinsic star formation rates. The simulation’s moderately large volume (400 cMpc/h) and high resolution (dark matter particle mass of $m_p = 9.63 \times 10^7 M_\odot/h$) allowed us to resolve halos hosting LAEs, while UniverseMachine empirically linked these halos to realistic galaxies with observable properties (Sec. 2).
- The original UniverseMachine predicted SFRs underestimates the faint end of the observed UV luminosity function at $z \sim 2-3$. We adjusted the SFRs to match the faint-end UV luminosity function (while staying consistent with observational uncertainties) to ensure sufficient UV photons for Ly α production. To match the bright end, which can be explained by the attenuation of UV photons by dust, we adopt the empirical approach in Vogelsberger et al. (2020) (Sec. 2.2).
- Using the recalibrated SFR, we computed the intrinsic Ly α luminosity for each galaxy assuming case-B recombination and a Salpeter IMF. This step connects the SFR to the Ly α emission, but the observed Ly α luminosity depends significantly on radiative transfer effects which we modeled next (Sec. 3).
- We simulated how Ly α photons escape galaxies by modeling RT through expanding spherical gas shells using Gurung-López et al. (2021). The escape fraction depends on three key parameters: outflow velocity, neutral hydrogen column

density and dust optical depth. We used UniverseMachine empirical model alongside observationally motivated scaling relations to determine the key radiative transfer properties (Sec. 3.2).

- After escaping the ISM/CGM, Ly α photons face further absorption by the IGM. We adopted a redshift dependent mean transmission curve (based on Laursen et al. (2011)). We modified only the blue side so that it matches the mean IGM transmission from Faucher-Giguère et al. (2008) (Sec. 3.4).
- Combining ISM/CGM and IGM effects, we produced observed Ly α spectra for each LAE. The final observed escape fraction determined whether a galaxy was detected as an LAE. The same intrinsic Ly α luminosity could yield dramatically different observed Ly α luminosities due to RT effects, explaining the scatter in the $L_{\text{Ly}\alpha} - M_{\text{halo}}$ relation (Fig 17).
- We calibrated three free parameters (α, β, γ), scaling V_{exp} , N_{HI} and τ_a , to simultaneously match the Ly α luminosity function and the angular correlation function. A single parameter-set sufficed at both $z \sim 2$ and $z \sim 3$, validating model’s robustness (Sec. 3.5).
- Without further tuning, the model is in agreement with equivalent width distribution, observed Ly α escape fraction, dust reddening and the Ly α velocity offset (Sec. 4.2).
- Beyond matching observational data, our simulation offers insights into the underlying galaxy-halo connection for LAEs. Specifically, we found that LAEs predominantly occupy halos within the mass range of approximately $\sim 10^{10} - 10^{13} M_{\odot}/h$. Our halo-occupation analysis (Fig. 18) shows that the central occupation of observed LAEs closely follows the intrinsic LAE sample at low to intermediate halo masses but shows a pronounced suppression at the high-mass end due to declining Ly α escape fractions. Our satellite fraction prediction changes from 8.7% to 12.4% for our different LAE samples at different redshifts. The central LAE occupation peaks around $10^{11} - 10^{12} M_{\odot}$ before falling off towards larger halo masses reflecting the combined effects of the dust attenuation and metallicity. We demonstrate that lower-mass halos typically lack sufficient Ly α luminosity or escape fraction to be detectable, whereas higher-mass halos may suppress observable Ly α emission due to enhanced metallicity or dust (Sec. 4.3).
- We also examined the potential impact of assembly bias but found their influence to be minor, suggesting that halo mass remains primary driver of LAE clustering. Nevertheless, detecting subtler effects from assembly bias might require future studies with larger samples. Our model also provides predictions for the relationship between Ly α luminosity and halo mass, further demonstrating its versatility (Fig. 19).
- Moreover, we predict the ratio of Ly α to UV escape fractions as an indicator of how efficiently Ly α photons escape relative to the UV continuum. We find a strong anti-correlation of this ratio with the neutral hydrogen column density, indicating that denser hydrogen environments more severely suppress Ly α escape compared to UV photons. (Fig. 16)

Our work bridges the gap between galaxy-scale physics and cosmological surveys by demonstrating that Ly α visibility is not just about star formation. It is a complex interplay of gas dynamics, dust and IGM absorption. The success of our model lies in its simplicity: with only three physically interpretable parameters, we reproduce a wide range of observables. This makes the mock catalog particularly valuable for ongoing and upcoming cosmological LAE surveys, where systematic uncertainties in LAE selection could bias cosmological measurements. We make our LAE catalog and spectra publicly available upon publication.

In the future, we will incorporate additional physical processes and observational constraints to further improve the fidelity of our LAE model. Importantly for precision cosmology, our framework will enable us to explore LAE selection and distortion effects due to the complex radiative transfer across spatial scales. Nevertheless, our framework offers a crucial first step in linking dark-matter halos to LAE observables, turning the LAEs from cosmological nuisances into powerful probes of both galaxy evolution and the large-scale structure.

ACKNOWLEDGMENTS

The authors are grateful to the HETDEX collaboration for their helpful comments. The authors thank Siddhartha Gurung-López for the development of this work in the early stages. HK and SS acknowledge the support for this work from by National Science Foundation grant, NSF-2219212. SS is also supported by the U.S. Department of Energy, Office of Science, Office of High Energy Physics under DE-SC0024694. SS is supported in part by World Premier International Research Center Initiative, MEXT, Japan. Part of this work was carried out by CB as JSPS International Research Fellow. MG thanks the Max Planck Society for support through the Max Planck Research Group, and the European Union for support through ERC-2024-STG 101165038 (ReMMU). This work was performed in part at the Aspen Center for Physics, which is supported by a National Science Foundation grant, PHY-2210452.

The CosmoSim database used in this paper is a service by the Leibniz-Institute for Astrophysics Potsdam (AIP). The MultiDark database was developed in cooperation with the Spanish MultiDark Consolider Project CSD2009-00064. The authors gratefully acknowledge the Gauss Centre for Supercomputing e.V. (www.gauss-centre.eu) and the Partnership for Advanced Supercomputing

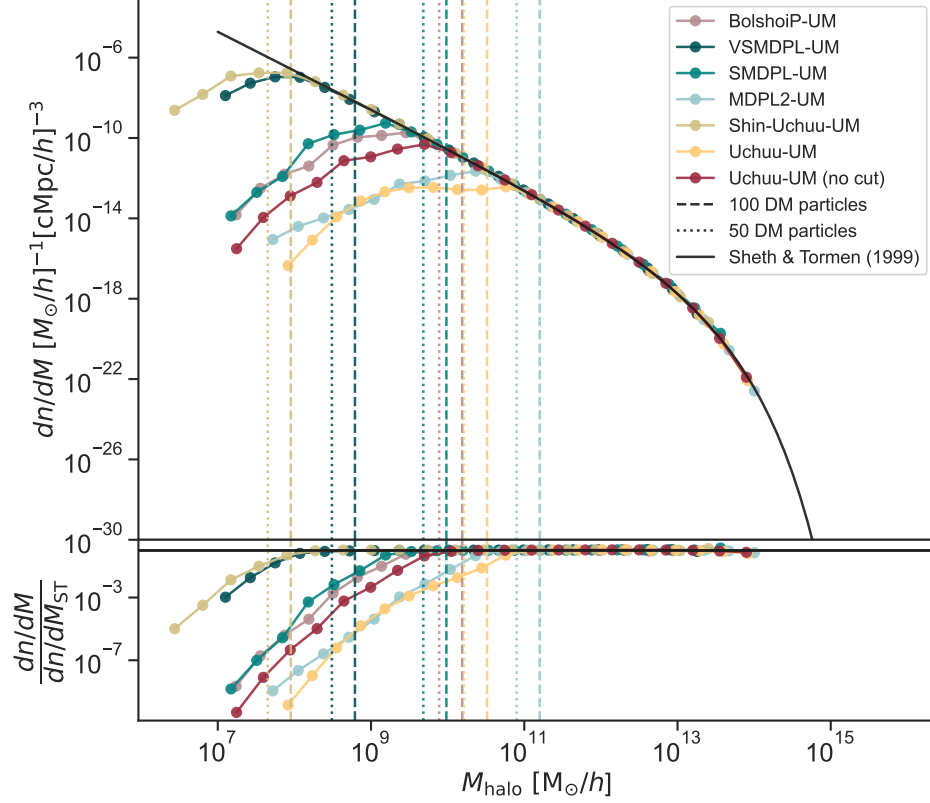


FIG. 20.— Halo mass function comparison for BolshoiP1-UM (Bolshoi series), MDPL2-UM, SMDPL-UM, and VSMPL-UM (MultiDark Planck series), and Uchuu-UM and Shin-Uchuu-UM (Uchuu series). The solid black curve denotes the Sheth & Tormen (1999) halo mass function. Dashed vertical lines indicate the mass corresponding to 100 dark matter particles for each catalog, and dotted vertical lines show the mass of 50 particles (both color-coded with the same color used for the catalog). The lower panel presents the ratio of each simulation’s mass function to the Sheth & Tormen (1999) baseline, highlighting how resolution affects halo abundance in different N -body runs. The yellow curve is the publicly available Uchuu-UM catalog which include a cut of $M_* > 10^8 M_\odot$.

in Europe (PRACE, www.prace-ri.eu) for funding the MultiDark simulation project by providing computing time on the GCS Supercomputer SuperMUC at Leibniz Supercomputing Centre (LRZ, www.lrz.de).

APPENDIX

A. SIMULATION METHODOLOGY AND TECHNICAL DETAILS

In this appendix, we present additional details and tests to support the numerical setup used in our LAE modeling framework. First in Appendix A.1, we assess how varying the mass resolution in different N -body simulations affects the resulting halo mass function. From this analysis, we identify the mass limit below which the halos become unreliable. Next, Appendix A.2 examines how the UV luminosity function evolves with redshift in our recalibrated UniverseMachine catalog, showing that our model remains consistent within the redshift range $1.9 \leq z \leq 3.2$. Finally, Appendix A.3 discusses orphan galaxies, which are indeed subhalos that are no longer tracked by the halo finder. We quantify how these orphans influence LAE observables, particularly their impact on the faint-end of the luminosity function and small-scale clustering.

A.1. The impact of N -body simulation mass resolution

In Sec. 2, we adopt the SMDPL simulation as our baseline for building a realistic LAE catalog. A crucial motivation behind this choice is the simulation’s mass resolution. This is because when halos are composed of too few particles, their star formation rates become poorly determined, and in extreme cases, low-mass halos could disappear entirely even though they can host faint LAEs. To quantify these resolution limits, we compare some widely used N -body plus UniverseMachine catalogs, each derived from a different simulation with different dark matter particle mass resolution (summarized in Table 3). These include BolshoiP1-UM (Bolshoi series), MDPL2-UM, SMDPL-UM, and VSMPL-UM (MultiDark Planck series), as well as Uchuu-UM and Shin-Uchuu-UM (Uchuu series). Fig. 20 compares their halo mass functions against the analytic Sheth & Tormen (1999) prediction. Vertical lines show the halo masses corresponding to 100 and 50 dark matter particles color-coded for each catalog. In our fiducial SMDPL-UM case, 100 particles correspond to a halo mass of roughly $9 \times 10^9 M_\odot/h$, well below the typical LAE host halo mass $\gtrsim 10^{11} M_\odot$ at $2 \lesssim z \lesssim 3$ (Ouchi et al. 2020) ensuring that we could resolve the halos that matter for our LAE sample.

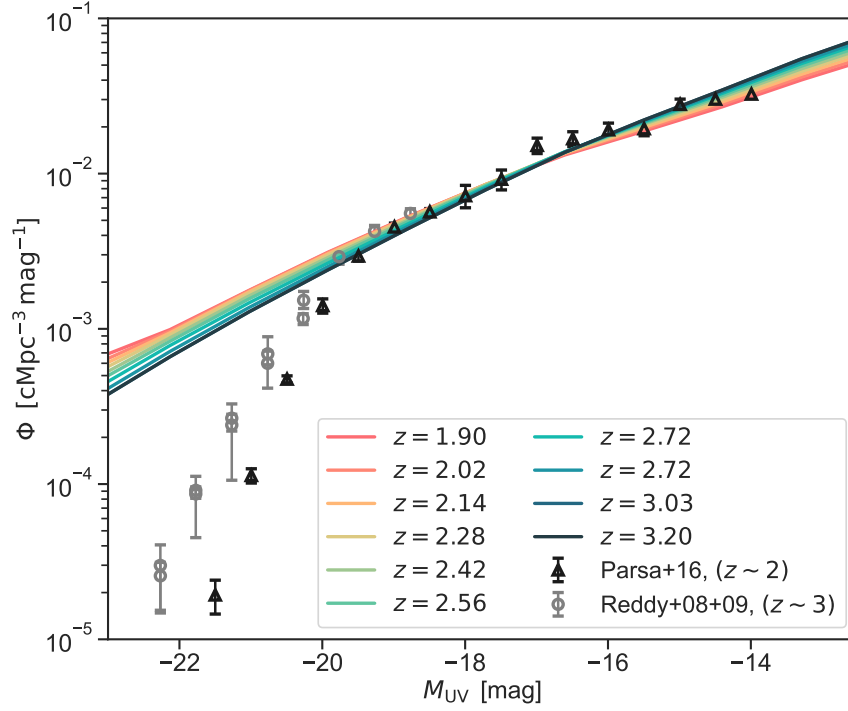


FIG. 21.— Dust-free rest-frame UV luminosity functions predicted by the UniverseMachine model after applying (Eq. 1). Colored curves show 10 snapshots from $z = 1.9$ (red) to $z = 3.2$ (dark blue, see legends for exact redshifts). Black triangles and gray circles are the measurements from Parsa et al. (2016) and Reddy et al. (2008); Reddy & Steidel (2009). The model consistently reproduces the observed faint-end across all redshifts with minimal evolution ($\lesssim 0.1$ dex) confirming that dust parameters calibrated at $z = 2.42$ and $z = 3.03$ suffice for the full $z \sim 2-3$ range.

TABLE 3.— A summary of six distinct Nbody-*UniverseMachine* catalogs, each with its own box size, particle count, and mass resolution. SMDPL-UM, the focus of this work, provides an optimal trade-off between moderate volume (400 cMpc/h) and comparatively high mass resolution ($9.63 \times 10^7 M_\odot/h$), enabling it to sufficiently resolve the halos that typically host LAEs at $z \sim 2-3$.

NBODY-UNIVERSEMACHINE catalogs	Boxsize	Number of particles	Mass Resolution
BOLSHOIP-UM	250 cMpc/h	2048^3	$1.55 \times 10^8 M_\odot/h$
VSM-DPL-UM	160 cMpc/h	3840^3	$6.17 \times 10^6 M_\odot/h$
SMDPL-UM	400 cMpc/h	3840^3	$9.63 \times 10^7 M_\odot/h$
MDPL2-UM	1000 cMpc/h	3840^3	$1.51 \times 10^9 M_\odot/h$
SHIN-UCHUU-UM	140 cMpc/h	6400^3	$8.97 \times 10^5 M_\odot/h$
UCHUU-UM	2000 cMpc/h	12800^3	$3.27 \times 10^8 M_\odot/h$

A.2. Redshift evolution of the model UV luminosity function

After recalibrating the SFR in *UniverseMachine* (Eq. 1 in Sec. 2.2), we confirm our model reproduces the observed UV luminosity function consistently across the redshift range $1.9 \leq z \leq 3.2$. Fig. 21 presents the predicted dust-free UV luminosity functions for 10 snapshots within this redshift interval, compared to observational data from Parsa et al. (2016) at $z \sim 2$ and Reddy et al. (2008); Reddy & Steidel (2009) at $z \sim 3$. It shows the model successfully matches the observed UV luminosity function at magnitudes fainter than $M_{UV} \sim -20$. This agreement, with variation of less than ~ 0.1 dex, holds across the entire redshift range and demonstrate that the weak redshift evolution justifies our calibration strategy: The adjustments made at $z = 2.42$ and $z = 3.03$, sufficiently characterize the galaxy population across $1.9 \leq z \leq 3.2$ without requiring redshift-dependent corrections. While this appendix focuses on the dust-free faint end, we emphasize that the empirical dust model from Vogelsberger et al. (2020) corrects the bright end overprediction in our main analysis.

A.3. Orphan Galaxies and their Impact on LAEs

In the *UniverseMachine* galaxy-halo connection model, “orphan” galaxies represent satellite galaxies whose host subhalos have fallen below resolution limits of the simulation and are no longer tracked by the halo finder. These orphans originate from subhalos in earlier snapshots but lack an associate dark matter structure in the final halo catalog. To evaluate their impact on our model predictions for LAE populations, we compare model outputs constructed with and without orphans at redshifts $z \sim 2$ and $z \sim 3$. We define the orphan fraction as: $f_{\text{orphan}} \equiv N_{\text{orphan}}/N_{\text{LAE}}$, where N_{orphan} is the number of orphan LAEs and N_{LAE} is the total LAE population. At $z = 3.03$, $f_{\text{orphan}} = 0.02$, rising to 0.03 at $z = 2.42$. While subdominant, we systematically quantify

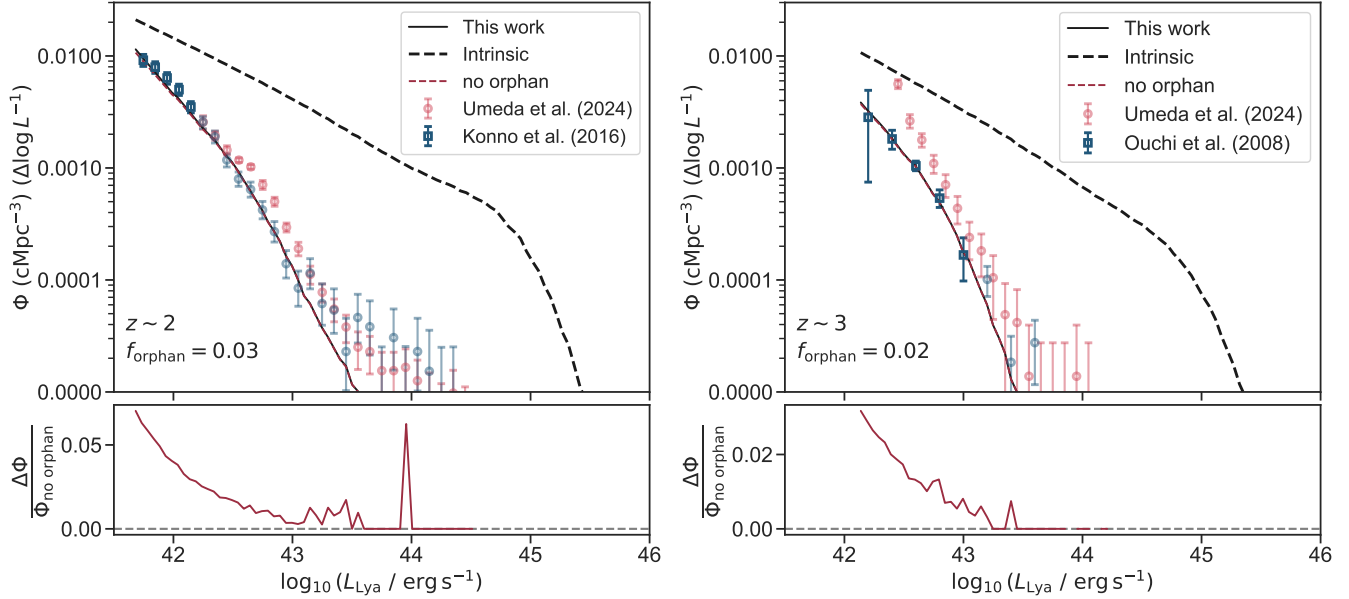


FIG. 22.— Impact of orphan galaxies on the Ly α luminosity function at $z \sim 2$ (left) and $z \sim 3$ (right). Black solid and red dashed curves show LAE samples with and without orphans, respectively. The inclusion of orphans boosts the faint end ($\log_{10}(L_{\text{Ly}\alpha}/\text{erg s}^{-1}) \lesssim 42.5$) by $\sim 5\%$, while leaving the bright end unchanged. Lower panels quantify the relative difference $((\Phi_{\text{w orphan}} - \Phi_{\text{no orphan}})/\Phi_{\text{no orphan}})$, demonstrating how orphan removal suppresses faint LAE counts. This analysis extends the main luminosity function results from Fig. 8 by isolating the specific contribution of orphan galaxies to the LAE population.

their influence to ensure robustness.

To evaluate their impact, we have computed the effects of excluding orphans from our LAE sample on all key diagnostics. For conciseness, we present results only for the Ly α luminosity function (Fig. 22), angular correlation function (Fig. 23) and halo occupation distributions (Fig. 24), while discussing the other diagnostics in the main text of this appendix.

Beginning with the luminosity function, we find the most noticeable orphan effect appear at the faint end. Fig. 22 shows that including orphans produces a modest but systematic enhancement of $\sim 5\%$ at most for galaxies with $\log_{10}(L_{\text{Ly}\alpha}/\text{erg s}^{-1}) \lesssim 42.5$. This boost reflects their contribution as predominantly low-luminosity satellites that would otherwise be absent from the sample. The effect is consistent across both redshifts, though slightly more pronounced at $z \sim 2$ where the orphan fraction is slightly higher ($\sim 3\%$ at $z \sim 2$ vs. $\sim 2\%$ at $z \sim 3$), suggesting a mild redshift dependence in their impact on the faint-end luminosity function.

The orphan population's role as satellites become even more apparent when examining their impact on clustering. Fig. 23 shows that orphans enhance the 1-halo term of the angular correlation function by up to $\sim 10\%$ at small scales ($\theta \lesssim 10''$), while leaving the 2-halo term unchanged. This scale-dependent effect occurs because orphans contribute exclusively to intra-halo pair counts as unresolved satellites, with their $\sim 3\%$ population fraction at $z \sim 2$ translating to a proportionally larger effect on small-scale clustering due to their concentrated spatial distribution within halos. The unchanged 2-halo term confirms that orphans do not affect the large-scale bias of the LAE population, consistent with their nature as subdominant satellite systems.

The scale-dependent clustering patterns in Fig. 23, find their physical explanation in the halo occupation statistics. Fig. 24 illustrates that orphans contribute exclusively to the satellite population, accounting for up to $\sim 20\%$ of satellites in low-mass halos $M_{\text{halo}} \lesssim 10^{11} M_{\odot}/h$. Their concentrated spatial distribution within these halos naturally explains both the enhanced small-scale clustering seen in Fig. 23 and the $\sim 20\%$ increase in satellite fraction when orphans are included (f_{sat} values in blue in Fig. 24). This halo occupation signature simultaneously clarifies why removing orphans reduces the faint-end luminosity function (Fig. 22). The missing satellites preferentially reside in lower-mass halos hosting fainter LAEs. The complete lack of orphan contribution to central galaxies further confirms they represent a distinct population from normal satellites with resolved subhalos, consistent with their origin as numerically unresolved systems.

Beyond the luminosity function and clustering, we assessed how orphan galaxies influence additional LAE observables. Their impact is consistently minor. The relationship between halo mass and Ly α luminosity shifts by less than 0.005 dex. The rest-frame equivalent width distribution, including its exponential slope and high EW tail, shows no statistically significant changes, with differences confined to the $\pm 1\sigma$ uncertainty of the best-fit model. Orphans reduce the Ly α emitter fraction $X_{\text{Ly}\alpha}$ by at most $\sim 5\%$ for the faintest UV magnitudes, though this falls below typical Poisson errors. Similarly, the median Ly α escape fraction $f_{\text{esc,Ly}\alpha}^{\text{obs}}$, shifts by < 0.02 across stellar masses. Kinematic diagnostics like velocity offsets, $\Delta v_{\text{Ly}\alpha}$, vary by less than $\lesssim 0.25 \text{ km s}^{-1}$, while the anti-correlation between Ly α -to-UV escape ratios and N_{HI} remains indistinguishable (shifts $\lesssim 0.01$). The dust reddening

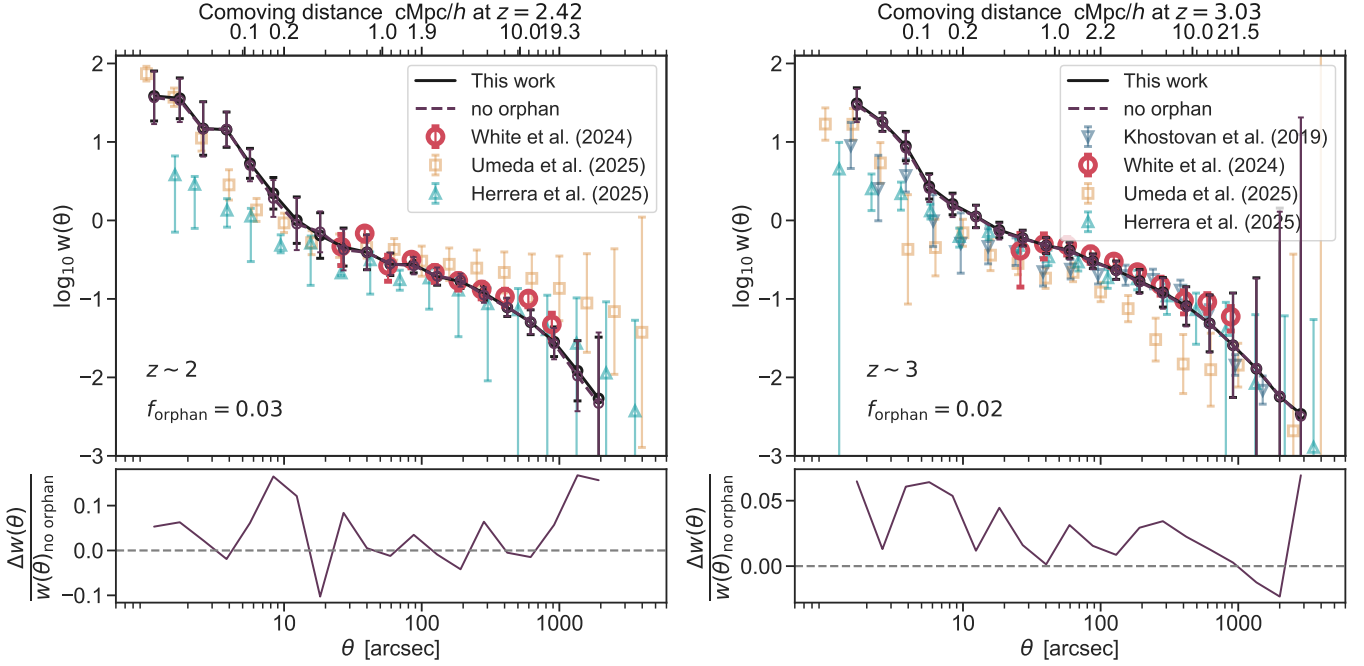


FIG. 23.— Impact of orphan galaxies on LAE clustering at $z \sim 2$ (left) and $z \sim 3$ (right). Black solid and red dashed curves show the angular correlation function, $w(\theta)$, for samples with and without orphans, respectively. Orphans enhance small-scale clustering ($\theta \lesssim 10''$) by up to $\sim 10\%$ by contributing to intra-halo satellite pairs, while leaving large-scale clustering ($\theta \gtrsim 100''$) unaffected. Lower panels quantify the relative difference $((w(\theta)_{\text{w orphan}} - w(\theta)_{\text{no orphan}}) / w(\theta)_{\text{no orphan}})$, confirming their exclusive impact on the 1-halo regime. These results demonstrate how orphan satellites, despite constituting only 2–3% of the LAE population, disproportionately affect small-scale clustering due to their spatial concentration within halos.

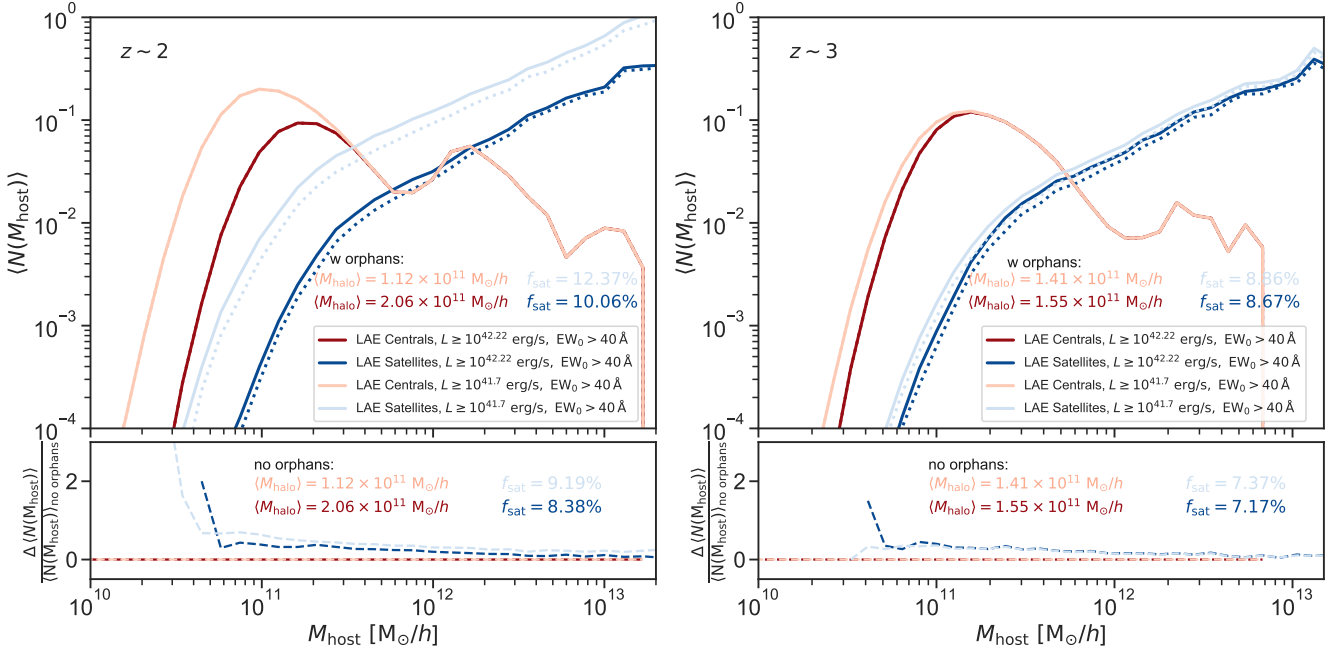


FIG. 24.— Halo Occupation Distribution of LAEs at redshifts $z \sim 2$ (left) and $z \sim 3$ (right), comparing samples with (solid lines) and without (dotted lines) orphan galaxies. Central LAEs are shown in red and satellite LAEs in blue. The darker curves represent LAEs with a luminosity cut of $\log_{10}(L_{\text{Ly}\alpha}/\text{erg s}^{-1}) > 42.22$, while the lighter curves correspond to a fainter cut of $\log_{10}(L_{\text{Ly}\alpha}/\text{erg s}^{-1}) > 41.7$. The lower panels quantify the relative difference in HOD between the two samples, $((N(M_{\text{host}})_{\text{w orphan}} - N(M_{\text{host}})_{\text{no orphan}}) / (N(M_{\text{host}})_{\text{no orphan}}))$, highlighting how excluding orphan galaxies, which are exclusively satellites reduces the satellite occupation by up to $\sim 20\%$, particularly in lower mass halos ($M_{\text{host}} \lesssim 10^{11} M_{\odot}/h$). This removal of orphans leaves the central population of LAEs unchanged also does not affect the mean halo mass of the sample. The results underscore the minor but systematic role of orphans in shaping the satellite fraction and clustering of faint LAEs.

trends are also unaffected, with median $f_{\text{esc, Ly}\alpha}^{\text{obs}}$ vs. $E(B-V)$ varying $\lesssim 0.005$, negligible compared to observational uncertainties. Collectively these tests confirm that orphans, while non-zero in their influence, introduce no systematic biases to the broader LAE population or its inferred physical properties.

B. SCALING RELATIONS - EVIDENCE FROM SIMULATIONS

Our model depends on three crucial scaling relations that link galaxies to their dark matter halos and gas properties. While these relations were initially motivated by observational studies, we demonstrate here that they are also supported by results from hydrodynamical simulations. This appendix shows that our choices for galaxy size, gas content and metallicities, all align well with what cosmological simulations predict. The agreement between observations and simulations suggests that our scaling relations reflect the key physics governing LAEs, particularly at redshifts where direct measurements are challenging.

B.1. Galaxy size-halo size relation

Our model connects stellar half-mass radius, $r_{1/2}$, to their halo virial radius, R_{vir} through a simple but physically motivated two-regime prescription: for larger halos ($R_{\text{vir}} > 113$ pkpc), the stellar half-mass-radius scales linearly with the virial radius as $r_{1/2} \approx 0.015 R_{\text{vir}}$, while for smaller halos, the relation flattens to account for the observed compactness of low-mass galaxies (see Fig. 4, top left panel). This behavior aligns remarkably well with trends seen in cosmological simulations like IllustrisTNG (see Karmakar et al. (2023)), which shows a nearly linear size-halo relation with minimal evolution from $z = 0$ to $z = 3$. We also included a Gaussian scatter of 0.12 dex motivated by observational as well as simulation works. Our choice of slope, pivot and scatter (see sec.3.3) therefore reproduces the size-halo relation for both low- and high-mass halos seen in fully hydrodynamical simulations. As shown in top left panel of Fig. 25, the consequence of our scaling relation is that for low-mass halos, the galaxy-size to halo-size ratio reduces by increasing the halo mass, while at high-halo mass, the ratio remains approximately constant. This relation remains consistent with the results from Karmakar et al. (2023). This agreement between simulations and observations strengthens our choice of this scaling relation.

B.2. Stellar mass-neutral hydrogen mass relation

When modeling how much neutral hydrogen surrounds galaxies, we start with a simple but effective trend. More massive galaxies tend to have proportionally less atomic gas relative to their stars. This matches what we see in local galaxy surveys like XGASS (Catinella et al. 2018). The relation follows a scatter of 0.1 dex as we have discussed in Sec. 3.3. What is particularly useful is that modern simulations like IllustrisTNG (Nelson et al. 2017; Pillepich et al. 2017; Springel et al. 2017; Marinacci et al. 2018; Naiman et al. 2018), SIMBA (Davé et al. 2019) and EAGLE (Schaye et al. 2014; Crain et al. 2015) show this relationship holds remarkably well back to $z \sim 2-3$ (see Fig. 25, top right panel). While gas fractions were higher in the early universe, the fundamental connection between stellar mass and HI mass appears stable over time. This means our scaling relation likely reflects the true gas content of LAEs during their peak epoch, even if direct HI measurements at these redshifts remain challenging. The modest scatter we include accounts for the natural diversity in gas accretion histories while staying grounded in both observational and simulation results.

B.3. Cold gas metallicity - stellar mass relation

For modeling the metal content of LAEs, we start with a simple but powerful trend. More massive galaxies tend to have more enriched gas. We adjusted the local mass-metallicity relation from Tremonti et al. (2004) to better match observations at $z \sim 2-3$ (see Sec. 3.3), lowering the overall normalization while keeping the same slope. This tweak makes physical sense, galaxies at cosmic noon were still building up their metal supplies through ongoing star formation. A key strength of this relation is its consistency across different approaches. While the absolute metallicity values in simulations can vary depending on feedback prescriptions, the fundamental trend we adopt aligns well with results from FIRE simulations (Ma et al. 2016). Our conservative 0.05 dex scatter accounts for the natural variations we see in both observations and simulations, some galaxies form stars more efficiently, while others lose metals more easily through outflows. For LAEs specifically, getting this metallicity right is important, because it directly impacts both dust attenuation and the radiative transfer of Ly α photons through their interstellar medium. (see Fig. 25 for our empirical adjusted relation with simulation predictions at $z \sim 2-3$ (Ma et al. 2016).)

C. CALIBRATION AGAINST DIFFERENT OBSERVATIONAL MEASUREMENTS

To assess how sensitive our model is to observational inputs, we recalibrate it using alternative datasets. In Appendix C.1, we examined the impact of luminosity function measurements by adopting the Ly α LF from Umeda et al. (2025), while maintaining our fiducial clustering calibration (White et al. 2024) at both redshifts. This test highlights how the faint-end slope of the luminosity function (especially at $z \sim 3$, where the discrepancies between Umeda et al. (2025) and Ouchi et al. (2008) measurements are more pronounced) affects our parameter estimates. While the best-fit values shift slightly compared to our fiducial calibration, they remain consistent within uncertainties. In Appendix C.2, we investigate the small-scale clustering regime by fitting to the angular correlation function from Khostovan et al. (2019) while keeping the Ouchi et al. (2008) luminosity function calibration fixed at $z \sim 3$. This analysis provides important constraints on satellite galaxy fraction and the 1-halo term that were less prominent in our fiducial clustering dataset choices. Together these tests offer insights into how different aspects of the observational datasets, to which our model is calibrated, influence our model parameters and predictions.

C.1. Parameter constraints and model fitting with Umeda et al. (2024)

In Sec. 4, we calibrated our model parameters, (α, β, γ) , using the luminosity functions from Konno et al. (2016) at $z \sim 2$ and Ouchi et al. (2008) at $z \sim 3$, finding that a single set of parameters could describe both redshifts within uncertainties. To test the sensitivity of our results to the luminosity function measurements, we now recalibrate the model using Umeda et al. (2025) luminosity function measurements, while keeping our fiducial clustering calibration fixed to White et al. (2024) at both redshifts. At $z \sim 2$, luminosity function measurements from Umeda et al. (2025) are brighter than those from Konno et al. (2016) in the

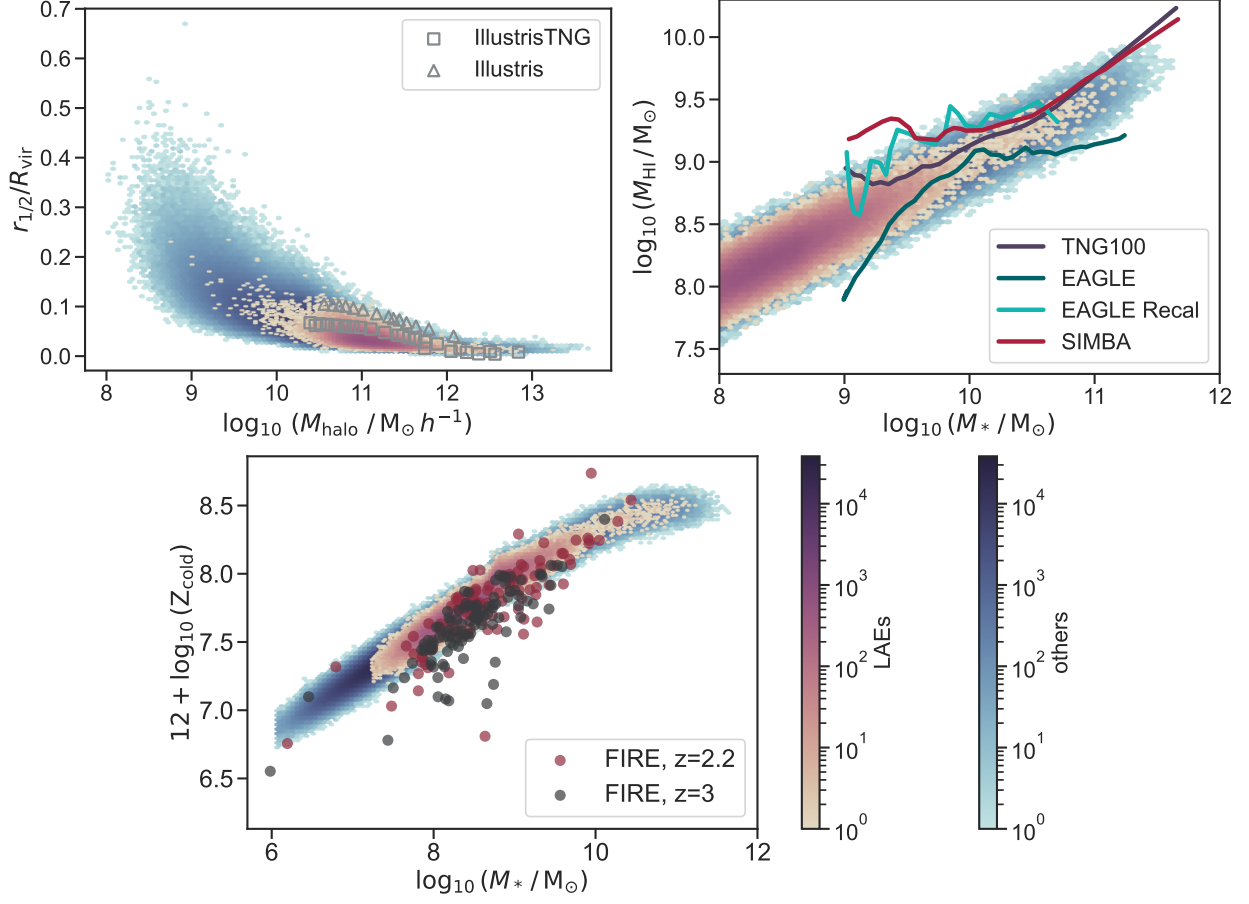


FIG. 25.— Comparison of our adopted scaling relations with hydrodynamical simulation predictions. Same as Fig. 4, the scatter points show our galaxy sample at $z \sim 3$ where LAEs ($\log_{10}(L_{\text{Ly}\alpha} / \text{erg s}^{-1}) \geq 41.7$ and $\text{EW}_0 > 40 \text{ \AA}$) are shown in pink while others are presented in blue. *Top left*: Our galaxy size to halo virial radius ratio versus halo mass compared to Illustris and IllustrisTNG results (Karmakar et al. 2023). *Top right*: Neutral hydrogen mass (M_{HI}), versus stellar mass M_* , showing our empirical relation against simulation predictions. *Bottom*: Gas-phase metallicity, $12 + \log_{10}(Z_{\text{cold}})$, versus stellar mass with our model compared to FIRE simulations (Ma et al. 2016).

faint end, though the two studies yield comparable slopes. At $z \sim 3$, Umeda et al. (2025) luminosity function is steeper than Ouchi et al. (2008) at faint end. The best-fit model for this test is shown in Fig. 26 in solid black line. The bright red data points present the data used for the fit. Our calibration to Umeda et al. (2025), requires adjustments to our free parameters. At $z \sim 2$, $(\alpha, \beta, \gamma) = (2.000^{+0.966}_{-1.000}, 0.080^{+0.020}_{-0.039}, 70.0^{+15.78}_{-10.0})$, while at $z \sim 3$, $(\alpha, \beta, \gamma) = (0.100^{+0.151}_{-0.080}, 0.030^{+0.011}_{-0.030}, 10.0^{+1.222}_{-0.782})$. Unlike our fiducial calibration, these solutions show no overlap between redshifts. The shifts arise because of the following reasons. The steeper luminosity function as $z \sim 3$ demands lower α (weaker outflow) and γ (less dust), while the $z \sim 2$, data require stronger outflow and dust attenuation. Moreover, the sample selection also may probe different LAE populations especially at low luminosities. Also narrow-band filters as well as the cosmic variance could affect the slope of the measurements.

C.2. Angular correlation function fit to Khostovan et al. (2019)

To investigate the model’s adaptability to different clustering constraints, we recalibrated the angular correlation function using the measurements from Khostovan et al. (2019) at $z \sim 3$ (while keeping the luminosity function fixed to Ouchi et al. (2008)). The Khostovan et al. (2019) measurement is based on 1198 LAEs detected over a 1.38 deg^2 field using the NB497 filter, extend to smaller angular scales ($\theta \approx 1''$) than our fiducial dataset (White et al. 2024) and provide valuable constraints on the 1-halo regime. Although their sample has a higher estimated contamination fraction ($\sim 15\%$), the median Ly α luminosity ($\log_{10}(L_{\text{Ly}\alpha} / \text{erg s}^{-1}) = 42.2$) is also higher than in our fiducial sample. Fig. 27 compares the results: the gray curve shows our fiducial model (calibrated to White et al. (2024); red circles), while the black curve shows the model recalibrated to Khostovan et al. (2019) (blue triangles). Recalibrating the parameters successfully reproduces the Khostovan et al. (2019) measurements, primarily by adjusting the satellite fraction to match their higher luminosity threshold, which naturally excludes fainter satellites. This demonstrates the framework’s flexibility to adapt to different observational datasets through parameter adjustments informed by their specific selection functions.

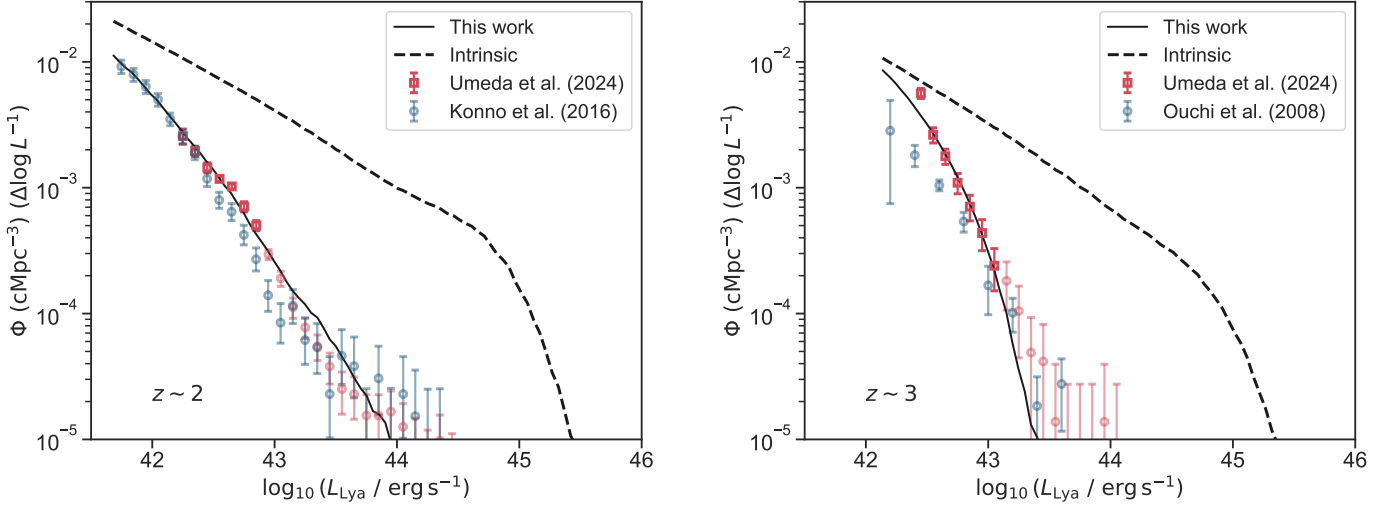


FIG. 26.— Comparison of the $\text{Ly}\alpha$ luminosity function predictions from our model when calibrated to Umeda et al. (2025) (solid line) against the intrinsic luminosity function (dashed line; before radiative transfer effects). The left panel shows results at $z \sim 2$, and the right panel at $z \sim 3$. The black line traces the red square data points (from Umeda et al. (2025)) at both redshifts. For reference we overplot measurements from Konno et al. (2016) at $z \sim 2$ and Ouchi et al. (2008) at $z \sim 3$ in faint blue circles. The fainter red data points are not used in our fitting procedure to avoid contamination from AGNs.

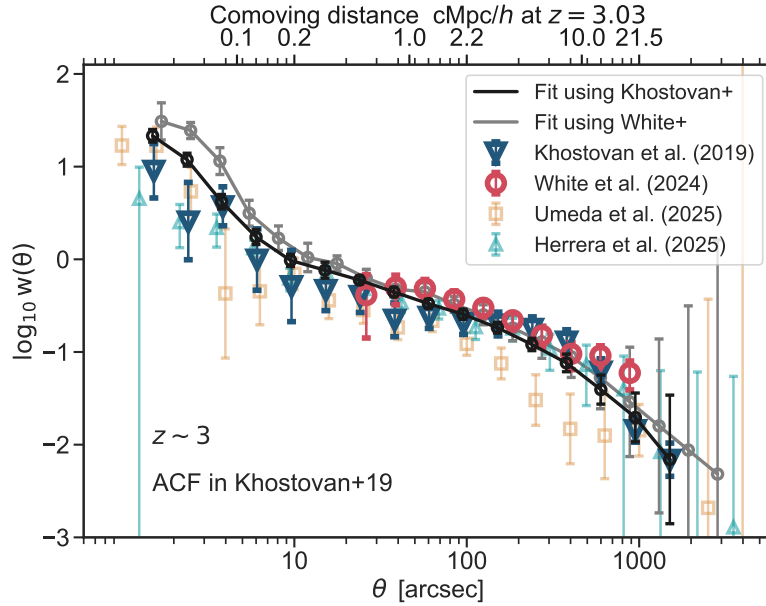


FIG. 27.— Angular correlation function, $w(\theta)$, of LAEs at $z \sim 3$. The gray curve shows our fiducial model calibrated to White et al. (2024), while the black curve shows the model fit to Khostovan et al. (2019). The two curves diverge most strongly at small angular separation, where the 1-halo term dominates. Because the White et al. (2024) measurements do not probe those small scales, the 1-halo contribution in our fiducial model is not well constrained.

D. IMPACT OF FREE PARAMETERS ON $\text{Ly}\alpha$ SUMMARY STATISTICS

In this appendix, we systematically explore how variations in our three free parameters, α (outflow velocity scaling), β (neutral hydrogen column density scaling) and γ (dust attenuation scaling), shape the observable properties of LAEs. These parameters were carefully constrained during our model calibration to reproduce key observational diagnostics: the luminosity function and the angular correlation function. By isolating the influence of each free parameter we gain insights into the physical process governing $\text{Ly}\alpha$ emission and escape, and how these processes shape the observational properties of LAEs. We can directly see which observables are most sensitive to changes in outflow velocity, neutral hydrogen column density and dust optical depth. Appendix D.1 shows the effects on the luminosity function, while Appendix D.2 explores this effect on the angular correlation function. This analysis not only validates the robustness of our model but also highlights the interplay between the parameters and the observables they govern.

D.1. Impact of free parameters on the Luminosity Function

The luminosity function of LAEs serves as a critical diagnostics for understanding how Ly α photons escape from galaxies and propagate through the ISM and IGM. In our model this escape process is governed by three key physical parameters: α , which scales the outflow velocity of neutral hydrogen gas, β , which determines the column density of the neutral hydrogen, and γ , which sets the optical depth of dust attenuation. By systematically varying these parameters while holding others fixed, we can dissect their individual effects on the predicted luminosity function.

Fig 28 demonstrates how each parameter leaves its unique imprint on the Ly α luminosity function. The parameter α , controlling the expansion velocity of gas shells, primarily affect the bright end of the luminosity function. As shown in the left-most panels of Fig 28, increasing α significantly boosts the number density of the most luminous LAEs. This is physically intuitive as galaxies with stronger outflows (higher α), allow more Ly α photons to escape because the Doppler shift from the expanding shell reduces the number of resonant scatterings. At the bright end, where the galaxies typically have higher star formation rates and thus more intrinsic Ly α emission, even small changes in α , lead to noticeable differences in the number of detectable LAEs. When we increase α , we are essentially opening escape routes for photons in the most luminous galaxies, causing the bright end of the luminosity function to rise. In contrast, the faint end of the luminosity function is dominated by low-mass galaxies with smaller V_{exp} . These galaxies are less affected by changes in α because their outflows are weaker (due to the lower sSFR or smaller sizes) so their escape fractions remain low. As α increases, the bright end rises significantly while the faint end stays relatively unchanged, resulting in a flatter overall slope of the luminosity function.

The parameter β , has a broad impact across all luminosities, uniformly suppressing the number of LAEs as it increases. This parameter scales the column density of neutral hydrogen (N_{HI}), which determines how efficiently the ISM/CGM can trap Ly α photons through resonant scattering. Higher β values correspond to denser neutral hydrogen gas, increasing the likelihood of resonant scattering and trapping Ly α photons before they escape. As seen in the middle panels of Fig 28, increasing β shifts the entire luminosity function downward. Unlike α , which selectively affects LAEs with strong outflows (due to the impact from SFR), β 's impact is more uniform because HI mass and size vary less dramatically with luminosity rather than SFR. However a subtle mass dependent may arise. Low-mass LAEs tend to have higher M_{HI}/M_* ratios (Fig. 4, top right), so their N_{HI} , and thus β 's suppression could be slightly more pronounced at the faint end.

The parameter γ , scales the dust optical depth (τ_a), which depends on the product of the cold gas phase metallicity and the HI column density (see Eq. 8). Since dust absorption destroys Ly α photons irrespective of the LAE's intrinsic luminosity or SFR, increasing γ suppresses the Ly α escape fraction across all luminosities. As shown in the right-most panels of Fig 28, increasing γ , results in a nearly parallel downward shift of the entire luminosity function, changing its overall normalization rather than its shape. This uniform suppression occurs because τ_a is tied to dust-to-gas ratio (via Z_{cold}) and N_{HI} , both of which vary less steeply with galaxy mass than outflow velocities or SFR. However subtle deviations may occur. High-mass LAEs tend to have higher metallicities (Fig. 4, bottom panel), so their dust attenuation (and thus γ 's impact) could be slightly more pronounced at bright end.

Our model's effectiveness stems from the distinct yet interconnected roles of α , β and γ in shaping Ly α escape fraction. Fig. 29 illustrates these relationships through joint distributions of key physical properties. The $V_{\text{exp}} - f_{\text{esc, Ly}\alpha}^{\text{obs}}$ panel shows a clear trend: galaxies require sufficiently high outflow velocities (high α) to achieve large escape fractions, but even strong outflows can not guarantee Ly α escape if HI column densities (N_{HI}) or dust optical depths (τ_a) are too high. This explains why α primarily influences the bright end of the luminosity function. Only galaxies with both high SFRs (generating abundance Ly α photons) and powerful outflows (enabling their escape) dominate this regime. The $N_{\text{HI}} - f_{\text{esc, Ly}\alpha}^{\text{obs}}$ panel shows β 's broad impact. Higher β increases N_{HI} , enhancing resonance trapping and reducing escape across all luminosities. Low-mass galaxies with their higher M_{HI}/M_* ratios (Fig. 4), experience slightly stronger suppression. Meanwhile, γ 's dust attenuation scale ($\tau_a \propto Z_{\text{cold}} N_{\text{HI}}$) uniformly lowers $f_{\text{esc, Ly}\alpha}^{\text{obs}}$, blocking photons independent of galaxy luminosity. This results in a near parallel shift of the luminosity function.

Understanding these distinct parameter effects is crucial for our calibration process. The sensitivity of the bright-end slope of the luminosity function to α , combined with the broad suppression in normalization from β , and the overall normalization controlled by γ allows us to constrain each parameter independently. This multi-dimensional fitting approach ensures our model captures the complex physics governing Ly α escape while remaining constraint by observations. By isolating these effects (Figs. 28 and 29) our model captures the essential physics governing Ly α visibility while remaining empirically grounded.

D.2. Impact of free parameters on the angular correlation function

The angular correlation function, $w(\theta)$, encodes how LAEs cluster across different scales. This clustering is sensitive to the underlying halo occupation of LAEs, which in turn depends on the radiative transfer processes governed by our three free parameters α (outflow velocity scaling), β (neutral hydrogen column density scaling), and γ (dust attenuation scaling). To understand their individual effects, we systematically vary each parameter, while holding the others fixed at their best-fit values and analyze the resulting change in $w(\theta)$.

The expansion velocity of gas shells, scaled by α , determines how efficiently Ly α photons escape resonant scattering. Higher α

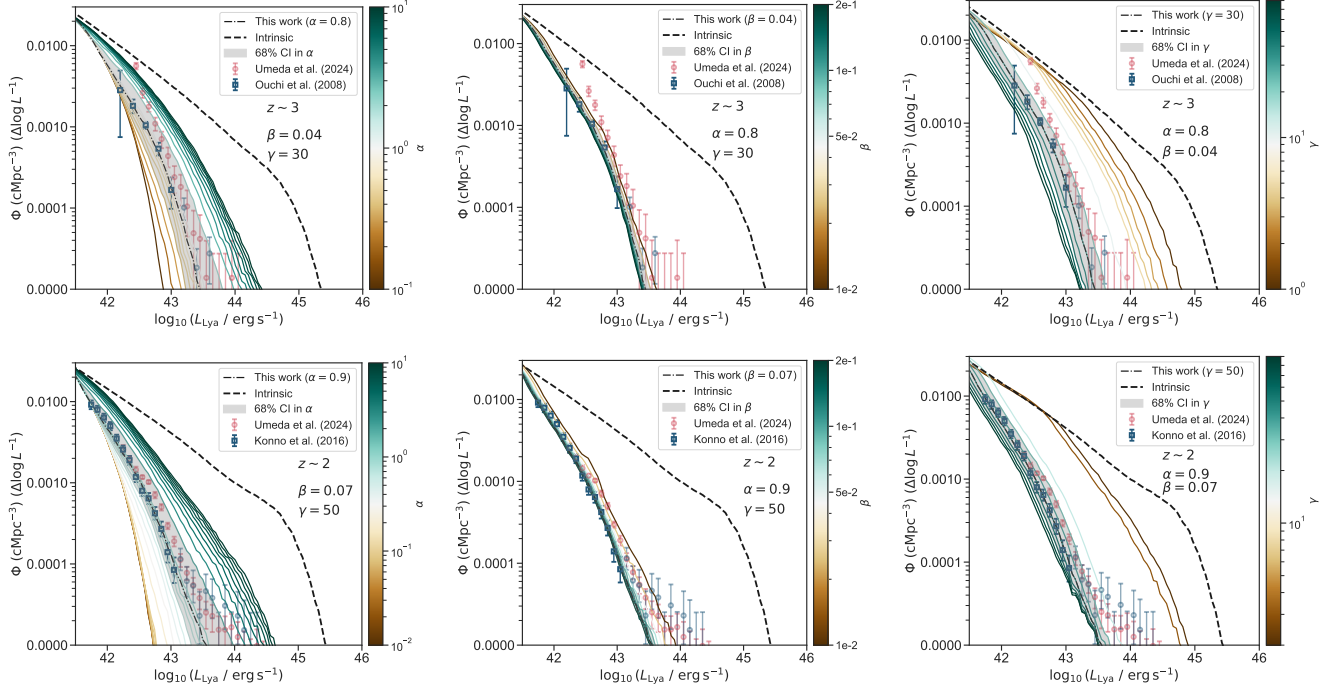


FIG. 28.— Sensitivity of the $\text{Ly}\alpha$ luminosity function to variations in the model parameters, α (outflow velocity scaling), β (HI column density scaling), and γ (dust attenuation scaling). Each column shows the effect of varying one parameter (with values indicated in the legend), while fixing the others to their best-fit values derived in Sec. 4.1. Upper panels show the impact of the free parameters on LF at $z \sim 3$, while lower panels present the impacts at $z \sim 2$. This analysis illustrates how increasing α primarily boosts the bright end as stronger outflows enhance $\text{Ly}\alpha$ escape in high-SFR galaxies, higher β uniformly suppresses $\text{Ly}\alpha$ escape across all luminosities and increasing γ causing a near parallel downward shift in normalization. Observational data from Konno et al. (2016) at $z \sim 2$ and Ouchi et al. (2008) at $z \sim 3$ are over-plotted, showing the consistency of the best-fit model with constraints across redshifts.

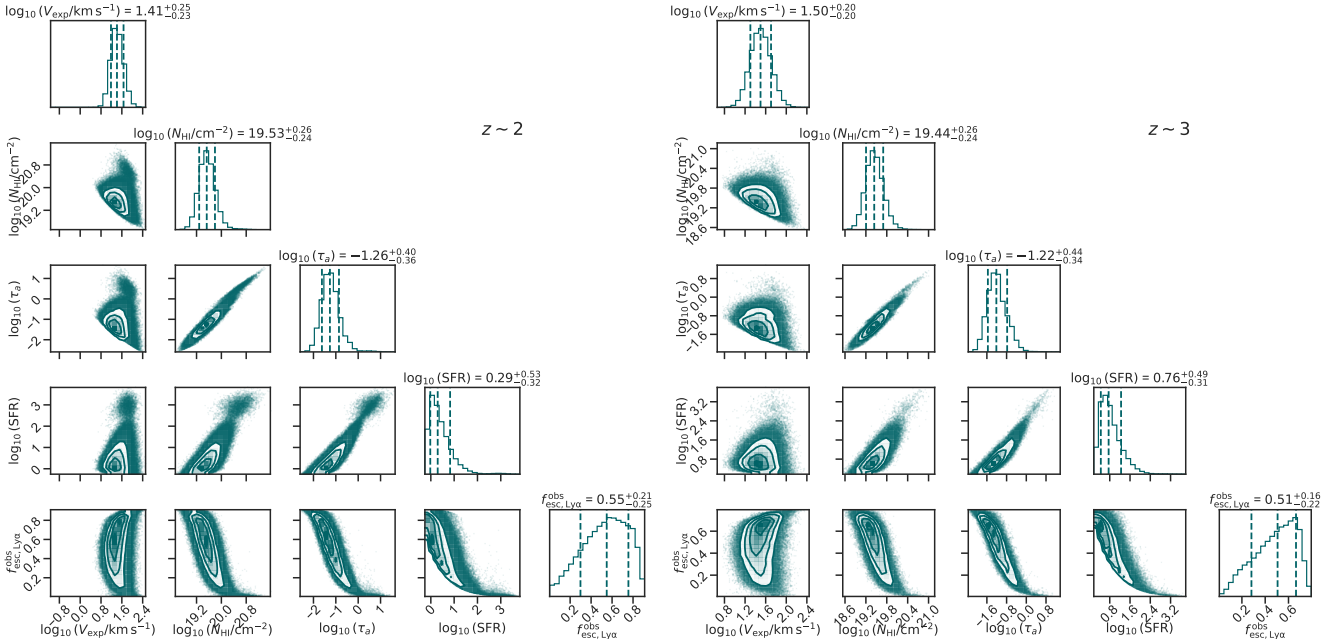


FIG. 29.— Corner plot showing the joint distribution and the correlation between key radiative transfer parameters at $z \sim 2$ (left) and $z \sim 3$ (right). Each 1D histogram along the diagonal shows the distribution for one parameter, expansion velocity, $\log_{10}(v_{\text{exp}}/\text{km s}^{-1})$, neutral hydrogen column density, $\log_{10}(N_{\text{HI}}/\text{cm}^{-2})$, dust absorption optical depth, $\log_{10}(\tau_a)$, star formation rate, $\log_{10}(\text{SFR})$ and the resulting observed $\text{Ly}\alpha$ escape fraction, $f_{\text{esc}, \text{Ly}\alpha}^{\text{obs}}$ with vertical dashed lines marking the median and 68% confidence intervals of the distribution. Off-diagonal panels show the joint distribution 2D credible regions at 68%, 95.4% and 99.7% levels illustrating the correlations between each pair of parameters.

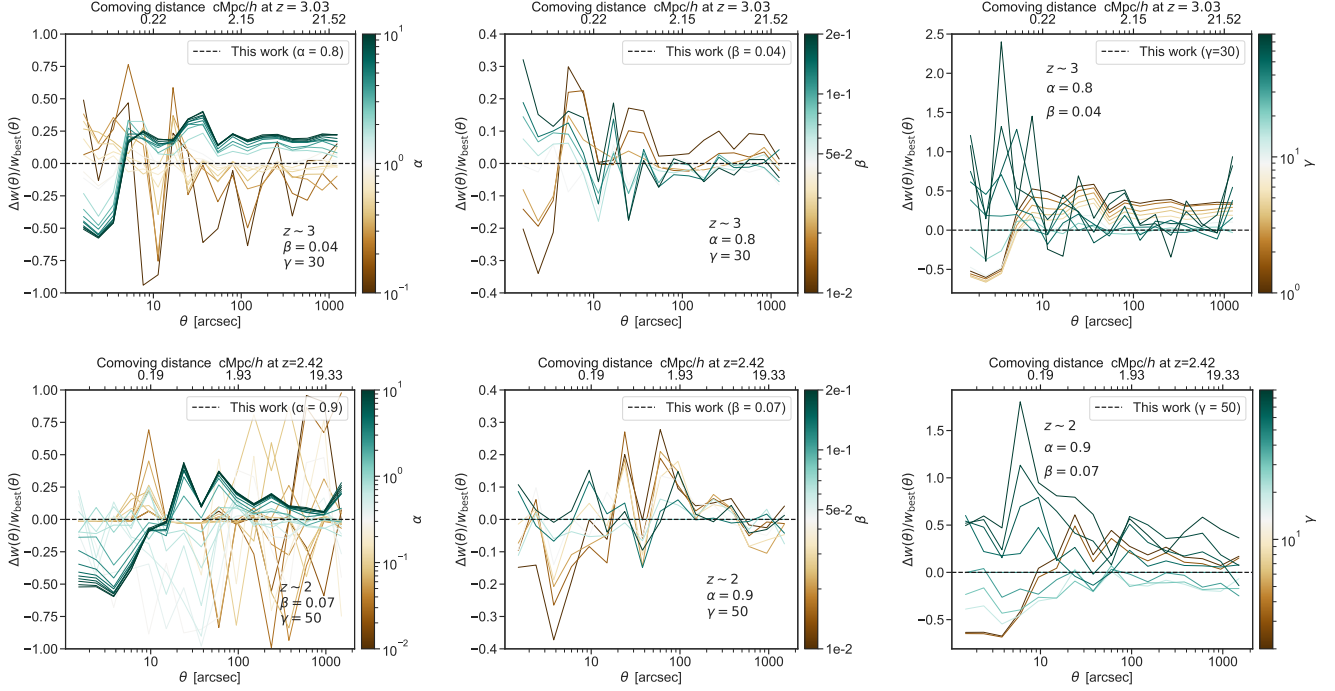


FIG. 30.— Scale dependent response of the LAE angular correlation function, $w(\theta)$, to variation in radiative transfer parameters. *Left:* Outflow velocity scaling, α , enhances large-scale clustering while slightly suppressing small scales. *Middle and right:* Both HI column density scaling, β and dust attenuation scaling γ , show overall similar trends: increasing small-scale clustering, while weakening large scale correlations.

values leads to stronger outflows which shift photons to the wings of the line profile, reducing interactions with neutral hydrogen. This enhances the detectability of central galaxies in massive halos, where star formation rates are high. As shown in Fig. 30 (left-most panels), increasing α produces two opposite trends. At large scales ($\theta \gtrsim 100''$), the clustering amplitude rises because more central galaxies in massive halos become detectable, amplifying the two-halo term. These systems are highly biased and dominate pair-counts at large separations. At small scales ($\theta \lesssim 10''$), the signal weakens slightly. While outflows aid escape, satellite galaxies, even with boosted $f_{\text{esc, Ly}\alpha}^{\text{obs}}$, often remain below the detection threshold due to their lower intrinsic luminosities. This reduces the contribution of satellite-satellite and central-satellite pairs to the 1-halo term, in other words, it reduces the satellite fraction. This contrast highlights a key feature of LAE clustering. Bright centrals drive the large-scale signal, while the faint satellite population shapes small-scale correlations.

The parameter β controls the neutral hydrogen column density, N_{HI} , which sets the optical depth for Ly α scattering. Higher β values increases N_{HI} , suppressing Ly α escape across all galaxies but with important scale-dependent effect on clustering. Fig. 30 (middle panels), illustrate this impact. At small scales ($\theta \lesssim 10''$), higher β removes LAEs from low-mass halos (where gas fractions are typically higher, see Fig. 4). The surviving population becomes dominated by satellites in massive halos, where deeper gravitational potential well maintain dense gas reservoirs. This boosts the 1-halo term, as these satellites cluster tightly around their centrals. Conversely, at large scales ($\theta \gtrsim 100''$), higher β reduces the overall LAE number density by suppressing escape in lower-mass centrals (which have higher gas fraction and lower intrinsic luminosities). This weakens the 2-halo term, as fewer biased central galaxies contribute to large-scale pair counts.

The dust optical depth scaling parameter γ (where $\tau_a \propto \gamma Z_{\text{cold}} N_{\text{HI}}$; Eq. 8), exhibits the same scale dependent trend as β . At small scales ($\theta \lesssim 10''$), higher γ strengthens clustering because dust preferentially extinguishes LAEs in low-mass halos (where galaxies have lower metallicities; Fig. 4, but insufficient SFR to compensate for increased attenuation). Meanwhile, satellites in massive systems survive due to deeper gravitational potentials that retain both high dust and abundant satellite populations. This creates a surviving sample dominated by clustered satellites, boosting the 1-halo term. Conversely, at large scales ($\theta \gtrsim 100''$), higher γ reduces clustering amplitude because the suppression of low-mass centrals (with high gas fraction but low luminosity) decreases the overall LAE number density. While the most massive centrals remain detectable, their scarcity weakens the 2-halo term, as fewer bias tracers contribute to large-scale pairs (see Fig. 30 right-most panels).

The scale-dependent signatures of α , β and γ in the angular correlation function show how different physical processes control LAE visibility across cosmic environments. While outflows (α) enhance central galaxy detection, both HI scattering (β) and dust attenuation (γ) exhibit similar trends (increasing small-scale clustering through satellite preservation in massive halos, while weakening large-scale correlations through number density suppression). Although our fiducial model (calibrated to White et al. (2024)) primarily constrain the 2-halo regime, lacking strong small-scale (1-halo term) constraints. However, our tests in this

appendix shows the following overall trend: increasing the Ly α escape fraction, whether via stronger outflows (higher α), reduced HI column density (lower β) or weaker dust (lower γ), systematically decreases the satellite fraction. This occurs because higher escape fractions preferentially increases the detectability of luminous central galaxies, while fainter satellites remain more likely to fall below the luminosity threshold. Our results shows the complex behavior between galaxy formation physics and observable LAE populations. It highlights how clustering measurements when combined with luminosity function, offer constraints on the gas and dust environments shaping Ly α emission across cosmic time.

REFERENCES

- Almada Monter, S., & Gronke, M. 2024, MNRAS, 534, L7, doi: [10.1093/mnras/1/slae074](#)
- Arribas, S., Colina, L., Bellocchi, E., Maiolino, R., & Villar-Martín, M. 2014, A&A, 568, A14, doi: [10.1051/0004-6361/201323324](#)
- Artale, M. C., Zehavi, I., Contreras, S., & Norberg, P. 2018, MNRAS, 480, 3978, doi: [10.1093/mnras/sty2110](#)
- Atek, H., Kunth, D., Hayes, M., Östlin, G., & Mas-Hesse, J. M. 2008, A&A, 488, 491, doi: [10.1051/0004-6361/200809527](#)
- Atek, H., Kunth, D., Schaerer, D., et al. 2014, A&A, 561, A89, doi: [10.1051/0004-6361/201321519](#)
- Aung, H., Nagai, D., Klypin, A., et al. 2023, MNRAS, 519, 1648, doi: [10.1093/mnras/stac3514](#)
- Baur, J., Palanque-Delabrouille, N., Yèche, C., et al. 2017, Journal of Cosmology and Astroparticle Physics, 2017, 013, doi: [10.1088/1475-7516/2017/12/013](#)
- Behrens, C., Byrohl, C., Saito, S., & Niemeyer, J. C. 2018, A&A, 614, A31, doi: [10.1051/0004-6361/201731783](#)
- Behroozi, P., Wechsler, R. H., Hearin, A. P., & Conroy, C. 2019, Monthly Notices of the Royal Astronomical Society, 488, 3143, doi: [10.1093/mnras/stz1182](#)
- Behroozi, P. S., Wechsler, R. H., & Wu, H.-Y. 2012a, The Astrophysical Journal, 762, 109, doi: [10.1088/0004-637X/762/2/109](#)
- Behroozi, P. S., Wechsler, R. H., Wu, H.-Y., et al. 2012b, The Astrophysical Journal, 763, 18, doi: [10.1088/0004-637X/763/1/18](#)
- Benitez, N., Dupke, R., Moles, M., et al. 2014, arXiv e-prints, arXiv:1403.5237, doi: [10.48550/arXiv.1403.5237](#)
- Besuner, R., Dey, A., Drlica-Wagner, A., et al. 2025, arXiv e-prints, arXiv:2503.07923, doi: [10.48550/arXiv.2503.07923](#)
- Bird, S., Peiris, H. V., Viel, M., & Verde, L. 2011, Monthly Notices of the Royal Astronomical Society, 413, 1717, doi: [10.1111/j.1365-2966.2011.18245.x](#)
- Bird, S., Vogelsberger, M., Haehnelt, M., et al. 2014, MNRAS, 445, 2313, doi: [10.1093/mnras/stu1923](#)
- Bird, S., Fernandez, M., Ho, M.-F., et al. 2023, J. Cosmology Astropart. Phys., 2023, 037, doi: [10.1088/1475-7516/2023/10/037](#)
- Blanc, G. A., Adams, J. J., Gebhardt, K., et al. 2011, ApJ, 736, 31, doi: [10.1088/0004-637X/736/1/31](#)
- Boggess, A., Carr, F. A., Evans, D. C., et al. 1978, Nature, 275, 372, doi: [10.1038/275372a0](#)
- Bouwens, R. J., Illingworth, G. D., Oesch, P. A., et al. 2014, ApJ, 793, 115, doi: [10.1088/0004-637X/793/2/115](#)
- Brown, T., Catinella, B., Cortese, L., et al. 2015, MNRAS, 452, 2479, doi: [10.1093/mnras/stv1311](#)
- Byrohl, C., & Gronke, M. 2020, A&A, 642, L16, doi: [10.1051/0004-6361/202038685](#)
- Byrohl, C., & Nelson, D. 2023, MNRAS, 523, 5248, doi: [10.1093/mnras/stad1779](#)
- Byrohl, C., & Nelson, D. 2025, THOR: a GPU-accelerated and MPI-parallel radiative transfer code. <https://arxiv.org/abs/2507.11603>
- Byrohl, C., Saito, S., & Behrens, C. 2019, MNRAS, 489, 3472, doi: [10.1093/mnras/stz2260](#)
- Calzetti, D., Armus, L., Bohlin, R. C., et al. 2000, The Astrophysical Journal, 533, 682, doi: [10.1086/308692](#)
- Caruana, J., Wisotzki, L., Herenz, E. C., et al. 2017, Monthly Notices of the Royal Astronomical Society, 473, 30, doi: [10.1093/mnras/stx2307](#)
- Catinella, B., Saintonge, A., Janowiecki, S., et al. 2018, Monthly Notices of the Royal Astronomical Society, 476, 875, doi: [10.1093/mnras/sty089](#)
- Chabrier, G. 2003, PASP, 115, 763, doi: [10.1086/376392](#)
- Chang, S.-J., & Gronke, M. 2024, MNRAS, 532, 3526, doi: [10.1093/mnras/stae1664](#)
- Chiang, C.-T., Wullstein, P., Jeong, D., et al. 2013, J. Cosmology Astropart. Phys., 2013, 030, doi: [10.1088/1475-7516/2013/12/030](#)
- Cowie, L. L., Barger, A. J., & Hu, E. M. 2011, ApJ, 738, 136, doi: [10.1088/0004-637X/738/2/136](#)
- Crain, R. A., Schaye, J., Bower, R. G., et al. 2015, Monthly Notices of the Royal Astronomical Society, 450, 1937, doi: [10.1093/mnras/stv725](#)
- Crain, R. A., Bahé, Y. M., Lagos, C. d. P., et al. 2017, MNRAS, 464, 4204, doi: [10.1093/mnras/stw2586](#)
- Croft, R. A. C., Miralda-Escudé, J., Zheng, Z., Blomqvist, M., & Pieri, M. 2018, MNRAS, 481, 1320, doi: [10.1093/mnras/sty2302](#)
- Davé, R., Crain, R. A., Stevens, A. R. H., et al. 2020, MNRAS, 497, 146, doi: [10.1093/mnras/staa1894](#)
- Davé, R., Anglés-Alcázar, D., Narayanan, D., et al. 2019, Monthly Notices of the Royal Astronomical Society, 486, 2827, doi: [10.1093/mnras/stz937](#)
- Dayal, P., & Ferrara, A. 2012, Monthly Notices of the Royal Astronomical Society, 421, 2568, doi: [10.1111/j.1365-2966.2012.20486.x](#)
- DESI Collaboration, Aghamousa, A., Aguilar, J., et al. 2016, arXiv e-prints, arXiv:1611.00036, doi: [10.48550/arXiv.1611.00036](#)
- Dijkstra, M. 2017, arXiv e-prints, arXiv:1704.03416, doi: [10.48550/arXiv.1704.03416](#)
- Dijkstra, M., Haiman, Z., & Spaans, M. 2006, The Astrophysical Journal, 649, 14, doi: [10.1086/506243](#)
- Dijkstra, M., Lidz, A., & Wyithe, J. S. B. 2007, Monthly Notices of the Royal Astronomical Society, 377, 1175
- Dijkstra, M., & Westra, E. 2010, MNRAS, 401, 2343, doi: [10.1111/j.1365-2966.2009.15859.x](#)
- du Mas des Bourboux, H., Rich, J., Font-Ribera, A., et al. 2020, ApJ, 901, 153, doi: [10.3847/1538-4357/abb085](#)
- Duval, F., Schaerer, D., Östlin, G., & Laursen, P. 2014, A&A, 562, A52, doi: [10.1051/0004-6361/201220455](#)
- Ebina, H., & White, M. 2024, J. Cosmology Astropart. Phys., 2024, 052, doi: [10.1088/1475-7516/2024/06/052](#)
- Erb, D. K., Steidel, C. C., Shapley, A. E., et al. 2006, The Astrophysical Journal, 646, 107, doi: [10.1086/504891](#)
- Erb, D. K., Steidel, C. C., Trainor, R. F., et al. 2014, The Astrophysical Journal, 795, 33, doi: [10.1088/0004-637X/795/1/33](#)
- Euclid Collaboration, Castander, F. J., Fosalba, P., et al. 2025, A&A, 697, A5, doi: [10.1051/0004-6361/202450853](#)
- Fang, J. J., Faber, S. M., Koo, D. C., et al. 2018, ApJ, 858, 100, doi: [10.3847/1538-4357/aabcb4](#)
- Faucher-Giguère, C.-A., Feldmann, R., Quataert, E., et al. 2016, MNRAS, 461, L32, doi: [10.1093/mnras/1/slw091](#)
- Faucher-Giguère, C.-A., Lidz, A., Hernquist, L., & Zaldarriaga, M. 2008, The Astrophysical Journal, 688, 85, doi: [10.1086/592289](#)
- Ferguson, H. C., Dickinson, M., Giavalisco, M., et al. 2004, ApJ, 600, L107, doi: [10.1086/378578](#)
- Finkelstein, K. D., Papovich, C., Finkelstein, S. L., et al. 2011a, ApJ, 742, 108, doi: [10.1088/0004-637X/742/2/108](#)
- Finkelstein, S. L., Hill, G. J., Gebhardt, K., et al. 2011b, ApJ, 729, 140, doi: [10.1088/0004-637X/729/2/140](#)
- Firestone, N. M., Gawiser, E., Ramakrishnan, V., et al. 2023, arXiv e-prints, arXiv:2312.16075, doi: [10.48550/arXiv.2312.16075](#)
- Firestone, N. M., Gawiser, E., Iyer, K. G., et al. 2025, arXiv e-prints, arXiv:2501.08568, doi: [10.48550/arXiv.2501.08568](#)
- Gao, L., & White, S. D. M. 2007, MNRAS, 377, L5, doi: [10.1111/j.1745-3933.2007.00292.x](#)
- Garel, T., Blaizot, J., Guiderdoni, B., et al. 2015, MNRAS, 450, 1279, doi: [10.1093/mnras/stv374](#)
- Garel, T., Blaizot, J., Rosdahl, J., et al. 2021, Monthly Notices of the Royal Astronomical Society, 504, 1902, doi: [10.1093/mnras/stab990](#)
- Gebhardt, K., Mentuch Cooper, E., Ciardullo, R., et al. 2021, ApJ, 923, 217, doi: [10.3847/1538-4357/ac2e03](#)
- Genel, S., Vogelsberger, M., Springel, V., et al. 2014, Monthly Notices of the Royal Astronomical Society, 445, 175, doi: [10.1093/mnras/stu1654](#)
- Granato, G. L., Lacey, C. G., Silva, L., et al. 2000, ApJ, 542, 710, doi: [10.1086/317032](#)
- Gronke, M. 2017, A&A, 608, A139, doi: [10.1051/0004-6361/201731791](#)
- Gronke, M., Bull, P., & Dijkstra, M. 2015, The Astrophysical Journal, 812, 123, doi: [10.1088/0004-637X/812/2/123](#)
- Gronke, M., & Dijkstra, M. 2014, Monthly Notices of the Royal Astronomical Society, 444, 1095, doi: [10.1093/mnras/stu1513](#)
- Gronke, M., & Dijkstra, M. 2016, ApJ, 826, 14, doi: [10.3847/0004-637X/826/1/14](#)
- Gronke, M., Dijkstra, M., McCourt, M., & Oh, S. P. 2017, A&A, 607, A71, doi: [10.1051/0004-6361/201731013](#)
- Gronke, M., Girichidis, P., Naab, T., & Walch, S. 2018, The Astrophysical Journal Letters, 862, L7, doi: [10.3847/2041-8213/aad286](#)
- Gronke, M., Ocvirk, P., Mason, C., et al. 2021, MNRAS, 508, 3697, doi: [10.1093/mnras/stab2762](#)
- Gronke, M., Ocvirk, P., Mason, C., et al. 2021, Monthly Notices of the Royal Astronomical Society, 508, 3697, doi: [10.1093/mnras/stab2762](#)
- Gurung-Lopez, S., Byrohl, C., Gronke, M., et al. 2025, arXiv e-prints, arXiv:2501.04077, doi: [10.48550/arXiv.2501.04077](#)
- Gurung-López, S., Byrohl, C., Gronke, M., et al. 2025, arXiv e-prints, arXiv:2503.03824, doi: [10.48550/arXiv.2503.03824](#)
- Gurung-López, S., Orsi, Á. A., & Bonoli, S. 2019, MNRAS, 490, 733, doi: [10.1093/mnras/stz2591](#)
- Gurung-López, S., Saito, S., Baugh, C. M., et al. 2021, MNRAS, 500, 603, doi: [10.1093/mnras/staa3269](#)

- Gurung-López, S., Gronke, M., Saito, S., Bonoli, S., & Orsi, A. A. 2021, *Monthly Notices of the Royal Astronomical Society*, 510, 4525, doi: [10.1093/mnras/stab3554](#)
- Gurung-López, S., Orsi, A. A., Bonoli, S., Baugh, C. M., & Lacey, C. G. 2019a, *Monthly Notices of the Royal Astronomical Society*, 486, 1882, doi: [10.1093/mnras/stz838](#)
- Gurung-López, S., Orsi, A. A., Bonoli, S., et al. 2019b, *Monthly Notices of the Royal Astronomical Society*, 491, 3266, doi: [10.1093/mnras/stz3204](#)
- Hadzhiyska, B., Font-Ribera, A., Cuceu, A., et al. 2023, *Monthly Notices of the Royal Astronomical Society*, 524, 1008, doi: [10.1093/mnras/stad1920](#)
- Hamana, T., Ouchi, M., Shimasaku, K., Kayo, I., & Suto, Y. 2004, *MNRAS*, 347, 813, doi: [10.1111/j.1365-2966.2004.07253.x](#)
- Hansen, M., & Oh, S. P. 2006, *MNRAS*, 367, 979, doi: [10.1111/j.1365-2966.2005.09870.x](#)
- Harrington, J. P. 1973, *Monthly Notices of the Royal Astronomical Society*, 162, 43, doi: [10.1093/mnras/162.1.43](#)
- Haskell, P., Das, S., Smith, D. J. B., et al. 2024, *MNRAS*, 530, L7, doi: [10.1093/mnras/ltae019](#)
- Hayes, M. J., Runnholm, A., Gronke, M., & Scarlata, C. 2021, *ApJ*, 908, 36, doi: [10.3847/1538-4357/abd246](#)
- Hearin, A., Behroozi, P., Kravtsov, A., & Moster, B. 2019, *Monthly Notices of the Royal Astronomical Society*, 489, 1805, doi: [10.1093/mnras/stz2251](#)
- Hearin, A. P., Zentner, A. R., van den Bosch, F. C., Campbell, D., & Tollerud, E. 2016, *Monthly Notices of the Royal Astronomical Society*, 460, 2552, doi: [10.1093/mnras/stw840](#)
- Hearin, A. P., Campbell, D., Tollerud, E., et al. 2017, *The Astrophysical Journal*, 154, 190, doi: [10.3847/1538-3881/aa859f](#)
- Herenz, E. C., Wisotzki, L., Saust, R., et al. 2019, *A&A*, 621, A107, doi: [10.1051/0004-6361/201834164](#)
- Herrera, D., Gawiser, E., Benda, B., et al. 2025, arXiv e-prints, arXiv:2503.17824, doi: [10.48550/arXiv.2503.17824](#)
- Herrero Alonso, Y., Krumpe, M., Wisotzki, L., et al. 2021, *A&A*, 653, A136, doi: [10.1051/0004-6361/202141226](#)
- Hill, G. J., Lee, H., MacQueen, P. J., et al. 2021, *AJ*, 162, 298, doi: [10.3847/1538-3881/ac2c02](#)
- Hong, S., Dey, A., Lee, K.-S., et al. 2019, *MNRAS*, 483, 3950, doi: [10.1093/mnras/sty3219](#)
- Hopkins, P. F., Quataert, E., & Murray, N. 2012, *MNRAS*, 421, 3522, doi: [10.1111/j.1365-2966.2012.20593.x](#)
- Huang, K.-H., Fall, S. M., Ferguson, H. C., et al. 2017, *ApJ*, 838, 6, doi: [10.3847/1538-4357/aa62a6](#)
- Huang, S., Haynes, M. P., Giovanelli, R., & Brinchmann, J. 2012, *The Astrophysical Journal*, 756, 113, doi: [10.1088/0004-637X/756/2/113](#)
- Hutter, A., Dayal, P., & Müller, V. 2015, *MNRAS*, 450, 4025, doi: [10.1093/mnras/stv929](#)
- Im, S. H., Hwang, H. S., Park, J., et al. 2024, *ApJ*, 972, 196, doi: [10.3847/1538-4357/ad67d2](#)
- Inoue, A. K., Shimizu, I., Iwata, I., & Tanaka, M. 2014, *MNRAS*, 442, 1805, doi: [10.1093/mnras/stu936](#)
- Inoue, A. K., Hasegawa, K., Ishiyama, T., et al. 2018, *PASJ*, 70, 55, doi: [10.1093/pasj/psy048](#)
- Iršič, V., Viel, M., Haehnelt, M. G., Bolton, J. S., & Becker, G. D. 2017, *Phys. Rev. Lett.*, 119, 031302, doi: [10.1103/PhysRevLett.119.031302](#)
- Iršič, V., Viel, M., Berg, T. A. M., et al. 2016, *Monthly Notices of the Royal Astronomical Society*, 466, 4332, doi: [10.1093/mnras/stw3372](#)
- Jensen, H., Hayes, M., Iliev, I. T., et al. 2014, *Monthly Notices of the Royal Astronomical Society*, 444, 2114, doi: [10.1093/mnras/stu1600](#)
- Jiang, F., & van den Bosch, F. C. 2016, *Monthly Notices of the Royal Astronomical Society*, 458, 2848, doi: [10.1093/mnras/stw439](#)
- Karmakar, T., Genel, S., & Somerville, R. S. 2023, *MNRAS*, 520, 1630, doi: [10.1093/mnras/stad178](#)
- Kashino, D., Silverman, J. D., Rodighiero, G., et al. 2013, *ApJ*, 777, L8, doi: [10.1088/2041-8205/777/1/L8](#)
- Kennicutt, Robert C., J. 1998, *ARA&A*, 36, 189, doi: [10.1146/annurev.astro.36.1.189](#)
- Khostovan, A. A., Sobral, D., Mobasher, B., et al. 2019, *Monthly Notices of the Royal Astronomical Society*, 489, 555, doi: [10.1093/mnras/stz2149](#)
- Kirkman, D., Tytler, D., Suzuki, N., et al. 2005, *Monthly Notices of the Royal Astronomical Society*, 360, 1373, doi: [10.1111/j.1365-2966.2005.09126.x](#)
- Kitaura, F.-S., Rodríguez-Torres, S., Chuang, C.-H., et al. 2016, *MNRAS*, 456, 4156, doi: [10.1093/mnras/stv2826](#)
- Klypin, A., Yepes, G., Gottlöber, S., Prada, F., & Heß, S. 2016, *Monthly Notices of the Royal Astronomical Society*, 457, 4340, doi: [10.1093/mnras/stw248](#)
- Kobayashi, M. A. R., & Totani, M., T. N. 2008, in *Astronomical Society of the Pacific Conference Series*, Vol. 399, *Panoramic Views of Galaxy Formation and Evolution*, ed. T. Kodama, T. Yamada, & K. Aoki, 32
- Konno, A., Ouchi, M., Nakajima, K., et al. 2016, *The Astrophysical Journal*, 823, 20, doi: [10.3847/0004-637X/823/1/20](#)
- Kravtsov, A. V. 2013, *The Astrophysical Journal Letters*, 764, L31, doi: [10.1088/2041-8205/764/2/L31](#)
- Kroupa, P. 2001, *MNRAS*, 322, 231, doi: [10.1046/j.1365-8711.2001.04022.x](#)
- Kusakabe, H., Shimasaku, K., Ouchi, M., et al. 2018, *Publications of the Astronomical Society of Japan*, 70, 4, doi: [10.1093/pasj/psx148](#)
- Kusakabe, H., Blaizot, J., Garel, T., et al. 2020, *A&A*, 638, A12, doi: [10.1051/0004-6361/201937340](#)
- Kwan, J., Sánchez, C., Clampitt, J., et al. 2017, *MNRAS*, 464, 4045, doi: [10.1093/mnras/stw2464](#)
- Landriau, M., Mentuch Cooper, E., Davis, D., et al. 2025, arXiv e-prints, arXiv:2503.02229, doi: [10.48550/arXiv.2503.02229](#)
- Landy, S. D., & Szalay, A. S. 1993, *ApJ*, 412, 64, doi: [10.1086/172900](#)
- Laursen, P., Duval, F., & Östlin, G. 2013, *ApJ*, 766, 124, doi: [10.1088/0004-637X/766/2/124](#)
- Laursen, P., Razoumov, A. O., & Sommer-Larsen, J. 2009, *The Astrophysical Journal*, 696, 853, doi: [10.1088/0004-637X/696/1/853](#)
- Laursen, P., Sommer-Larsen, J., & Razoumov, A. O. 2011, *ApJ*, 728, 52, doi: [10.1088/0004-637X/728/1/52](#)
- Le Delliou, M., Lacey, C. G., Baugh, C. M., & Morris, S. L. 2006, *MNRAS*, 365, 712, doi: [10.1111/j.1365-2966.2005.09797.x](#)
- Leclercq, F., Bacon, R., Wisotzki, L., et al. 2017, *A&A*, 608, A8, doi: [10.1051/0004-6361/201731480](#)
- Lee, K.-S., Gawiser, E., Park, C., et al. 2024, *ApJ*, 962, 36, doi: [10.3847/1538-4357/ad165e](#)
- Levi, M., Bebek, C., Beers, T., et al. 2013, arXiv e-prints, arXiv:1308.0847, doi: [10.48550/arXiv.1308.0847](#)
- Li, Z., & Gronke, M. 2022, *MNRAS*, 513, 5034, doi: [10.1093/mnras/stac1207](#)
- Lin, X., Zheng, Z., & Cai, Z. 2022, *ApJS*, 262, 38, doi: [10.3847/1538-4365/ac82e8](#)
- Liu, C., Gebhardt, K., Cooper, E. M., et al. 2022a, *ApJS*, 261, 24, doi: [10.3847/1538-4365/ac6ba6](#)
- , 2022b, *ApJ*, 935, 132, doi: [10.3847/1538-4357/ac8054](#)
- Lujan Niemeyer, M. 2025, *ApJ*, 980, 250, doi: [10.3847/1538-4357/ada8a3](#)
- Lujan Niemeyer, M., Bernal, J. L., & Komatsu, E. 2023, *ApJ*, 958, 4, doi: [10.3847/1538-4357/acfe4](#)
- Lujan Niemeyer, M., Bowman, W. P., Ciardullo, R., et al. 2022, *ApJ*, 934, L26, doi: [10.3847/2041-8213/ac82e5](#)
- Ma, X., Hopkins, P. F., Faucher-Giguère, C.-A., et al. 2016, *MNRAS*, 456, 2140, doi: [10.1093/mnras/stv2659](#)
- Madau, P. 1995, *ApJ*, 441, 18, doi: [10.1086/175332](#)
- Mainieri, V., Anderson, R. I., Brinchmann, J., et al. 2024, arXiv e-prints, arXiv:2403.05398, doi: [10.48550/arXiv.2403.05398](#)
- Mannucci, F., Cresci, G., Maiolino, R., et al. 2009, *Monthly Notices of the Royal Astronomical Society*, 398, 1915
- Marinacci, F., Vogelsberger, M., Pakmor, R., et al. 2018, *Monthly Notices of the Royal Astronomical Society*, 480, 5113, doi: [10.1093/mnras/sty2206](#)
- Martin, D. C., Fanson, J., Schiminovich, D., et al. 2005, *ApJ*, 619, L1, doi: [10.1086/426387](#)
- Mason, C. A., Trenti, M., & Treu, T. 2015, *The Astrophysical Journal*, 813, 21, doi: [10.1088/0004-637X/813/1/21](#)
- Mason, C. A., Treu, T., Dijkstra, M., et al. 2018, *ApJ*, 856, 2, doi: [10.3847/1538-4357/aab0a7](#)
- McCarron, A. P., Finkelstein, S. L., Chavez Ortiz, O. A., et al. 2022, *ApJ*, 936, 131, doi: [10.3847/1538-4357/ac8546](#)
- McDonald, P., Miralda-Escudé, J., Rauch, M., et al. 2000, *ApJ*, 543, 1, doi: [10.1086/317079](#)
- McDonald, P., Seljak, U., Cen, R., et al. 2005, *ApJ*, 635, 761, doi: [10.1086/497563](#)
- McDonald, P., Seljak, U., Burles, S., et al. 2006, *ApJS*, 163, 80, doi: [10.1086/444361](#)
- Meurer, G. R., Heckman, T. M., & Calzetti, D. 1999, *ApJ*, 521, 64, doi: [10.1086/307523](#)
- Miralda-Escudé, J., & Rees, M. J. 1994, *MNRAS*, 266, 343, doi: [10.1093/mnras/266.2.343](#)
- Momose, R., Ouchi, M., Nakajima, K., et al. 2014, *MNRAS*, 442, 110, doi: [10.1093/mnras/stu825](#)
- , 2016, *MNRAS*, 457, 2318, doi: [10.1093/mnras/stw021](#)
- Murgia, R., Iršič, V., & Viel, M. 2018, *Phys. Rev. D*, 98, 083540, doi: [10.1103/PhysRevD.98.083540](#)
- Murgia, R., Scelfo, G., Viel, M., & Raccanelli, A. 2019, *Phys. Rev. Lett.*, 123, 071102, doi: [10.1103/PhysRevLett.123.071102](#)
- Nagamine, K., Ouchi, M., Springel, V., & Hernquist, L. 2010, *PASJ*, 62, 1455, doi: [10.1093/pasj/62.6.1455](#)
- Naiman, J. P., Pillepich, A., Springel, V., et al. 2018, *Monthly Notices of the Royal Astronomical Society*, 477, 1206, doi: [10.1093/mnras/sty618](#)
- Nebrin, O., Smith, A., Lorinc, K., et al. 2025, *MNRAS*, 537, 1646, doi: [10.1093/mnras/staf038](#)
- Nelson, D., Pillepich, A., Springel, V., et al. 2017, *Monthly Notices of the Royal Astronomical Society*, 475, 624, doi: [10.1093/mnras/stx3040](#)
- Neufeld, D. A. 1990, *ApJ*, 350, 216, doi: [10.1086/168375](#)
- Nianias, J., Lim, J., Wong, Y. L., & Wong, G. 2025, arXiv e-prints, arXiv:2506.20422, doi: [10.48550/arXiv.2506.20422](#)
- Norberg, P., Baugh, C. M., Gaztañaga, E., & Croton, D. J. 2009, *MNRAS*, 396, 19, doi: [10.1111/j.1365-2966.2009.14389.x](#)

- Ouchi, M., Ono, Y., & Shibuya, T. 2020, *ARA&A*, 58, 617, doi: [10.1146/annurev-astro-032620-021859](#)
- Ouchi, M., Shimasaku, K., Akiyama, M., et al. 2008, *The Astrophysical Journal Supplement Series*, 176, 301, doi: [10.1086/527673](#)
- Ouchi, M., Harikane, Y., Shibuya, T., et al. 2018, *PASJ*, 70, S13, doi: [10.1093/pasj/psx074](#)
- Oyarzún, G. A., Blanc, G. A., González, V., Mateo, M., & Bailey, J. I. 2017, *The Astrophysical Journal*, 843, 133, doi: [10.3847/1538-4357/aa7552](#)
- Park, H., Jung, I., Song, H., et al. 2021, *The Astrophysical Journal*, 922, 263, doi: [10.3847/1538-4357/ac2f4b](#)
- Parsa, S., Dunlop, J. S., McLure, R. J., & Mortlock, A. 2016, *Monthly Notices of the Royal Astronomical Society*, 456, 3194, doi: [10.1093/mnras/stv2857](#)
- Partridge, R. B., & Peebles, P. J. E. 1967, *ApJ*, 147, 868, doi: [10.1086/149079](#)
- Pedregosa, F., Varoquaux, G., Gramfort, A., et al. 2011, *Journal of Machine Learning Research*, 12, 2825
- Peebles, P. J. E. 1980, *The large-scale structure of the universe*
- Pillepich, A., Nelson, D., Hernquist, L., et al. 2017, *Monthly Notices of the Royal Astronomical Society*, 475, 648, doi: [10.1093/mnras/stx3112](#)
- Pillepich, A., Springel, V., Nelson, D., et al. 2018, *MNRAS*, 473, 4077, doi: [10.1093/mnras/stx2656](#)
- Planck Collaboration, Ade, P. A. R., Aghanim, N., et al. 2014, *A&A*, 571, A16, doi: [10.1051/0004-6361/201321591](#)
- Prada, F., Ezeiza, J., Smith, A., et al. 2023, *arXiv e-prints*, arXiv:2306.06315, doi: [10.48550/arXiv.2306.06315](#)
- Qezlou, M., Newman, A. B., Rudie, G. C., & Bird, S. 2022, *The Astrophysical Journal*, 930, 109, doi: [10.3847/1538-4357/ac6259](#)
- Ramakrishnan, V., Moon, B., Im, S. H., et al. 2023, *ApJ*, 951, 119, doi: [10.3847/1538-4357/acd341](#)
- Ravi, J., Hadzhiyska, B., White, M. J., Hernquist, L., & Bose, S. 2024, *Phys. Rev. D*, 110, 103509, doi: [10.1103/PhysRevD.110.103509](#)
- Ravindranath, S., Ferguson, H. C., Conselice, C., et al. 2004, *ApJ*, 604, L9, doi: [10.1086/382952](#)
- Reddy, N. A., & Steidel, C. C. 2009, *The Astrophysical Journal*, 692, 778, doi: [10.1088/0004-637X/692/1/778](#)
- Reddy, N. A., Steidel, C. C., Pettini, M., et al. 2008, *The Astrophysical Journal Supplement Series*, 175, 48, doi: [10.1086/521105](#)
- Rohr, E., Feldmann, R., Bullock, J. S., et al. 2022, *MNRAS*, 510, 3967, doi: [10.1093/mnras/stab3625](#)
- Rossi, G., Choi, P. D., Moon, J., et al. 2021, *MNRAS*, 505, 377, doi: [10.1093/mnras/staa3955](#)
- Runnholm, A., Gronke, M., & Hayes, M. 2021, *PASP*, 133, 034507, doi: [10.1088/1538-3873/abe3ca](#)
- Runnholm, A., Hayes, M., Melinder, J., et al. 2020, *The Astrophysical Journal*, 892, 48, doi: [10.3847/1538-4357/ab7a91](#)
- Saintonge, A., Catinella, B., Tacconi, L. J., et al. 2017, *ApJS*, 233, 22, doi: [10.3847/1538-4365/aa97e0](#)
- Saito, S., de la Torre, S., Ilbert, O., et al. 2020, *MNRAS*, 494, 199, doi: [10.1093/mnras/staa727](#)
- Saito, S., Leauthaud, A., Hearin, A. P., et al. 2016, *MNRAS*, 460, 1457, doi: [10.1093/mnras/stw1080](#)
- Sanders, R. L., Shapley, A. E., Kriek, M., et al. 2015, *The Astrophysical Journal*, 799, 138
- Scarlata, C., Colbert, J., Teplitz, H. I., et al. 2009, *ApJ*, 704, L98, doi: [10.1088/0004-637X/704/2/L98](#)
- Schaan, E., & White, M. 2021, *J. Cosmology Astropart. Phys.*, 2021, 068, doi: [10.1088/1475-7516/2021/05/068](#)
- Schaefer, D. 2003, *A&A*, 397, 527, doi: [10.1051/0004-6361:20021525](#)
- Schaye, J., Aguirre, A., Kim, T.-S., et al. 2003, *ApJ*, 596, 768, doi: [10.1086/378044](#)
- Schaye, J., Crain, R. A., Bower, R. G., et al. 2014, *Monthly Notices of the Royal Astronomical Society*, 446, 521, doi: [10.1093/mnras/stu2058](#)
- Schlegel, D. J., Ferraro, S., Aldering, G., et al. 2022, *arXiv e-prints*, arXiv:2209.03585, doi: [10.48550/arXiv.2209.03585](#)
- Schmidt, M. 1968, *ApJ*, 151, 393, doi: [10.1086/149446](#)
- Seaton, M. J. 1979, *MNRAS*, 187, 73, doi: [10.1093/mnras/187.1.73P](#)
- Semelin, B., Combes, F., & Baek, S. 2007, *A&A*, 474, 365, doi: [10.1051/0004-6361:20077965](#)
- Sheth, R. K., & Tormen, G. 1999, *MNRAS*, 308, 119, doi: [10.1046/j.1365-8711.1999.02692.x](#)
- Shibuya, T., Ouchi, M., & Harikane, Y. 2015, *ApJS*, 219, 15, doi: [10.1088/0067-0049/219/2/15](#)
- Shibuya, T., Ouchi, M., Harikane, Y., & Nakajima, K. 2019, *The Astrophysical Journal*, 871, 164, doi: [10.3847/1538-4357/aaf64b](#)
- Shimizu, I., & Umemura, M. 2010, *MNRAS*, 406, 913, doi: [10.1111/j.1365-2966.2010.16758.x](#)
- Shimizu, I., Yoshida, N., & Okamoto, T. 2011, *MNRAS*, 418, 2273, doi: [10.1111/j.1365-2966.2011.19549.x](#)
- Smith, A., Kannan, R., Garaldi, E., et al. 2022, *MNRAS*, 512, 3243, doi: [10.1093/mnras/stac713](#)
- Smith, A., Lorinc, K., Nebrin, O., & Lao, B.-X. 2025, *MNRAS*, doi: [10.1093/mnras/staf961](#)
- Smith, A., Ma, X., Bromm, V., et al. 2019, *MNRAS*, 484, 39, doi: [10.1093/mnras/sty3483](#)
- Smith, A., Safranek-Shrader, C., Bromm, V., & Milosavljević, M. 2015, *Monthly Notices of the Royal Astronomical Society*, 449, 4336, doi: [10.1093/mnras/stv565](#)
- Sobral, D., & Matthee, J. 2019, *A&A*, 623, A157, doi: [10.1051/0004-6361/201833075](#)
- Somerville, R. S., Gabrielpillai, A., Hadzhiyska, B., & Genel, S. 2025, *arXiv e-prints*, arXiv:2502.03679, doi: [10.48550/arXiv.2502.03679](#)
- Somerville, R. S., Behroozi, P., Pandya, V., et al. 2018, *MNRAS*, 473, 2714, doi: [10.1093/mnras/stx2040](#)
- Song, H., Seon, K.-I., & Hwang, H. S. 2020, *ApJ*, 901, 41, doi: [10.3847/1538-4357/abac02](#)
- Spinoso, D., Orsi, A., López-Sanjuan, C., et al. 2020, *A&A*, 643, A149, doi: [10.1051/0004-6361/202038756](#)
- Springel, V. 2005, *Monthly Notices of the Royal Astronomical Society*, 364, 1105, doi: [10.1111/j.1365-2966.2005.09655.x](#)
- Springel, V., Pakmor, R., Pillepich, A., et al. 2017, *Monthly Notices of the Royal Astronomical Society*, 475, 676, doi: [10.1093/mnras/stx3304](#)
- Stark, D. P., Ellis, R. S., & Ouchi, M. 2011, *The Astrophysical Journal Letters*, 728, L2, doi: [10.1088/2041-8205/728/1/L2](#)
- Steidel, C. C., Bogosavljević, M., Shapley, A. E., et al. 2011, *ApJ*, 736, 160, doi: [10.1088/0004-637X/736/2/160](#)
- Steidel, C. C., Erb, D. K., Shapley, A. E., et al. 2010, *ApJ*, 717, 289, doi: [10.1088/0004-637X/717/1/289](#)
- Steidel, C. C., Rudie, G. C., Strom, A. L., et al. 2014, *ApJ*, 795, 165, doi: [10.1088/0004-637X/795/2/165](#)
- Sullivan, J. M., Cuesta-Lazaro, C., Ivanov, M. M., et al. 2025, *arXiv e-prints*, arXiv:2505.03626, doi: [10.48550/arXiv.2505.03626](#)
- Sun, G., Faucher-Giguère, C.-A., Hayward, C. C., et al. 2023, *ApJ*, 955, L35, doi: [10.3847/2041-8213/acf85a](#)
- Sun, G., Muñoz, J. B., Mirocha, J., & Faucher-Giguère, C.-A. 2024, *arXiv e-prints*, arXiv:2410.21409, doi: [10.48550/arXiv.2410.21409](#)
- Tasitsiomi, A. 2006, *The Astrophysical Journal*, 645, 792, doi: [10.1086/504460](#)
- Tilvi, V., Malhotra, S., Rhoads, J. E., et al. 2009, *ApJ*, 704, 724, doi: [10.1088/0004-637X/704/1/724](#)
- Torralba-Torregrosa, A., Gurung-López, S., Arnalte-Mur, P., et al. 2023a, *A&A*, 680, A14, doi: [10.1051/0004-6361/202347463](#)
- . 2023b, *A&A*, 680, A14, doi: [10.1051/0004-6361/202347463](#)
- Tremonti, C. A., Heckman, T. M., Kauffmann, G., et al. 2004, *ApJ*, 613, 898, doi: [10.1086/423264](#)
- Umeda, H., Ouchi, M., Kikuta, S., et al. 2025, *ApJS*, 277, 37, doi: [10.3847/1538-4365/adb1c0](#)
- van de Voort, F., Springel, V., Mandelker, N., van den Bosch, F. C., & Pakmor, R. 2019, *MNRAS*, 482, L85, doi: [10.1093/mnras/1/sly190](#)
- van der Wel, A., Franx, M., van Dokkum, P. G., et al. 2014, *ApJ*, 788, 28, doi: [10.1088/0004-637X/788/1/28](#)
- Verhamme, A., Schaefer, D., & Maselli, A. 2006, *A&A*, 460, 397, doi: [10.1051/0004-6361:20065554](#)
- Viel, M., & Haehnelt, M. G. 2006, *MNRAS*, 365, 231, doi: [10.1111/j.1365-2966.2005.09703.x](#)
- Viel, M., Haehnelt, M. G., & Springel, V. 2004, *Monthly Notices of the Royal Astronomical Society*, 354, 684, doi: [10.1111/j.1365-2966.2004.08224.x](#)
- Villaescusa-Navarro, F., Anglés-Alcázar, D., Genel, S., et al. 2021, *ApJ*, 915, 71, doi: [10.3847/1538-4357/abf7ba](#)
- Vogelsberger, M., Genel, S., Springel, V., et al. 2014a, *Monthly Notices of the Royal Astronomical Society*, 444, 1518, doi: [10.1093/mnras/stu1536](#)
- . 2014b, *Nature*, 509, 177
- Vogelsberger, M., Nelson, D., Pillepich, A., et al. 2020, *MNRAS*, 492, 5167, doi: [10.1093/mnras/staa137](#)
- Wechsler, R. H., & Tinker, J. L. 2018, *ARA&A*, 56, 435, doi: [10.1146/annurev-astro-081817-051756](#)
- Wechsler, R. H., Zentner, A. R., Bullock, J. S., Kravtsov, A. V., & Allgood, B. 2006, *The Astrophysical Journal*, 652, 71, doi: [10.1086/507120](#)
- Weiss, L. H., Bowman, W. P., Ciardullo, R., et al. 2021, *The Astrophysical Journal*, 912, 100, doi: [10.3847/1538-4357/abedb9](#)
- White, M., Raichoor, A., Dey, A., et al. 2024, *J. Cosmology Astropart. Phys.*, 2024, 020, doi: [10.1088/1475-7516/2024/08/020](#)
- Xu, C., Smith, A., Borrow, J., et al. 2023, *MNRAS*, 521, 4356, doi: [10.1093/mnras/stad789](#)
- Yajima, H., Li, Y., Zhu, Q., & Abel, T. 2012, *Monthly Notices of the Royal Astronomical Society*, 424, 884, doi: [10.1111/j.1365-2966.2012.21228.x](#)
- Yang, H., Malhotra, S., Gronke, M., et al. 2016, *The Astrophysical Journal*, 820, 130, doi: [10.3847/0004-637X/820/2/130](#)
- Zaldarriaga, M., Hui, L., & Tegmark, M. 2001, *The Astrophysical Journal*, 557, 519, doi: [10.1086/321652](#)
- Zanisi, L., Shankar, F., Lapi, A., et al. 2020, *MNRAS*, 492, 1671, doi: [10.1093/mnras/stz3516](#)
- Zehavi, I., Contreras, S., Padilla, N., et al. 2018, *ApJ*, 853, 84, doi: [10.3847/1538-4357/aaa54a](#)
- Zhang, Y., Ouchi, M., Gebhardt, K., et al. 2021, *ApJ*, 922, 167, doi: [10.3847/1538-4357/ac1e97](#)
- Zhao, C., Huang, S., He, M., et al. 2024, *arXiv e-prints*, arXiv:2411.07970, doi: [10.48550/arXiv.2411.07970](#)

Zheng, Z., Cen, R., Trac, H., & Miralda-Escudé, J. 2010, ApJ, 716, 574,
doi: [10.1088/0004-637X/716/1/574](https://doi.org/10.1088/0004-637X/716/1/574)
—, 2011, ApJ, 726, 38, doi: [10.1088/0004-637X/726/1/38](https://doi.org/10.1088/0004-637X/726/1/38)

Zheng, Z., & Miralda-Escudé, J. 2002, The Astrophysical Journal, 578, 33,
doi: [10.1086/342400](https://doi.org/10.1086/342400)
Zheng, Z.-Y., Malhotra, S., Rhoads, J. E., et al. 2016, ApJS, 226, 23,
doi: [10.3847/0067-0049/226/2/23](https://doi.org/10.3847/0067-0049/226/2/23)